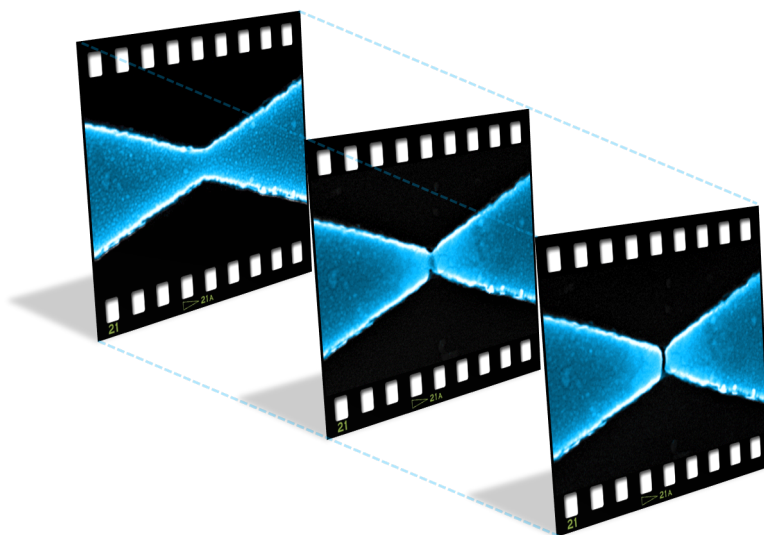




FACULTY OF SCIENCES
CESAM RESEARCH UNIT, Q-MAT CENTER
EXPERIMENTAL PHYSICS OF NANOSTRUCTURED MATERIALS



Nano-engineering superconducting junctions by atomic migration

Xavier Baumans

Dissertation presented in partial fulfilment of
the requirements for the degree of Doctor of
Science

Academic year 2018-2019



FACULTY OF SCIENCES
CESAM RESEARCH UNIT, Q-MAT CENTER
EXPERIMENTAL PHYSICS OF NANOSTRUCTURED MATERIALS

Nano-engineering superconducting junctions by atomic migration

Jury:

Prof. Dr. Philippe Ghosez (Chairman)

Dr. Stéphane Dorbolo (Secretary)

Prof. Dr. François Peeters (UAntwerp, Belgium)

Prof. Dr. Francesco Tafuri (Università degli
Studi di Napoli, Italy)

Prof. Dr. Joris Van de Vondel (KULeuven, Belgium)

Prof. Dr. A. V. Silhanek (Advisor)

October 2018

Dissertation presented in partial fulfilment of the requirements for the degree of Doctor of Science

by

Xavier Baumans

Academic year 2018-2019

© Copyright by Université de Liège - Faculté des Sciences, Place du 20 août, 7, B-4000 Liège, Belgium

Tous droits réservés. Aucune partie de ce document ne peut être reproduite sous forme d'imprimé, photocopie ou par n'importe quel autre moyen, sans l'autorisation écrite de l'auteur ou du promoteur.

All Rights Reserved. No part of this publication may be reproduced in any form by print, photo print or any other means without permission in writing from the author or the supervisor.

In memory of my godfather, André Habay. I wish you could be there, grandpa.

Abstract

Superconductivity is a fascinating quantum phenomenon able to manifest itself at truly macroscopic scale. From magnetic levitation to lossless power cables, from magnetic resonance imaging to plasma confinement for nuclear fusion, it has a bright future ahead, particularly in the field of quantum information. However, the dissipationless state, the hallmark of superconductivity, may be threatened or plainly disappear at low dimensions, as for instance in superconducting nanocircuits, mainly due to fluctuations. The dominant fluctuations are those concerning a simultaneous depletion of the order parameter and a slippage of the superconducting phase, known as phase slips, and can occur via thermal or athermal (i.e. quantum) excitations. Although extensively investigated during the last decades, a full understanding of phase slips, and especially quantum driven fluctuations, is still lacking.

This thesis is devoted to the development and experimental investigation of nano-engineered superconducting junctions. Since the advent of nanotechnologies, nanoscale has been reached with relative accuracy by several fabrication methods. Nanowires, including some made of superconducting materials, have been produced and the current limit is situated around few nanometers of lateral dimension, which is not far from where the transition from thermal to quantum fluctuations of the superconducting phase is expected. We thus propose to bypass this limitation by taking advantage of the possibility to induce atomic migration under an electron wind to carve superconducting junctions well below ten nanometers, and even reach single atom scales.

The first task in this work consists in mastering the process of electromigration before applying it to superconducting constricted junctions of multiple kinds. It is observed that electromigration can locally alter material properties and be fully reversed in Al, partially in $\text{La}_{2-x}\text{Ce}_x\text{CuO}_4$ whereas it becomes rather irreversible in Nb. While electromigration induces clear structural changes in Al, more complex mechanisms are at work in Nb and $\text{La}_{2-x}\text{Ce}_x\text{CuO}_4$, which are probably the reason for incomplete reversibility. In addition to the ability of going beyond sizes achieved by standard lithography techniques, the reversibility of the process can act as a powerful complementary tool to fine-tune the properties of a given junction. An easy-to-implement

method of current pulses is also presented, allowing to achieve faster but yet very efficient electromigration.

Following this approach, controlled electromigration is used to narrow down Al nanoconstrictions. We demonstrate that a transition from thermally assisted phase slips to quantum phase slips takes place when the cross section becomes smaller than $\sim 150 \text{ nm}^2$. In the regime dominated by quantum phase slips the nanowire loses its capacity to carry current without dissipation, even at the lowest possible temperature. We also show that electromigrated superconducting constrictions exhibit a negative magnetoresistance at low-magnetic fields, which can be attributed to the suppression of superconductivity in the contact leads.

At the moment this thesis work started, most of the reported studies had focused on long nanowires where coexisting phase slip events appear randomly along the nanowire. In the present work, we investigate highly confined phase slips at the contact point of two superconducting leads. The electromigration procedure allows us to shrink in situ the nanoconstriction and thus to investigate, in the very same sample, thermally activated phase slips and the probability density function of the switching current needed to trigger an avalanche of events. Furthermore, for an applied current larger than the switching current, the existence of two distinct thermal regimes is unveiled. One corresponding to efficient heat removal where the constriction and bath temperatures remain close to each other, and another one in which the constriction temperature can be substantially larger than the bath temperature leading to the formation of a steady normal region known as hot spot.

In the last experimental chapter of this thesis, we report on preliminary results concerning the temperature dependence of the current density $J_{EM}(T)$, above which atom migration takes place, for several superconducting materials. For high critical current density $J_c(T)$ superconductors, such as $\text{YBa}_2\text{Cu}_3\text{O}_{7-\delta}$, $J_{EM}(T)$ intersects $J_c(T)$ at certain temperature T^* . Therefore, for $T < T^*$ the superconducting dissipative state cannot be accessed without leading to irreversible modifications of the material properties. This phenomenon may also become an important mechanism of local sample deterioration in high critical temperature superconducting films abruptly penetrated by thermomagnetic instabilities.

Résumé

La supraconductivité est un phénomène quantique fascinant capable de se manifester à une échelle réellement macroscopique. De la lévitation magnétique aux câbles électriques sans pertes, en passant par l'imagerie par résonance magnétique ou le confinement du plasma dans les réacteurs à fusion, elle a un brillant avenir devant elle, en particulier dans le domaine de l'information quantique. Cependant, l'absence de dissipation, la marque de fabrique de l'état supraconducteur, pourrait être menacée ou même disparaître à petite échelle, comme par exemple dans les nanocircuits supraconducteurs, principalement à cause des fluctuations. Celles qui dominent sont liées à une réduction du paramètre d'ordre simultanée à un glissement de la phase supraconductrice. Ces fluctuations, connues sous le nom de glissements de phase, peuvent être déclenchées thermiquement ou non (i.e. quantiquement). Bien que largement étudiés au cours des dernières décennies, une compréhension complète de ces phénomènes, spécialement de ceux d'origine quantique, nous fait toujours défaut.

Cette thèse est dédiée au développement et à l'étude expérimentale de jonctions supraconductrices mises au point à l'échelle nanométrique. Depuis l'avènement des nanotechnologies, l'échelle nanométrique a été atteinte par différentes méthodes avec une précision relative. Des nanofils, dont certains faits de matériaux supraconducteurs, ont été produits et la frontière actuelle se situe aux alentours de quelques nanomètres de dimension latérale, non loin de là où l'on s'attend à observer la transition entre fluctuations thermiques et quantiques. Nous proposons de contourner cette limitation, en tirant parti d'une migration atomique induite par vent d'électrons pour tailler des jonctions supraconductrices bien en deçà de dix nanomètres, et même atteindre l'échelle monoatomique.

La première étape de ce travail consiste à maîtriser le procédé d'électromigration avant de l'appliquer à des constriction supraconductrices de différents types. On observe alors que l'électromigration peut altérer localement les propriétés du matériau et peut être complètement inversée dans Al, partiellement dans $\text{La}_{2-x}\text{Ce}_x\text{CuO}_4$ alors qu'elle est plutôt irréversible dans Nb. Elle induit des changements de structure clairs dans Al tandis que dans Nb et $\text{La}_{2-x}\text{Ce}_x\text{CuO}_4$ des mécanismes plus complexes sont à

l'oeuvre, ce qui pourrait expliquer leur irréversibilité. En plus de la possibilité d'obtenir des tailles inférieures à celles atteintes par les techniques de lithographie standard, la réversibilité du processus peut faire office de puissant outil complémentaire pour ajuster finement les propriétés d'une jonction donnée. Une méthode de pulses de courant, facile à implémenter et permettant une électromigration plus rapide et tout aussi efficace, est également présentée.

En suivant cette approche, l'électromigration contrôlée est utilisée pour contracter des nanoconstrictions en Al. Nous démontrons qu'une transition, de glissements de phase assistés thermiquement vers des glissements de phase quantiques, a lieu lorsque la section transverse devient inférieure à $\sim 150 \text{ nm}^2$. Dans le régime dominé par les glissements de phase quantiques, le nanofil perd sa capacité à conduire le courant sans dissipation, et ce même à la plus basse température atteignable. Nous montrons aussi que des constrictions supraconductrices électromigrées manifestent une magnéto-résistance négative à faibles champs magnétiques, ce qui peut être attribué à la suppression de la supraconductivité au niveau des contacts.

Au moment où ce travail de thèse a commencé, la plupart des études s'étaient concentrées sur des longs nanofils où plusieurs glissements de phase peuvent cohabiter et apparaître aléatoirement le long du nanofil. Dans le présent travail, nous étudions des glissements de phase hautement confinés au point de contact entre deux nanofils supraconducteurs. Le procédé d'électromigration nous permet de réduire in situ la dimension latérale de la nanoconstriction et donc d'investiguer, sur le même échantillon, les glissements de phase thermiques et la fonction de densité de probabilité du courant de commutation nécessaire pour déclencher une avalanche d'événements. De plus, pour un courant appliqué supérieur au courant de commutation, l'existence de deux régimes thermiques distincts est mise au jour. Le premier correspondant à une évacuation de la chaleur efficace où la température de la constriction et celle du bain restent donc proches l'une de l'autre, et le second pour lequel la température de la constriction peut largement excéder celle du bain menant donc à la formation d'une région normale stationnaire appelée point chaud.

Dans le dernier chapitre expérimental de cette thèse, nous présentons des résultats préliminaires concernant la dépendance en température de la densité de courant $J_{EM}(T)$, au-dessus de laquelle la migration atomique a lieu, pour plusieurs supraconducteurs. En ce qui concerne les supraconducteurs à haute densité de courant critique $J_c(T)$, comme $\text{YBa}_2\text{Cu}_3\text{O}_{7-\delta}$, $J_{EM}(T)$ intersecte $J_c(T)$ à une certaine température T^* . Dès lors, pour $T < T^*$ l'état supraconducteur dissipatif ne peut plus être atteint sans que cela ne mène à des modifications irréversibles des propriétés du matériau. Ce phénomène pourrait aussi constituer un mécanisme non-négligeable de détérioration locale de l'échantillon dans les films supraconducteurs à haute température critique soumis à des pénétrations abruptes d'instabilités thermomagnétiques.

Acknowledgements

Who would I be to pretend that this work is the product of my sole contribution? I think scientific research teaches humility, and it is thus full of humbleness that I can happily thank the countless people that have a part in it. Most of them had to support a huge burden: me and my unbearable jokes constantly bothering them and asking for help.

I would like to start by thanking the Physics department of Uliège for giving me the opportunity to pursue a thesis as part of my assistant position.

My deepest thanks go to the members of my jury for taking the time to review my manuscript and to attend my defense.

I also want to acknowledge Ngoc Duy Nguyen, member of my thesis committee, for his advice during these five years.

I express many thanks to Médéric Mélard and Samuel Rondia for the numerous high quality anti-ESD pieces they made for me. Their reaction time and the advice from Médéric have been precious.

Of course, all this work would not have been possible without the high quality samples made by Vyacheslav Zharinov at KULeuven and Roman Kramer in Grenoble. They have earned my everlasting gratitude.

I am also not forgetting the help and support of Mahmoud and Obaïd during my first years as a PhD and Jonathan during the last ones. Their immeasurable kindness and hard work have to be remembered.

I add here a special word for Maxime, in memory of our numerous discussions, especially the ones about drift and diffusion.

I express warm thanks to Francesco Tafuri, Davide Massorotti and Roberta Caruso for welcoming me in their lab and for doing a great job at helping me with my measurements.

Even details matters, so I would like to have a special thought for Benoit Vanderheyden and Philippe Vanderbemden who have been particularly kind to me during this frightening conference in the country of Uncle Sam.

Thank also to Thierry for the beautiful contrast he brought to my technical figure

of the in situ platform in the SEM.

During my five years of PhD, I had the chance to work and collaborate with amazing colleagues and friends. R  r  my, Sylvano, Guiseppe, Milou,   eljko and Sunil (from the south), as well as Jeroen, Slava, Mathias and Ritika (from the north) are the funniest, nicest and most hard-working people you could ever wish to work with. This was a great chance for me to have them.

Among the northerners, was standing a man who played a bit the role of a supervisor when I was measuring at KULeuven. So, I would like to deeply thank Joris Van de Vondel for his careful guidance and help. He was very welcoming and patient with the young and sometimes a bit scared PhD student that I was.

I cannot find the words to describe how grateful I am to Alejandro Silhanek for giving me the opportunity to join his group and pursue a PhD thesis under his supervision. He is probably one of the most humble person I know. He tried to teach me the value of hard work and made me a little less lazy. He helped me with a considerable amount of ideas and suggestions, not to mention corrections. He was able, at the same time, to be comprehensive and to nag enough for me to overcome the barrier. I wish him the best for the future, I hope to work again with someone like him.

Inside and outside the University, I had also the chance to have great friends. It is probably a bit strange to thank them for being what they are but I can still thank them for the joy they bring me. So thank you Antoine D., Antoine N., Aurore, C  lia, Cl  mentine,   lodie,   ric, Fran  ois, Gilles, Julien, Justine, Kevin, Laurie, Lionel A., Lionel P., Lory, Ludivine, Ludovic, Marie-Julie, Mathieu G., Mathieu M., Maxime, M  lanie, Nicolas, Philip, Pierre-Yves, Sarah, Simon and Valentine. Merci Simon et Antoine pour votre relecture.

Merci aussi    ma famille, pour leur soutien et leur amour inconditionnels. Merci pour tout Maman, Papa, St  phane, France et Pierre. Merci soeurette et caillou pour votre relecture attentive.

Finally, I would like to have a word for someone who "only" had to endure the last year of my thesis. Her smile is shining more than any other, it keeps making my heart skip a beat.



Veritatem inquirenti, semel in vita de omnibus, quantum fieri potest, esse dubitandum.

René Descartes

Contents

Abstract	6
Résumé	8
Acknowledgements	11
List of abbreviations	19
List of symbols	20
Introduction	23
1 Phase slippage in superconductors	29
1.1 Introduction	30
1.2 Superconductivity in a nutshell	30
1.2.1 Superconducting state: general properties	30
1.2.2 The two-fluid model	32
1.2.3 Ginzburg-Landau equations	34
1.2.4 Josephson effect	36
1.2.5 Magnetic classification of superconductors	36
1.2.5.1 Demagnetizing factor	36
1.2.5.2 Ginzburg-Landau parameter	37
1.2.5.3 Critical fields	39
1.2.6 Persistent currents in a superconducting ring	40
1.2.7 Fluxoid quantization	41
1.3 Fluctuation effects in superconductors	43
1.3.1 Dissipation in a thin superconducting wire	43
1.3.1.1 Qualitative picture	43
1.3.1.2 Quantitative considerations	44
1.3.2 Thermally Activated Phase Slips (TAPS)	45
1.3.3 Quantum Phase Slips (QPS)	47

2	Electromigration in metals	49
2.1	Introduction	50
2.2	Historical context	50
2.3	Physics of atomic diffusion under electron wind	51
2.3.1	Electron-lattice interaction	51
2.3.2	Static and dynamic perturbations	52
2.3.3	Mass flux	54
2.3.4	Activation factors	57
2.3.4.1	Effect of temperature	57
2.3.4.2	Effect of grain structure	58
2.3.4.3	Size effects	58
2.3.5	Improving the resistance to electromigration	60
2.4	Controlling atomic migration: state of the art	60
2.4.1	Layout of the structures	61
2.4.2	Control loop	61
2.4.2.1	Limitations of voltage-driven self-controlled EM . . .	61
2.4.2.2	Electronic control loop	63
2.5	Controlling atomic migration: the software	64
2.5.1	Choice of the process variable	64
2.5.2	Pure software-based feedback loop	64
3	Experimental techniques	67
3.1	Introduction	68
3.2	Sample fabrication and observation	68
3.2.1	Raith PIONEER Two electron microscope	68
3.2.1.1	Scanning Electron Microscopy	69
3.2.1.2	Electron Beam Lithography	70
3.2.1.3	In situ observation during transport measurements . .	71
3.2.2	Fabrication processes	72
3.2.2.1	Al nanoconstrictions	72
3.2.2.2	Nb nanoconstrictions	74
3.2.2.3	YBa ₂ Cu ₃ O _{7-d} and La _{2-x} Ce _x CuO ₄ microstructured bridges	74
3.3	Cryogenics and noise filtering	76
3.3.1	Oxford continuous flow ⁴ He cryostat	76
3.3.2	Oxford ³ He refrigerator	78
3.3.3	Montana closed-cycle cryostation	79
3.3.4	Relevant types of noise in the system	80
3.3.4.1	Johnson-Nyquist noise	80
3.3.4.2	Shot noise	81

3.3.4.3	Flicker noise	81
3.3.4.4	Coupled noise	81
3.4	Avoiding electrostatic discharges	81
3.4.1	Sample holder	82
3.4.2	Wirebonding	83
3.4.3	Installation	84
3.4.3.1	Cryogenic environment	85
3.4.3.2	Electron microscope	86
3.4.4	End of installation	87
4	Anti-electromigration of superconducting nanowires	89
4.1	Introduction	90
4.2	Investigation of anti-electromigration on conventional and high- T_c superconductors	90
4.2.1	Samples technical details	91
4.2.2	Electromigration of Al nanoconstrictions	93
4.2.3	Electromigration of Nb nanoconstrictions	96
4.2.4	Electromigration of LCCO microconstrictions	99
4.2.5	Electropulsing	102
4.3	Conclusions	103
5	Transition between phase slips dominated regimes in narrowed superconducting wires	105
5.1	Introduction	106
5.2	Structural characterization	107
5.3	Characterization of electromigration	108
5.3.1	TPS to QPS transition for electromigrated constrictions	111
5.4	Conclusions	117
6	Localized phase slips statistics in narrowed superconducting junctions	119
6.1	Introduction	120
6.2	Evidence of weak to strong self-heating transition	121
6.3	Switching current distributions	126
6.4	Methods	133
6.5	Conclusions	135
7	Current-induced atomic diffusion limits the dissipative state of high T_c superconducting bridges	137
7.1	Introduction	138

7.2 Electromigration current density vs critical current density	138
7.3 Conclusions	142
Conclusion and perspectives	143
Bibliography	147
Curriculum Vitae	161

List of abbreviations

BCS	Bardeen-Cooper-Schrieffer.....	31
BNC	Bayonet Neill-Concelman	71
CSD	chemical solution deposition.....	74
DPT	dissipative phase transition	117
EBL	electron beam lithography.....	68
EM	electromigration	25
ESD	Electrostatic discharges	81
FPGA	field programmable gate array	63
GL	Ginzburg-Landau	34
GZ	Golubev-Zaikin	47
HEPA	high efficiency particulate air.....	69
IPA	isopropyl alcohol	73
LAMH	Langer-Ambegaokar-McCumber-Halperin.....	47
LCCO	Lanthanum cerium copper oxide	68
MBB	make-before-break	82
MBE	molecular beam epitaxy.....	73
MIBK	methyl isobutyl ketone.....	73
NMR	negative magneto-resistance	107
PCB	printed circuit board	82
PS	phase slip.....	43
PID	proportional-integral-derivative.....	63
PLD	pulsed laser deposition	74
PVD	physical vapor deposition	72
PMMA	poly(methyl methacrylate).....	72

QPS	quantum phase slips	47
RIE	reactive ion etching	72
RRR	residual resistivity ratio	95
SE	secondary electrons	69
SEM	scanning electron microscope	50
SNSPD	superconducting nanowire single photon detector	25
TAPS	thermally activated phase slips	47
TDGL	time-dependent Ginzburg-Landau	47
YBCO	Yttrium baryum copper oxide	27

List of symbols

Roman

A	magnetic vector potential
B	magnetic induction
C	concentration of vacancies
\mathcal{C}	specific heat
D	diffusion constant
E	(applied) electric field
e	electron charge
e^*	condensed electron charge
$e(t)$	error of setpoint from process variable
f_n	normal free energy density
f_{nl}	voltage feedback reaction
f_s	superconducting free energy density
f_{PID}	response function of PID controller
F_{wind}	electron wind force
G	conductance
G_j	conductance of the junction
G_T	total conductance
h	Planck constant
\hbar	reduced Planck constant
\mathcal{H}_0	hamiltonian of unperturbed crystal
\mathcal{H}	hamiltonian of crystal including perturbations
H	magnetic field

Greek

α	Stekly parameter
α_T	Thermal coefficient
Γ_{QPS}	rate of quantum phase slips
δ	thermal healing length
Δ	superconducting gap
ΔF	free energy barrier for phase slips
ϵ	RMS noise value
ϵ_c	Thouless energy scale
η	demagnetizing factor
Θ_m	mass flux
Θ_v	vacancy flux
κ	Ginzburg-Landau parameter
λ	superconducting penetration depth
λ_F	Fermi wavelength
Λ_Q	charge imbalance length
μ	mobility
μ_0	magnetic permeability of free space
ν	frequency
ν_c	characteristic frequency
ξ	superconducting coherence length
ρ	resistivity
σ	conductivity

H_a	applied magnetic field	σ_{ns}	surface energy at normal/ superconductor interface
H_c	thermodynamic critical field	τ	characteristic time between two collisions
H_{c1}	first critical field	τ_0	characteristic response time of the superconductor
H_{c2}	second critical field	τ_{GL}	characteristic relaxation time in TDGL theory
H_{c3}	third critical field	τ_{PS}	lifetime of the footprints left by a phase slip
H_{demag}	demagnetizing field	τ_E	quasiparticles thermalization time
I	electric current	Υ	heat transfer coefficient
I_{EM}	electromigration current	φ	superconducting phase
I_c	critical current	Φ_B	magnetic flux
I_n	normal component of current	Φ_0	magnetic flux quantum
I_{ret}	retrapping current	Φ'	fluxoid
I_{sw}	switching current	χ	thermal conductivity
I_s	superconducting current	$\psi_e(\mathbf{r})$	electronic wavefunction
J	current density	ψ_s	superconducting order parameter
J_c	critical current density	$\psi_s(\mathbf{r})$	superconducting wavefunction
J_{EM}	electromigration current density	ω	pangular velocity
J_n	normal current density	Ω	attempt frequency for phase slips
J_s	superconducting current density		
J_{tot}	total current density		
K_j	Josephson constant		
k_B	Boltzmann constant		
ℓ	mean free path		
L	length		
\mathcal{L}	inductance		
M	magnetization		
m_e	electron mass		
m^*	condensed electron mass		
N	number of particles		
N_{PS}	number of phase slips needed to trigger a switch		
n	density of charge carriers		
n_n	normal electrons density		
n_s	superconducting electrons density		
p	process variable		
P	power		

P_{in}	heat generation
P_{out}	heat removal
P_j	power dissipated in the junction
P_R	power dissipated in the device
q^*	effective charge
R	resistance
R_d	differential resistance
R_j	resistance of the junction
R_L	resistance of the leads
R_N	normal resistance
R_q	resistance quantum
R_W	resistance of the wires (half of)
S	cross section
S_{QPS}	effective action
S_ω	power spectral density
t	thickness
T	temperature
T_B	bath temperature
T_c	critical temperature
T_{th}	threshold temperature
U	activation energy
V	voltage
v_d	critical velocity (of the charge carriers)
v_d	drift velocity
v_e	electron velocity
v_{EM}	electromigration drift velocity
v_s	superfluid velocity
w	width
W	perturbation
Z	impedance
Z^*	effective valence

Introduction

Superconductors were discovered at the beginning of the last century and have been, since then, involved in various cutting edge technologies. From magnetic resonance imaging to particle accelerators, probably their most visual and impressive application for the general public remains the magnetic levitation.

From late '60s, the advent of nanotechnologies strongly impacted numerous fields and superconductors were of course no exception. Quantum computation based on superconducting circuits has emerged as a serious candidate to replace current electronics, as it has been demonstrated that systems based on qubits greatly improve computation capabilities. Indeed, the need for increasing computing power continuously demands alternative technological advances to standard electronics which will eventually reach the limit of achievable miniaturization and give rise to a breakdown of Moore's law.

In 2016 IBM has made quantum computing available on a cloud platform¹. The quantum processor was made of five superconducting qubits and the firm already envisions 50-100 qubits processors available in the next decade. In another technological vein, superconducting nanowire single photon detectors (SNSPDs) are the fastest individual photon counters that are already in the market. Their applications range from quantum key distribution² to LIDAR³, successor of RADAR⁴. In this context, it is of fundamental importance to better understand their superconducting behaviour at low dimensions, especially the undesired and harmful appearance of thermal and quantum fluctuations of the superconducting order parameter as the wire width shrinks.

One of the most limiting factor to this investigation is the attainable size, even with the resolution of the most advanced lithography techniques. An innovative approach is proposed here, a historically detrimental process known as electromigration (EM) and consisting of the displacement of atoms in conducting materials submitted to large current densities.

¹See <https://www-03.ibm.com/press/us/en/pressrelease/49661.wss>.

²A secure communication method which implements a quantum cryptographic protocol.

³Light detection and ranging.

⁴Radio detection and ranging

The objective of this work is, on the one hand, to explore the capability of EM as a new nanofabrication tool for making superconducting junctions, and on the other hand, to apply this technique in order to study the superconducting properties of nanowires and nanoconstrictions, especially the dynamics of phase fluctuations. This has been achieved through the investigation of superconducting bow-tie nanostructures, where EM is used to gradually modify the material properties.

This thesis is structured as follows:

In **Chapter 1**, we briefly review some essential concepts of superconductivity required for the understanding of the rest of this thesis. We start by covering the basics of superconductivity, introducing its electrodynamics via the two-fluid model, the Ginzburg-Landau theory and the magnetic behaviour of superconductors. We finally dwell on the concept of fluctuations of the superconducting phase that induce dissipation and can be of either thermal or quantum origin.

Chapter 2 reviews the phenomenon of atomic migration under an electron wind, known as electromigration. The physics of the process is first presented and its triggering factors are explained. We then focus on how it is possible to master it through a control feedback loop.

Chapter 3 describes the experimental aspects and developments of this work. We present the necessary tools for lithography and visualization as well as for cooling at very low temperatures. We also highlight the problematic of noise and required filtering in the different systems. We end the chapter with a full description of the sample's installation procedure intended to avoid electrostatic discharges.

In **Chapter 4**, we present the results of EM on conventional and high- T_c superconductors along with particular emphasis on the reversibility of the process. We show, in some cases, full reversibility of the phenomenon and the possibility to fine-tune the resistance of the device. In the case of partial or total irreversibility, other complex mechanisms than only mass flux are highlighted.

In **Chapter 5**, we propose to use EM to gradually reduce the size of a superconducting nanoconstriction in order to study the transition between two regimes dominated by phase fluctuations. Following this approach, we are able to specify a value for the cross-section where the transition from thermal to quantum fluctuations takes place. In addition, we provide compelling evidence necessary to explain the negative magneto-resistance and furthermore, we reach the limit of one quantum of conductance where a superconducting/insulator transition is observed.

Chapter 6 focusses on dynamics of phase fluctuations in superconducting nanojunctions and permits to highlight the existence of two thermal regimes materialized by reversibility or irreversibility of current-voltage characteristics. We propose an in-

terpretation of the physical mechanisms involved. We also study the distribution of critical currents and are able to explain the observed distributions with a model solely including thermal fluctuations.

In **Chapter 7**, we measure and compare the values of critical and EM currents in a conventional and a cuprate superconducting material, namely Al and Yttrium baryum copper oxide (YBCO). While, for Al, the critical current density J_c is always lower than the current density needed to trigger EM, J_{EM} , for YBCO, J_{EM} can become lower than J_c below certain temperature.

Chapter 1

Phase slippage in superconductors

1.1 Introduction

In this chapter, we introduce some essential concepts on superconductivity required to understand the rest of this thesis. The two main particularities of the superconducting state, namely the absence of electric resistance and the extreme diamagnetic response, are briefly presented. We explain the concepts of critical temperature, critical current density and critical magnetic field. Concerning electrodynamics, a simple model based on the combination of two fluids is presented in order to understand the dissipation at non-zero frequencies.

As it will be central in this thesis, the concept of superconducting phase is also introduced followed by the main results of the Ginzburg-Landau theory and a brief illustrative description of the Josephson effect.

Superconductors react differently to an applied magnetic field, due to their shape or type. Magnetic classification of superconductors is therefore presented and allows to define their different critical fields.

The property of zero resistance allows us to imagine that if we would feed current through a superconducting loop, this current will flow forever. The concept of persistent currents is then discussed for the particular case of a superconducting ring. The observed decay of these currents can only be explained by invoking dissipative fluctuations. These variations of the superconducting order parameter, of thermal or quantum origin, are presented with some details. They are responsible for the appearance of resistance at the nanoscale, even if the material lies deeply in the superconducting state.

1.2 Superconductivity in a nutshell

We shall start by presenting the main characteristics of the superconducting state and discuss the persistent currents, made possible by the absence of resistance.

1.2.1 Superconducting state: general properties

Superconductivity is a macroscopic quantum state of matter discovered in 1911 by Heike Kamerlingh Onnes^[1]. The superconducting state of a material possesses two fundamental hallmarks: zero electric resistance and expulsion of magnetic field. In other words, a superconductor exhibits, under certain conditions, perfect electric conductivity and perfect diamagnetism.

Transport of electric current without opposing any resistance means that there are no energy losses. This ability to carry dissipationless current arises from a macroscopic quantum effect resulting from the condensation of electron pairs, called Cooper pairs^[2],

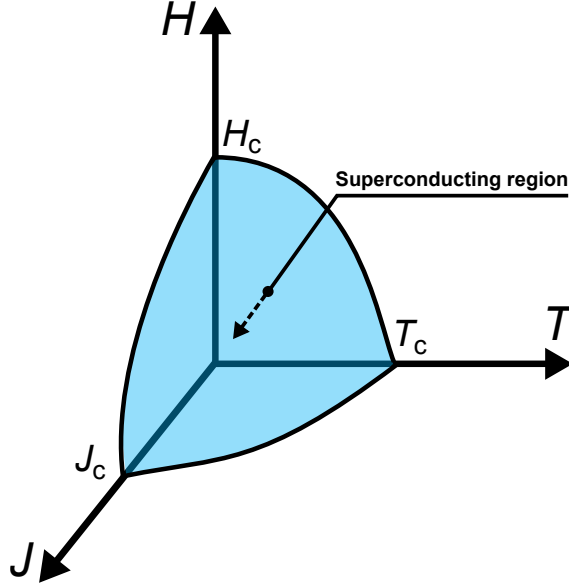


Figure 1.1: **Typical phase diagram of a superconductor.** The superconducting state is limited by a critical temperature T_c , a critical magnetic field H_c and a critical current density J_c .

in the ground-state energy. This latter is separated from the dissipative state by a energy gap Δ . The subsequent superconducting electron pairs are described, in the framework of the Bardeen-Cooper-Schrieffer (BCS) theory^[3], by a single macroscopic wavefunction. The characteristic distance for the variations of the superconducting electrons density n_s , for instance between superconducting and normal regions, is called the coherence length ξ .

Being a perfect diamagnet means that a magnetic field should be completely expelled from the material. When a superconductor is immersed in a magnetic field H , it induces supercurrents that generate a magnetization \mathbf{M} such that $\mathbf{B} = \mu_0(\mathbf{H} + \mathbf{M})$ is nearly zero in its bulk. The London theory^[4] furnished the first description of this phenomenon, named the Meissner-Ochsenfeld effect after its discoverers^[5]. The characteristic distance for the decay of the magnetic field at the surface of the superconductor is called the magnetic penetration depth λ and represents the second main characteristic length of a superconductor.

A material which has the potential to be a superconductor will be in its superconducting state if three conditions are fulfilled: it has to be cooled down below its critical temperature T_c , the magnetic field in which it is supposedly immersed has to be lower than its critical field H_c and the current to which it is subjected has to be such that its current density is lower than that certain critical current density J_c (see Figure 1.1).

Nevertheless, we have to anticipate that the two previously cited fundamental hallmarks of a superconductor will be put in jeopardy when it comes to a certain class of superconductors, said to be of type II. In these materials, magnetic field is allowed to penetrate in form of quantized units of flux which, once in motion, led to dissipation. In any case, the superconducting state can be described by a many-particle condensate wavefunction $\psi_s(\mathbf{r})$, with amplitude $|\psi_s(\mathbf{r})|$ and phase φ , so that it can be written as

$$\psi_s(\mathbf{r}) = |\psi_s(\mathbf{r})|e^{i\varphi(\mathbf{r})}. \quad (1.1)$$

The condensate maintains phase coherence over macroscopic distances and one regularly talks about Bose condensation of Cooper pairs, which can be seen as analogous (although not identical) to Bose-Einstein condensation. The BCS theory actually explains that, by taking into account electron-phonon interactions, one can obtain electron-electron attraction. As a result, a part of the electrons forms Cooper pairs with zero total spin, thus obeying Bose-Einstein statistics. The charge carrier, i.e. a Cooper pair, has naturally a total charge of $2e$.

Finally, we can mention that a Heisenberg uncertainty exists between any two non-commuting variables of a quantum-mechanical system, thus here between the conjugate variables number of particles N and phase φ ,

$$\Delta N \Delta\varphi \geq 1. \quad (1.2)$$

This relation limits the precision with which N and φ can be simultaneously known and has been experimentally demonstrated in the 90's^[6]. The physical significance of the superconducting phase was first emphasized in the work of B. D. Josephson^[7].

1.2.2 The two-fluid model

The two-fluid model describes the electrodynamics that results from the superposition of the response of two families of charge carriers, one made of normal electrons (or more precisely Bogoliubov quasiparticles¹) with density n_n and one composed of superconducting electrons with density n_s . It is a simple and useful model to understand, for example, the vulnerability of superconductivity under non-zero frequency excitations. Since the total current density is constant, we have

$$\mathbf{J}_{tot} = \mathbf{J}_s + \mathbf{J}_n. \quad (1.3)$$

It is based on the Drude model that assumes a gas of free electrons whose only inter-

¹A Bogoliubov quasiparticle is a broken Cooper pair where the term "quasiparticle" means that these are electrons as affected by the other forces and interactions in the solid. This implies slight modifications in their mass (effective mass) and electric field (electric field screening).

actions with the environment are made via collisions. This classical model, neglecting any long range interactions, gives an electronic equation of motion

$$m_e \dot{\mathbf{v}}_e = e\mathbf{E} - m_e \frac{\mathbf{v}_e}{\tau}, \quad (1.4)$$

where m_e is the electronic mass, v_e its speed, \mathbf{E} the applied electric field and τ the characteristic time between two collisions. It also gives the linear relationship between current density \mathbf{J} and electric field \mathbf{E}

$$\mathbf{J} = \sigma(\omega)\mathbf{E}, \quad (1.5)$$

where

$$\sigma(\omega) = \frac{\sigma_0}{1 + i\omega\tau} = \frac{\sigma_0}{1 + \omega^2\tau^2} - i\omega\tau \frac{\sigma_0}{1 + \omega^2\tau^2} \quad (1.6)$$

is the frequency-dependent conductivity for an electric field of the form $\mathbf{E}(t) = \mathbf{E}e^{i\omega t}$ with $\sigma_0 = \frac{ne^2\tau}{m}$ and n the density of charge carriers.

Limiting the frequencies below the superconducting gap Δ^2 and performing some elementary integrations^[8], the combined response of the two fluids to an electric field writes as follows,

$$\Re[\sigma(\omega)] = \frac{\pi n_s e^2}{2m} \delta(\omega) + \frac{n_n e^2 \tau_n}{m}, \quad (1.7h)$$

$$\Im[\sigma(\omega)] = \frac{n_s e^2}{m\omega}. \quad (1.7i)$$

We can see that at zero frequency, the imaginary part of the conductivity (Eq. 1.7i) tends to infinite, thus making of the supercurrent response a zero-impedance shunt.

At any non-zero frequency, given the Dirac delta function in Eq. 1.7h, we are left with a conductivity $\sigma(\omega) = \frac{n_n e^2 \tau_n}{m} + i \frac{n_s e^2}{m\omega}$. A common given analogy is an electric circuit with $\Re[\sigma(\omega)]$ the conductance $1/R$ of a resistive channel in parallel with $\Im[\sigma(\omega)]$ the admittance $1/i\omega\mathcal{L}$ of an inductive channel. The characteristic frequency $\omega_c = R/\mathcal{L}$ of this circuit allows to discriminate between the lossless inductive channel ($\omega < \omega_c$) and the dissipative resistive channel ($\omega > \omega_c$) for bearing the dominant current flow. In our case, the ratio of current densities in the two channels is

$$\frac{J_s}{J_n} = \frac{n_s e^2 / m\omega}{n_n e^2 \tau_n / m} = \frac{n_s}{n_n \omega \tau_n}, \quad (1.10)$$

and the crossover frequency is equal to $\sim n_s / n_n \tau_n \approx 100 \text{ GHz}$ (far infrared)³. Below this frequency, most of the current will be carried as supercurrent but there will always

²The superconducting gap is of the order of $k_B T_c$, so $\Delta \sim 10^{-4} \text{ eV}$.

³ τ_n is typically of the order of a picoseconds.

be non-zero dissipation at any non-zero frequency coming from the normal component of the current.

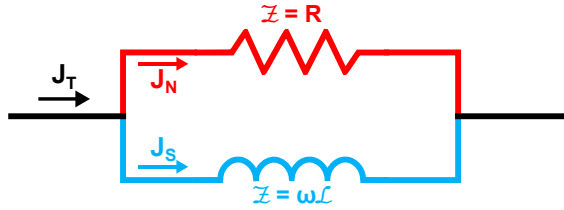


Figure 1.2: **Illustrative analogy for the two-fluid model.** At zero frequency, the inductive channel acts as a zero-impedance shunt. At any non-zero frequency, there is dissipation into the resistive channel.

1.2.3 Ginzburg-Landau equations

In the previous sections, we already cited two theories attempting to give a description of superconductivity: the classic London theory and the microscopic BCS theory. There is a third one, phenomenological, developed by V. L. Ginzburg and L. D. Landau^[9]. It is based on the pre-established Landau theory for second-order phase transitions and uses the concept of order parameter ψ_s lately demonstrated by Lev Gorkov^[10] that is related to the wavefunction of the condensed electrons. The order parameter $\psi_s(\mathbf{r})$ measures the breaking of symmetry in the superconducting state and $|\psi_s(\mathbf{r})|^2$ represents the local density of superconducting electrons, $n_s(\mathbf{r})$. The basic postulate of the Ginzburg-Landau (GL) theory is that if ψ_s is small and varies slowly in space, the free-energy density f can be expanded in powers of $|\psi_s|^2$ and $|\nabla\psi_s|^2$, which gives a series of the form^[9]

$$f_s = f_n + \alpha|\psi_s|^2 + \frac{\beta}{2}|\psi_s|^4 + \frac{1}{2m^*} \left| \left(\frac{\hbar}{i} \nabla - e^* \mathbf{A} \right) \psi_s \right|^2 + \frac{\mu_0 H^2}{2}, \quad (1.11)$$

where α and β are expansion coefficients, m^* and e^* are respectively the mass and the charge of the condensed electrons, and \mathbf{A} is the vector potential. Let us take the occasion to introduce the notion of condensation energy, which is by definition the free-energy difference between the normal and superconducting states in zero field, $f_n - f_s$. The thermodynamic critical magnetic field of a superconductor can be obtained by equating the magnetic energy per unit volume $B^2/2\mu_0$, associated with holding the field out against the magnetic pressure (cf. Meissner effect), with this condensation energy, that is to say

$$f_n - f_s = \frac{\mu_0 H_c^2}{2}. \quad (1.12)$$

In the absence of fields and spatial variations, Eq. (1.11) can be reduced to^[8]

$$f_s = f_n + \alpha |\psi_s|^2 + \frac{\beta}{2} |\psi_s|^4. \quad (1.13)$$

Examining Eq. (1.13), we see that β has to be positive, otherwise the lowest free-energy would occur at arbitrarily large values of $|\psi_s|^2$, which is non-physical. As it is depicted in Figure 1.3, two cases then arise, depending on whether α is positive or negative. In the former case, the minimum of f occurs at $|\psi_s|^2 = 0$ (normal state) while in the latter, the minimum is achieved for^[8]

$$|\psi_s|^2 = -\frac{\alpha}{\beta} \equiv \psi_{s,\infty}^2. \quad (1.14)$$

To sum up, α is temperature dependent, being negative in the superconducting state and changing sign at T_c , which is defined as *the highest temperature at which $|\psi_s|^2 \neq 0$* ^[8].

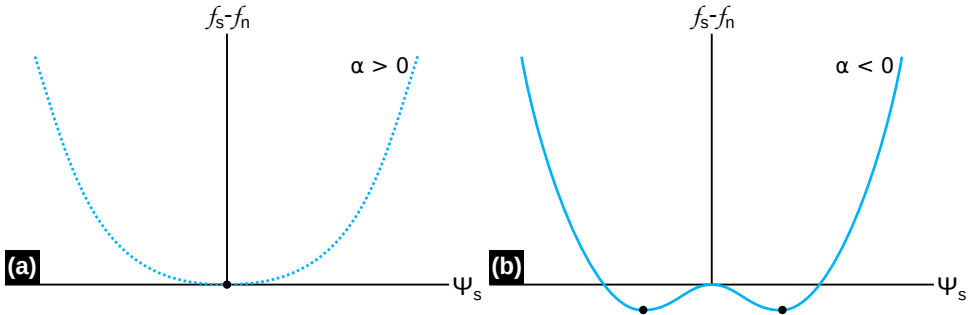


Figure 1.3: **Ginzburg-Landau free-energy functions for $T > T_c$ ($\alpha > 0$) and $T < T_c$ ($\alpha < 0$).** The dots indicate equilibrium positions. The vertical axis represents the free-energy difference between the superconducting and normal states while the horizontal axis represents values of ψ_s , which has been taken to be real for simplicity.

The overall free-energy is given by the volume integral of Eq. 1.11. This variational energy has to be minimized with respect to variations of the order parameter and the vector potential. Like any complex number, the order parameter has a modulus and a phase $\psi_s(\mathbf{r}) = |\psi_s(\mathbf{r})|e^{i\varphi(\mathbf{r})}$, then the obtained GL equations can be written as^[9]

$$\alpha\psi_s + \beta|\psi_s|^2\psi_s + \frac{1}{2m^*} \left(\frac{\hbar}{i} \nabla - e^* \mathbf{A} \right)^2 \psi_s = 0, \quad (1.15)$$

$$\mathbf{J}_s = \frac{e^*}{m^*} |\psi_s|^2 (\hbar \nabla \varphi - e^* \mathbf{A}) = e^* n_s \mathbf{v}_s, \quad (1.16)$$

where $v_s = \frac{1}{m^*} (\hbar \nabla \varphi - e^* \mathbf{A})$ is the superfluid velocity. Gor'kov later demonstrated that the GL theory could be derived from the BCS theory^[10] close to T_c . His calcula-

tions also showed that $e^* = 2e$ and $m^* = 2m$, that is to say that condensed electrons are actually electron pairs.

1.2.4 Josephson effect

The electrons of a superconducting condensate are described by a single wavefunction, meaning that they all have the same phase φ . In 1961, Josephson^[7] made a remarkable prediction that would earn him the Nobel prize a few years later. He stated that a zero voltage supercurrent should flow between two superconducting electrodes separated by a thin insulating barrier. If $\Delta\varphi$ is the difference of phase between the two wavefunctions describing each electrode and I_c the maximum supercurrent that the junction can support before switching to a dissipative state (i.e. its critical current), then the tunnel current between electrodes can be expressed as follows,

$$I_s = I_c \sin \Delta\varphi. \quad (1.17)$$

He further predicted that if a voltage difference V were to be maintained across the junction, the phase difference $\Delta\varphi$ would evolve according to

$$\dot{\Delta\varphi} = \frac{2eV}{\hbar}, \quad (1.18)$$

so that the current would be of amplitude I_c and alternating at frequency $2eV/\hbar$.

1.2.5 Magnetic classification of superconductors

Superconductors respond to an externally applied magnetic field in a rather exotic fashion as we have seen by mentioning the Meissner state where they exhibit perfect diamagnetism. However, their magnetic behaviour is even more complicated and depends mainly on two factors: their shape via the notion of demagnetization field and the ratio between their magnetic penetration depth λ and their superconducting coherence length ξ . This latter factor, called the Ginzburg-Landau parameter, is at the base of their classification in two types, type I and type II.

1.2.5.1 Demagnetizing factor

The response to an applied magnetic field H_a depends on the shape of the superconductor. This is due to the magnetic field generated by the magnetization M , called demagnetizing field or stray field, whose form is often difficult to calculate. However, for the special case of ellipsoids, the demagnetization field is linearly related to the

⁴The Josephson constant $K_J = 2e/h$ is equal to 483597.9 GHz/V and is used, via the AC Josephson effect, as the international standard of voltage.

magnetization by a geometry dependent constant called the demagnetizing factor η , hence

$$H_{demag} = \eta M. \quad (1.19)$$

As it is illustrated in Figure 1.4, for the case of a superconductor in the Meissner state, the magnetic field lines are always tangential to the surface of the superconductor and have a higher density when dimensions perpendicular to the field are increased. Therefore, for some $H_a < H_c$, it is expected that the field lines agglomeration can locally exceed H_c and correspondingly, at those places the material becomes normal.

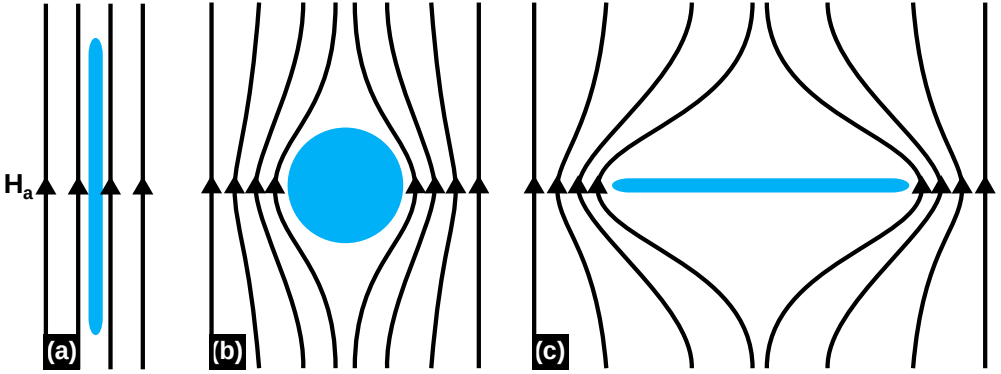


Figure 1.4: **Magnetic field lines density around superconductors of diverse shapes.** (a) In the limit of a thin slab parallel to the field lines, demagnetizing effects are negligible. (b) For a sphere, demagnetizing effects are such that density of field lines is more important at the equator. (c) In the extreme case of a thin infinite slab perpendicular to the field, the demagnetizing factor is large and a pronounced agglomeration of field lines is observed at the border of the slab.

A coexistence of alternating superconducting and normal regions is observed within a so-called intermediate state, situated between the Meissner and the normal states. This intermediate state is expected in a range of applied fields given by

$$(1 - \eta)H_c < H_a < H_c. \quad (1.20)$$

The demagnetizing factor ranges from zero (no intermediate state) in the limit of a long slab parallel to the applied field (Figure 1.4(a)) to 1 in the opposite case of an infinite slab in a perpendicular field (Figure 1.4(c)). For a sphere (Figure 1.4(b)), it is equal to $1/3$.

1.2.5.2 Ginzburg-Landau parameter

A method of classification of superconductors is based on the ratio of the magnetic penetration depth λ and the superconducting coherence length ξ , known as the Ginzburg-

Landau parameter

$$\kappa = \frac{\lambda}{\xi}. \quad (1.21)$$

This adimensional ratio aims at comparing diamagnetic energy with condensation energy in order to have the sign of the surface energy σ_{ns} of the interface between a normal and a superconducting region,

$$\sigma_{ns} = (\xi - \lambda)\mu_0 H_c^2 / 2. \quad (1.22)$$

A sketch of the one-dimensional variations of the superconducting order parameter ψ_s and the local magnetic induction h along a normal-superconducting domain wall is presented in Figure 1.5. Qualitatively, it can be seen that for $\kappa \ll 1$ (type I) the surface energy σ_{ns} is positive since there is a region of thickness $\sim (\xi - \lambda)$ from which the magnetic field is held out (contributing to the positive diamagnetic energy) while not enjoying the full condensation energy associated with $\psi_{s,\infty}$. On the contrary, for $\kappa \gg 1$ (type II) in Figure 1.5(b), σ_{ns} is negative.

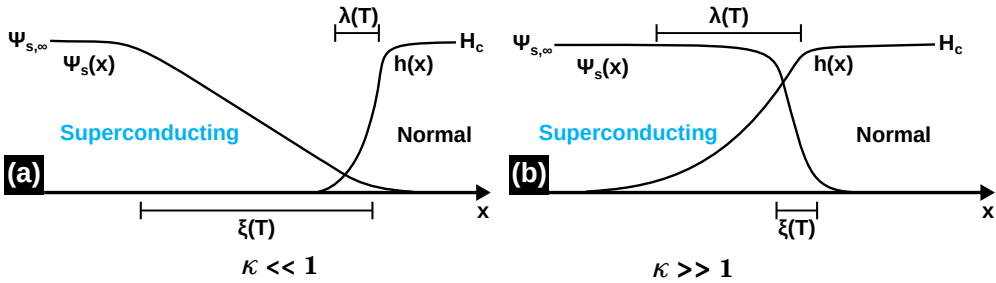


Figure 1.5: **Schematic comparison of ψ_s and h variations at a normal-superconductor domain wall in type I and type II superconductors.** (a) Type I: $\lambda \ll \xi$ and surface energy is positive. (b) Type II: $\lambda \gg \xi$ and surface energy is negative.

The exact crossover from positive to negative energy was found by numerical integration by Ginzburg and Landau^[9] and occurs at $\kappa = 1/\sqrt{2}$, but it was thanks to A. Abrikosov that a full picture of the implications of a negative surface energy at higher values of κ was obtained^[11]. In short, the negative σ_{ns} causes the normal regions (supporting magnetic flux) to subdivide until a quantum limit is reached in which each quantum of flux $\Phi_0 = h/2e = 1/K_j$ passes through the sample as a distinct flux tube called a vortex. These vortices form a regular array named the Abrikosov lattice. This state is called the mixed state and exists only for type II superconductors. In addition, we can now assert that the intermediate state described in the previous section exists only in type I superconductors, whereas the Meissner state remains for both types of superconductors.

1.2.5.3 Critical fields

Since they behave differently when subjected to an external magnetic field, type I and type II superconductors possess their own characteristic fields called their critical fields, at which a phase transition takes place (Figure 1.6). We have already introduced the thermodynamic critical field H_c determined by Eq. 1.12.

We start with H_{c2} , the characteristic field for nucleation of superconductivity in bulk. It is given by

$$H_{c2} = \sqrt{2}\kappa H_c. \quad (1.23)$$

The value $\kappa = 1/\sqrt{2}$ separates type I ($H_{c2} < H_c$) from type II ($H_{c2} > H_c$) superconducting materials. The fact that we have $H_{c2} < H_c$ for type I superconductors indicates the possibility of nucleation of superconductivity at a field inferior to the thermodynamic critical field. The resulting metastable state is analogous to "supercooling" in liquids and gives rise to hysteresis during magnetic field sweeps as sketched in Figure 1.6(b). The nucleation is followed by a discontinuous jump of $|\psi_s^2|$ to $\psi_{s,\infty}^2$, mark of a first-order phase transition. On the contrary, type II superconductors experience a second-order phase transition, with $|\psi_s^2|$ starting up continuously from zero at H_{c2} (Figure 1.6(c)).

A second characteristic field is H_{c3} , associated to nucleation of superconductivity at surfaces. Indeed, since real superconductors are finite in size, behavior at interfaces must be considered. In 1963, Saint-James and de Gennes showed^[12] that superconductivity can nucleate at a metal-insulator interface in a parallel field higher than H_{c2} by a factor of 1.695, so that

$$H_{c3} = 1.695(\sqrt{2}\kappa H_c). \quad (1.24)$$

This means that in a magnetic field parallel to the surface, superconductivity will nucleate in a surface layer of thickness $\sim \xi$ at a field approximately 70 percent higher than that at which nucleation occurs in the volume of the material^[8]. This also implies that superconductivity is more resistant to magnetic field at low dimensions^[13].

There is a third characteristic field called H_{c1} , only for type II superconductors, that is defined by the fact that when $H = H_{c1}$, the free energy must have the same value whether the first vortex is in or out of the sample. This field thus corresponds to the entry of the first flux quantum inside the superconductor. An analytical solution can be found for H_{c1} in the limit of high κ ,

$$H_{c1} = \frac{H_c}{\sqrt{2}\kappa} \ln \kappa. \quad (1.25)$$

This thesis involves superconductors of type-II. Therefore, as we will always refer

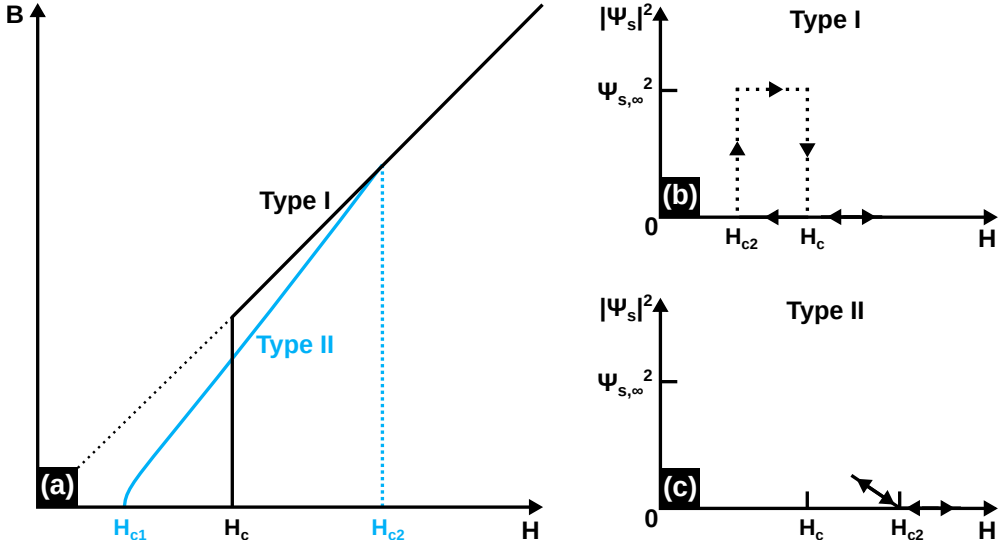


Figure 1.6: **Graphical explanation of critical fields for type I and type II superconductors.** (a) Magnetic field inside the superconductor as a function of the external applied field. H_{c2} corresponds to the nucleation of bulk superconductivity while H_{c1} is defined by the entrance of the first vortex inside a superconductor of type II. (b) Type I: first-order phase transition. In an increasing field, superconductivity can hold up to H_c while in a decreasing field, superconductivity may develop at a lower field $H_{c2} < H_c$. In both cases, $|\psi_s|^2$ experiences an abrupt jump at the transition. (c) Type II: second-order phase transition, no hysteresis is observed. Superconductivity starts to nucleate at $H_{c2} > H_c$, $|\psi_s|^2$ starts up continuously from zero.

to transitions to the normal state, when we write H_c as a designation for the critical field of one sample, the reader can reasonably assume that we mean H_{c2} .

1.2.6 Persistent currents in a superconducting ring

As we stated above, perfect conductivity ensures that charges can flow in a superconductor without any resistance. This effect had been evidenced by Kamerlingh Onnes when observing that the electric resistance of several metals vanished as they were cooled down below their critical temperature. However the most sensitive way to demonstrate the absence of dissipation is the observation of persistent currents in a superconducting ring, as shown in Figure 1.7. Using nuclear resonance to detect any slight decrease in the magnetic field produced by the circulating current, it was established that, once set up, these currents could flow with a lower bond for their characteristic decay time established at 100.000 years^[8].

Such persistent currents can be produced as follows. Let us first start with the ring situated above its superconducting critical temperature T_c and placed in an external axial magnetic field. Then let us cool it down to a temperature below T_c , where the

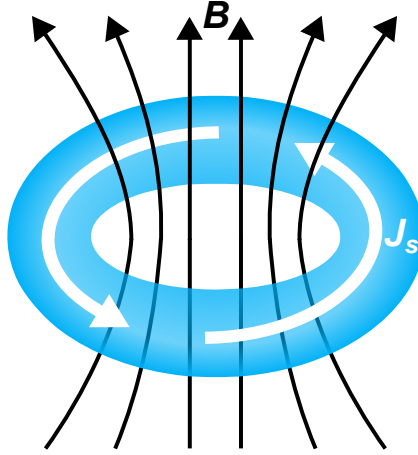


Figure 1.7: **Schematic diagram of a persistent current in a superconducting ring.** The circulating density J_s of superconducting current supports a magnetic field B .

material is superconducting and switch off magnetic field. At the moment when the magnetic field is turned off will appear an induced current compensating for the magnetic flux decrease, according to Faraday's law. Considering the absence of resistance, this current will persist and support the flux through the ring at its initial value. Indeed, if the ring had a finite resistance R and an inductance L , the flux through it would decay in a characteristic time L/R . Here, the resistance being perfectly zero, it takes the flux an infinite time to decay. It is said to be "frozen" while the ring carries a supporting supercurrent, as it is the case in Figure 1.7.

At first sight, it may seem that the trapped magnetic flux could take any value, we will see that this is not the case. Basically, we can be easily convinced that any state of non-zero supercurrent is metastable in the sense that there is a topologically accessible fluctuation which leads to a state of lower current and, therefore, lower free energy^[14]. This latter eventually reaches the global minimum corresponding to zero current.

In 1966, Little showed that thermodynamic fluctuations of the superconducting order parameter should *be able to cause the decay of a "persistent" current in a ring-shaped conductor*. His calculations of the lifetime of these currents indicated that, if the wire was thin enough, the claimed decay should be detectable^[15].

1.2.7 Fluxoid quantization

We have already anticipated that the flux passing through a superconductor cannot take any arbitrary value. In fact, when considering a hole through a bulk superconductor to which an axial flux is applied and subsequently cooled down below its T_c , one

will end up with the field being pushed out of the superconductor (cf. Meissner effect) whereas some "frozen" magnetic flux will remain in the hole. This flux is maintained by supercurrents flowing at the internal surface of the hole.

In order to calculate the resulting trapped flux, let us take a contour inside the superconductor which encloses the hole. In this situation, the path integral of Eq. 1.16 along the contour gives

$$\frac{m}{en_s} \oint_C \mathbf{J}_s \cdot d\mathbf{l} = \hbar \oint_C \nabla \varphi \cdot d\mathbf{l} - 2e \oint_C \mathbf{A} \cdot d\mathbf{l}. \quad (1.26)$$

Taking into account the definition of magnetic flux Φ_B through a contour C delimiting a surface S ,

$$\oint_C \mathbf{A} \cdot d\mathbf{l} = \iint_S \mathbf{B} \cdot d\mathbf{S} = \Phi_B, \quad (1.27)$$

we have

$$\Phi_B + \frac{m}{2e^2 n_s} \oint_C \mathbf{J}_s \cdot d\mathbf{l} = \frac{\hbar}{2e} \oint_C \nabla \varphi \cdot d\mathbf{l}. \quad (1.28)$$

The left member containing the ordinary magnetic flux and the path integral of the supercurrent was named the fluxoid⁵ Φ' , so that we can write

$$\Phi' = \Phi_B + \frac{m}{2e^2 n_s} \oint_C \mathbf{J}_s \cdot d\mathbf{l}. \quad (1.29)$$

One can see directly in Eq. 1.28 that φ is a multiple-valued function; it changes by a certain value after every full circle around the hole. Meanwhile, the wavefunction ψ_s must be single-valued. Therefore, this requires that the change in phase φ after a full circle around the hole containing the magnetic flux must be an integral multiple of 2π , i.e.

$$\oint \nabla \varphi \cdot d\mathbf{l} = 2\pi n, \quad (1.30)$$

where $n = 0, 1, 2, \dots$. Indeed, the addition of $2\pi n$ to the phase leaves the wavefunction unchanged. Eq. 1.28, 1.29 and 1.30 lead to the so-called fluxoid quantization

$$\Phi' = n\Phi_0. \quad (1.31)$$

The fluxoid quantization can be seen as the macroscopic analog to the quantization of angular momentum in an atomic system.

⁵The concept of fluxoid was introduced by F. London.

1.3 Fluctuation effects in superconductors

Superconducting electrons are described by a single macroscopic wavefunction $\psi_{s,0}(\mathbf{r})$ which, at equilibrium, corresponds to the minimum free-energy showed on Figure 1.3(b). However, we will see hereunder that thermodynamic fluctuations will permit to explore other functions $\psi_s(\mathbf{r})$ away from the absolute minimum energy point. This can lead to an increase of resistance and thus dissipation. The following discussion has to be seen in terms of the GL theory.

1.3.1 Dissipation in a thin superconducting wire

1.3.1.1 Qualitative picture

In the framework of the GL theory, we have seen in the last two sections that the requirement to have a persistent current flowing in a ring is that the loop retains the same fluxoid quantum number.

In a single connected superconducting wire, in which current is injected via normal leads, there is a relative phase difference φ_{12} between the two ends. This can be easily understood by referring to Eq. 1.16 from which we can see that $J_s \propto |\psi_s|^2 \nabla \varphi$. In addition, perfect conductivity requires the potential difference V between these two ends to be zero. According to the idea of Josephson formalized in Eq. (1.18), this implies that φ_{12} has to remain constant, with a value depending on the strength of the supercurrent J_s . Actually, φ_{12} fluctuates around a constant mean value, as the supercurrent fluctuates to keep the total current constant (cf. Eq. 1.3) by compensating for charge carriers thermal agitation (Johnson-Nyquist noise). We had indeed demonstrated, in the framework of the two-fluid model, that *at best, a superconductor is really a perfect conductor only for direct current*^[8]. Indeed, for any non-zero frequency, there will be an ac noise voltage reflecting the real part of the ac impedance of the superconductor (cf. Eq. 1.7h).

In order to understand the appearance of resistance, we should again refer to the Josephson relation (1.18). Because if there is resistance, there is a voltage drop across the wire and this means that the averaged φ_{12} should increase with time, which is inconsistent with a steady state. To solve this lack of consistency, we can invoke the occurrence of phase slip (PS) events. As depicted in the chronological scheme of Figure 1.8, if phase coherence is momentarily broken at some point of the superconductor, a slip of the phase can occur before it is re-established. Spatial localization of these events is ensured by the PS being through an integral multiple of 2π , because a uniform phase change by $2n\pi$ outside of the PS region is not physically significant. So maintaining a steady state requires such fluctuations to occur at an average frequency of $2eV/h$. If V is constant, φ_{12} increases steadily at the rate $2eV/h$

but instantaneously snaps back by 2π when a PS occurs. Thus, φ_{12} executes an irregular sawtooth which is equivalent, modulo 2π , to a uniform ramp.

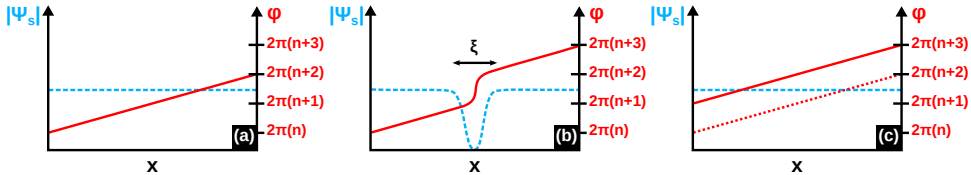


Figure 1.8: **Graphical representation of the PS mechanism.** (a) Gradient of the phase is constant between the two ends. $|\psi_s|$ is uniform over the whole condensate and phase coherence is maintained. Here, the horizontal axis represents the x coordinate for simplification. (b) Superconductivity is lost at some point of the condensate, $|\psi_s|$ drops to zero at this point, allowing the phase to slip by 2π . (c) Phase coherence is re-established together with uniformity of $|\psi_s|$.

1.3.1.2 Quantitative considerations

Let us consider a one-dimensional superconductor, meaning a wire of length L with transverse dimension $d \ll \xi$ so that variations of ψ_s over its cross-section are energetically prohibited. In that case, ψ_s is a function of a single coordinate x running along the wire, as in Figure 1.8. Let us also assume $d \ll \lambda$, so that magnetic energy can be neglected compared to kinetic energy. In order to better visualize the evolution of the complex function $\psi_s(x)$ during the PS process, it is convenient to plot $|\psi_s(x)|e^{i\varphi(x)}$ in polar form in a plane perpendicular to the x axis. Stationary solutions representing the flow of supercurrent at zero voltage have the form^[8],

$$\psi_{s,0}e^{iqx} \quad (1.32)$$

and are represented by helices of pitch $2\pi/q$ and radius $\psi_{s,0}$ as shown on Figure 1.9(a).

Resistive processes in the superconducting state have been addressed in details by Langer and Ambegaokar^[14]. When a voltage exists between the ends of the wire, the relative phase increases at the Josephson rate given by Eq. (1.18). This can be visualized as the phase at one end being steadily "cranked" around the Argand diagram while the other end is held fixed, thus tightening the helix. That is, the presence of the voltage increases q at a rate such that the total phase difference $\varphi_{12} = qL$ along the wire obeys Eq. (1.18).

The uniform solution of Figure 1.9(a) does not exist above a certain critical velocity

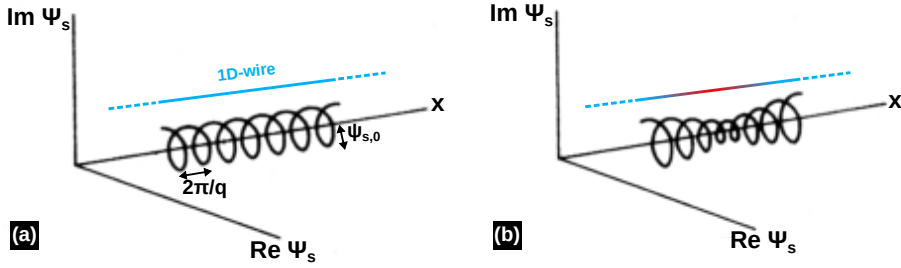


Figure 1.9: **Graphical representation of the complex current-carrying GL wavefunction in one-dimensional superconductors.** (a) Uniform solution, giving an helical wavefunction of pitch $2\pi/q$ and radius $\psi_{s,0}$. (b) Non-uniform solution just before a PS event^[8]: the helix is "compressed" and $|\psi_s| \rightarrow 0$ at some particular point where the occurrence of a PS event is imminent.

of the charge carriers v_c , corresponding to the critical current density J_c . The PS process proposed by Langer and Ambegaokar maintains a steady state with $v_s < v_c$, in the presence of a non-zero voltage, by annihilating turns in the interior of the helix at the same average rate as new ones are being "cranked" in at the exterior. Considering that conservation of current requires $J_s(x) \propto |\psi_s(x)|^2 v_s(x)$ to be constant, we have through Eq. (1.16)

$$|\psi_s(x)|^2 \frac{d\varphi}{dx} = \text{const} \propto I \quad (1.33)$$

and it is clear that if $|\psi_s|$ becomes very small in some region, $\frac{d\varphi}{dx}$ has to be large there. Thus as depicted in Figure 1.9(b) and first emphasized by Little^[15], as the limit $|\psi_s| \rightarrow 0$, it is relatively easy to add or subtract a turn. Thereby we get back to the qualitative picture depicted in Figure 1.8. In other terms, the energy that is supplied at a rate VI is dissipated as heat rather than converted into kinetic energy of supercurrent, which would otherwise soon exceed the condensation energy.

1.3.2 Thermally Activated Phase Slips (TAPS)

Trying to formalize the addition/subtraction of a turn of the helical wavefunction, Langer and Ambegaokar found paths through the function space between two uniform solutions with different number of turns. In short, they took the one with the lowest intermediate free-energy barrier to overcome, namely

$$\Delta F_0 = \frac{8\sqrt{2}}{3} \frac{H_c^2}{8\pi} S\xi \quad (1.34)$$

where S is the cross-sectional area of the conductor. A simple interpretation of this formula comes from considering that at least a length ξ of wire should become normal if a decoupling of the phase between the two wire ends was to be seen [8].

At this point of the story, we have the energy barrier for PS, but in the absence of a current, flipping by $\pm 2\pi$ is equally likely; this gives a fluctuating noise voltage but no DC component. A schematic representation of the periodic energy potential is given in Figure 1.10(a). However, if we consider a driving voltage, the current will build up a steady state value at which the $\Delta\varphi_{12} = +2\pi$ jumps outnumber the $\Delta\varphi_{12} = -2\pi$ ones by an amount of $2eV/h$ per second.

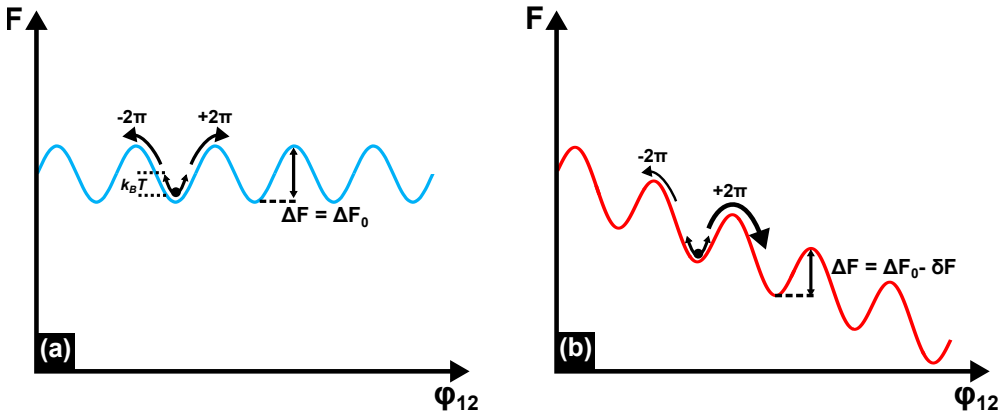


Figure 1.10: **Scheme of the energy landscape of Langer and Ambegaokar.** (a) In the absence of applied voltage, phase slips of $\pm 2\pi$ are equally likely. (b) With a driving voltage, potential turns to the tilted washboard form, thus favouring one type of slippage over the other.

The different slipping rates stem from a difference in the electric work $\int V I dt$ done in the process, thus lowering the energy barrier^[16,17] in view of Eq. (1.18) by an amount

$$\delta F = \frac{h}{2e} I = \Phi_0 J S. \quad (1.35)$$

The symmetry of the energy landscape is then broken, giving rise to a tilted-washboard potential as illustrated in Figure 1.10(b). The final step consists in introducing an attempt frequency Ω so that the mean net PS rate is

$$\dot{\varphi}_{12} = \Omega \left[\exp \left(-\frac{\Delta F_0 - \delta F/2}{k_B T} \right) - \exp \left(-\frac{\Delta F_0 + \delta F/2}{k_B T} \right) \right] \quad (1.36)$$

$$= 2\Omega e^{-\Delta F_0/k_B T} \sinh \left(\frac{\delta F}{2k_B T} \right). \quad (1.37)$$

Now if we substitute Eq. (1.35) into Eq. (1.37) and using Eq. (1.18), we obtain an

expression for the voltage,

$$V = \frac{\hbar\Omega}{e} e^{-\Delta F_0/k_B T} \sinh\left(\frac{hI}{4ek_B T}\right) \quad (1.38)$$

which, in the limit of very small currents⁶ and using Ohm's law, gives the resistance

$$R = \frac{V}{I} = \frac{\pi\hbar^2\Omega}{2e^2k_B T} e^{-\Delta F_0/k_B T}. \quad (1.39)$$

Originally, the question of the value of the prefactor Ω was open, Langer and Ambegaokar taking at first a rather arbitrary value^[14]. A few years later, using time-dependent Ginzburg-Landau (TDGL) theory, McCumber and Halperin proposed^[18] a temperature dependant prefactor of the form

$$\Omega = \frac{L}{\xi} \left(\frac{\Delta F_0}{k_B T}\right)^{1/2} \frac{1}{\tau_{GL}} \quad (1.40)$$

where L is the length of the superconducting wire and $\tau_{GL} = \pi\hbar/8k_B(T_c - T)$ is the characteristic relaxation time in the TDGL theory. The fact that the attempt frequency is proportional to the length of the wire is somewhat expected since *the jump can occur independently at sites all along the wire* whereas L/ξ represents *the number of non-overlapping locations in which the fluctuations might occur*.^[8] The results for the appearance of resistance in a superconducting wire undergoing PS due to thermal fluctuations derived by Langer and Ambegaokar together with the value of the attempt frequency proposed by McCumber and Halperin, are given the name of Langer-Ambegaokar-McCumber-Halperin (LAMH) theory. This provides a framework to describe what are called thermally activated phase slips (TAPS).

1.3.3 Quantum Phase Slips (QPS)

A natural breakdown of the TAPS model comes from the fact that once the barrier ΔF has been sufficiently reduced, tunnelling through, instead of surmounting it, becomes more likely. This is depicted in Figure 1.11. This regime of quantum phase slips (QPS) has been theoretically investigated by Golubev-Zaikin (GZ) who predicted^[19] a temperature dependence of the resistance given by

$$R_{\text{QPS}}(T) = \frac{h\Gamma_{\text{QPS}}}{2eI}, \quad (1.41)$$

where

⁶In the limit of very small I , the hyperbolic sine can be replaced by its argument.

$$\Gamma_{\text{QPS}} = \frac{S_{\text{QPS}}}{\tau_0} \frac{L}{\xi(T)} \exp(-S_{\text{QPS}}) \quad (1.42)$$

is the rate of QPS activation, $\tau_0 \sim h/\Delta$ is the characteristic response time of the superconductor, $S_{\text{QPS}} = A(\frac{R_q}{R_N})(\frac{L}{\xi(T)})$ is the effective action, $R_q = h/4e^2$ is half the quantum of resistance, R_N is the resistance in the normal state, $\xi(T)$ is the coherence length, L is the length of the wire and A is a numerical constant.

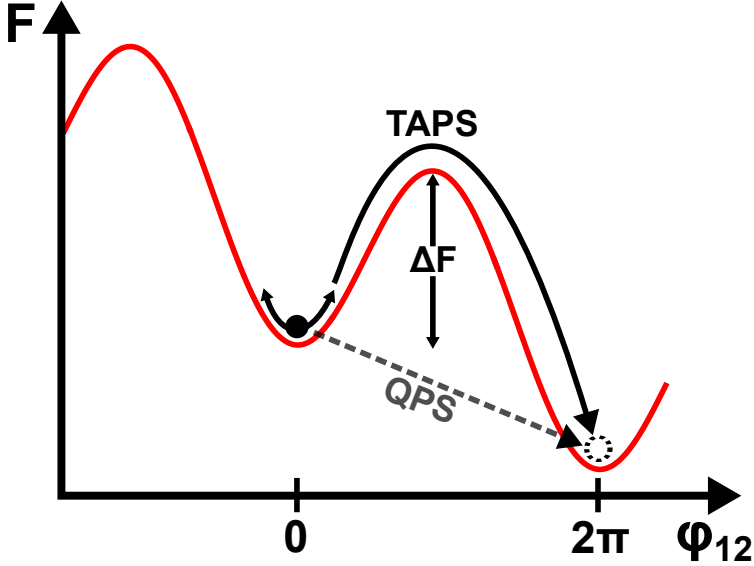


Figure 1.11: **Scheme of thermal and quantum fluctuations assisting the PS mechanism.** Below certain temperature, the free-energy barrier ΔF becomes small enough so that quantum tunnelling, compared to classic thermal crossing, is the predominant mechanism for the system to overcome it.

Chapter 2

Electromigration in metals

2.1 Introduction

This chapter aims at introducing the basic current understanding about atomic migration promoted by an electron wind, a phenomenon known as electromigration (EM). The physics of this phenomenon is presented, starting with the interaction of the electrons with the lattice including static and dynamic perturbations and ending with the estimation of the mass flux resulting from this effect. The key role played by the temperature, grain structure and dimensions, are also explained. Although in early days, the displacement of atoms caused by high electric current densities was identified as a major problem of narrow Al interconnects in integrated circuits^[20–23], this initial negative perception has progressively changed, as the scientific community first understood the physical mechanisms involved in the process and then learnt to master it^[24–26]. At the end of this section we detail our approach to gain some control on this stochastic phenomenon.

2.2 Historical context

Today microelectronic circuits can be counted among the most reliable human inventions ever built. Indeed, the number of transistors in a single-chip processor largely surpasses one billion units^[27] and yet it is expected to work for an extended period of time, say 10 years, without failing. In addition, what is even more challenging, is that the reliability must continue to increase as the complexity increases.

However, in the successful story of integrated circuits, there was initially a major concern. In the late 60's, electronic integrated circuits were often returned for inspection because of failure notices^[27]. Mean time of operation was of the order of weeks and after failure, nothing could be seen, even under a microscope. The shock for the industry was as tremendous as the hope placed in these circuits in the first place. A relatively new research tool introduced around those times allowed to unveil the ultimate cause of failure. The scanning electron microscope (SEM) was able to identify the failure sites as tiny cracks, voids and hillocks in the metallic lines, sometimes only a few nanometers wide and therefore escaping from optical microscopy inspection. It was understood that the origin of these defects was the high current densities applied to the devices. At first, making the interconnect lines wider and thicker helped to solve the problem. This was easy with the millimeter-wide lines of those times, but not so easy today. Since then, EM has not gone away but is now better understood although it continues to be a serious concern as miniaturization of electronic devices progresses. Solving the EM problem came to a high price, only at IBM it was estimated that close to a billion dollars were spent in the effort to solve the EM issue^[27].

2.3 Physics of atomic diffusion under electron wind

2.3.1 Electron-lattice interaction

Electromigration describes the motion of atoms in a metal under the influence of an applied electric field^[28]. This movement results from the momentum transfer between conducting electrons and lattice ions likely to diffuse. In materials with negative carriers (n-type), failures were noted near the cathode whereas in materials with positive charge carriers (p-type) failures were observed near the anode, thus demonstrating the role of the sign of the charge carrier in EM^[27]. This can be easily understood by looking at Figure 2.1.

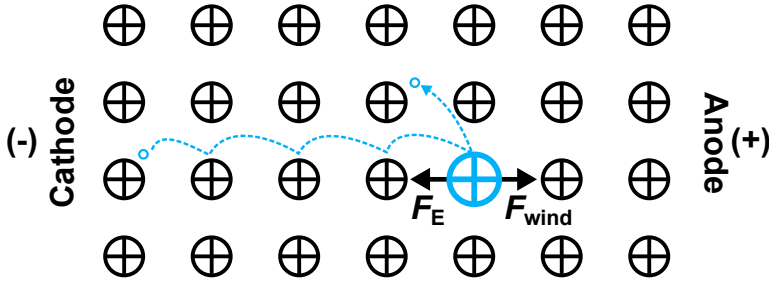


Figure 2.1: **Forces felt by an ion in a metallic lattice subjected to an electric current.** F_E is the force due to the electric field, F_{wind} is the electron wind force. Due to the latter, ions are pushed towards the electrode that has the sign opposite to the one of the carriers.

To understand the mechanisms of momentum transfer, let us briefly review the propagation of electron waves in a crystal. If we make the hypotheses of non-interacting (independent) electrons moving in a perfect crystal characterized by a periodic and static potential, then the problem is reduced to a one-body Schrödinger equation^[29],

$$\left[-\frac{\hbar^2}{2m_e} \nabla^2 + V(\mathbf{r}) \right] \psi_e(\mathbf{r}) = \mathcal{H}_0 \psi_e(\mathbf{r}) = E \psi_e(\mathbf{r}), \quad (2.1)$$

where

$$V(\mathbf{r} + \mathbf{R}) = V(\mathbf{r}) \quad (2.2)$$

with

$$\mathbf{R} = n_1 \mathbf{a}_1 + n_2 \mathbf{a}_2 + n_3 \mathbf{a}_3, \quad (2.3)$$

\mathbf{a}_1 , \mathbf{a}_2 , \mathbf{a}_3 , primitive lattice vectors and n_1 , n_2 , n_3 , integers. Since $V(\mathbf{r})$ is periodic, it can be expressed as a Fourier series

$$V(\mathbf{r}) = \sum_{\mathbf{G}} V_{\mathbf{G}} e^{i\mathbf{G} \cdot \mathbf{r}} \quad (2.4)$$

with the condition $e^{i\mathbf{G}\cdot\mathbf{R}} = 1$ implying $\mathbf{G} \cdot \mathbf{R} = n \cdot 2\pi$ and thus

$$\mathbf{G} = m_1\mathbf{b}_1 + m_2\mathbf{b}_2 + m_3\mathbf{b}_3 \quad (2.5)$$

where $\mathbf{b}_1, \mathbf{b}_2, \mathbf{b}_3$ are reciprocal lattice vectors satisfying $\mathbf{a}_i \cdot \mathbf{b}_j = 2\pi\delta_{ij}$ and m_1, m_2, m_3 are integers. The Schrödinger equation being linear and the potential being periodic, the wave function could also be expressed as a finite Fourier series in terms of reciprocal space vectors \mathbf{k} compatible with Born-von Karman periodic boundary conditions,

$$\psi_e(\mathbf{r}) = \sum_{\mathbf{k}} c_{\mathbf{k}} e^{i\mathbf{k}\cdot\mathbf{r}} \equiv \sum_{\mathbf{k}} \psi_{\mathbf{k}}(\mathbf{r}). \quad (2.6)$$

The time-independent Schrödinger equation (2.1) can then be rewritten by using Eq. (2.6) and Eq. (2.4). This leads to a rearranged expression for the wave function of the form^[29],

$$\psi_k(\mathbf{r}) = u_k(\mathbf{r}) e^{i\mathbf{k}\cdot\mathbf{r}}. \quad (2.7)$$

This wave, product of a plane wave and a periodic function $u_k(\mathbf{r}) = u_k(\mathbf{r} + \mathbf{R})$ having the periodicity of the potential, is called a Bloch wave, a type of wave function for a particle (here an electron) in a periodically repeating environment (here the crystalline lattice)^[29].

The Bloch waves are stationary solutions of the Schrödinger equation and describe an unperturbed propagation of electron waves. Therefore, in this scenario of a perfect lattice, there is no resistance. Electrons move about in a periodic potential with no other interaction with the metallic ions. In other words, a perfect crystal is a superconductor and no dissipation is expected. Unfortunately, real crystals depart from this ideal picture, as we will describe in the next section.

2.3.2 Static and dynamic perturbations

If we introduce a perturbation W in the lattice such that

$$\hat{\mathcal{H}} = \hat{\mathcal{H}}_0 + \hat{W} \quad (2.8)$$

where $\hat{\mathcal{H}}_0$ is the Hamiltonian of the unperturbed ideal crystal (see Eq. (2.1)), then electron scattering is indeed allowed and the probability to change from the initial state k to the final state k' is given by the Fermi's golden rule,

$$W_{kk'} \propto | \langle k' | W | k \rangle |^2. \quad (2.9)$$

This situation is depicted in Figure 2.2(a). Static perturbations are described by a W which is time independent and lead to elastic scattering while dynamic perturbations

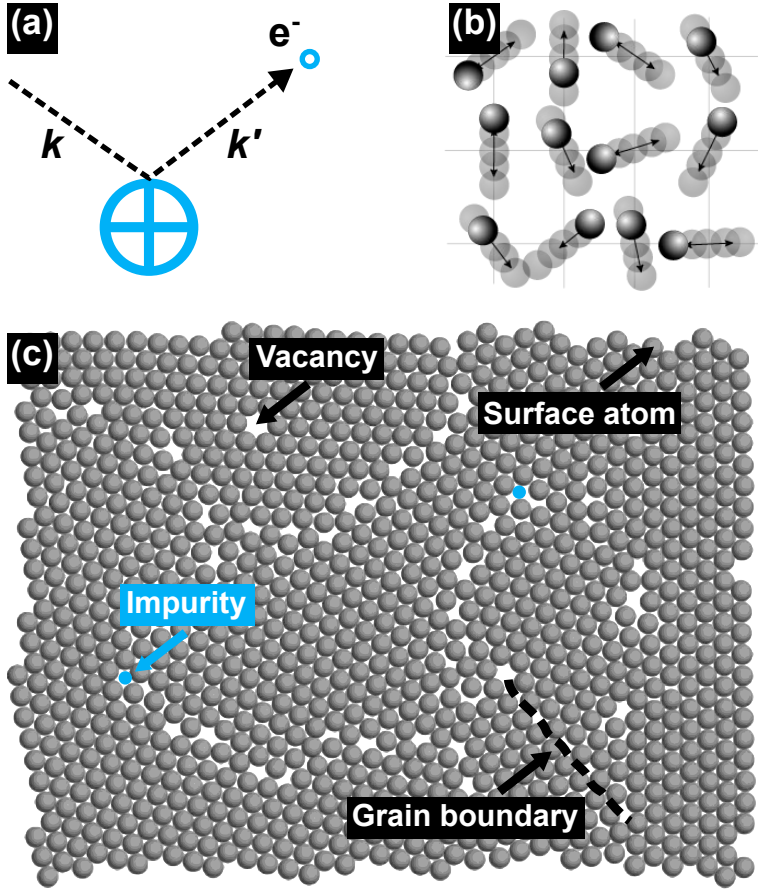


Figure 2.2: **Perturbations allowing scattering of electrons in a crystalline lattice.** (a) Scheme of an electron being scattered from an initial state k to a final state k' via an interaction with an ion of the lattice. (b) Classical picture of thermally excited ions vibrating around their equilibrium positions in a lattice. (c) Portion of crystalline lattice exhibiting defects: atom vacancies, interstitial impurities and grain boundaries.

correspond to a time dependent W and generate inelastic scattering^[30].

Dynamic perturbations are due to temperature. Indeed at any temperature above the absolute zero, atomic vibrations occur. These vibrations put an atom out of its perfect position about 10^{13} times each second (Debye frequency) and distort the otherwise perfectly periodic potential, causing electron scattering^[31]. A sketch of collective excitations (phonons) of atoms in a lattice is shown in Figure 2.2(b). This sort of perturbations are responsible for electric resistance at room temperatures in most metals. Since electromigration is a thermally activated process, they play an important role in the attempt frequency for atoms to diffuse, but the energy barrier that the atoms have to overcome is even more important. This latter is ruled by static

perturbations.

A perfect lattice cannot exist above absolute zero due to missing atoms (vacancies), other interstitial or substitutional atoms (impurities), boundaries between crystals of different orientation (grain boundaries), lower coordination of surface atoms, and regions of discontinuity in the crystalline lattice (dislocations). Some of these defects are illustrated in Figure 2.2(c). In this list, vacancies and grain boundaries are particularly important to allow ions to move from their fixed position in the lattice. This process, called diffusion or migration, is depicted in Figure 2.3.

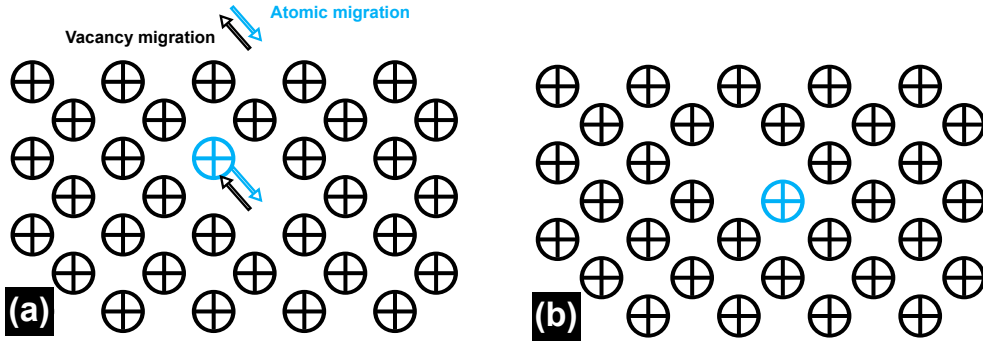


Figure 2.3: **Atomic migration in a crystalline lattice** (a) Depending on the view-point, it is either the atom that diffuses or the vacancy. (b) After migration, atom and vacancy have exchanged their positions.

2.3.3 Mass flux

Unidirectional atomic diffusion leads to flux of mass. Mass flux is the result of the combination of two phenomena: thermal diffusion of ions, which can be considered isotropic at the level of the entire lattice, and directional drift due to the electron wind, which is superimposed to diffusion and defines a favored direction.

Let us imagine an average electron accelerated by an electric field and colliding purely elastically with an atom. In this situation, the energy acquired by the atom is proportionnal to the product of the field strength by the component of the electron mean free path l in the direction of the field. The mean free path for an electron in a metal at room temperature is on the order of a few hundreds of nanometers at most^[32]. So if we take a plausible value of 10^4 Vm^{-1} for the electric field and a mean free path of $1 \mu\text{m}$, the electron will gain only 10^{-4} eV , which is not much in comparison to thermal energy of a metal atom averaging at about $k_B T_{\text{room}} \sim 3.10^{-2} \text{ eV}$. Net motion of the atom in the direction of the electron flow can be understood if we consider the fact that momentum exchanges happen many times per second.

It is easy to see that both the direct electrostatic force on the ion caused by the

applied electric field E and the electron wind force, are proportional to E . Thus we can propose that the customary total force^[33,34] writes as

$$F = F_{wind} - qE = q^*E \quad (2.10)$$

where q^* is called the effective charge. Using Ohm's law $E = \rho J$ and taking $q^* = Z^*e$, we have

$$F = Z^*e\rho J \quad (2.11)$$

where Z^* is called the effective valence while it actually represents the magnitude and direction of the momentum exchange^[32]. On average it can be considered that electrons are particles moving in a overdamped medium (damping caused by the collisions), and therefore the force is not proportional to the acceleration but rather to the velocity. We then define the mobility μ as the ratio of the drift velocity v_d and the force F that it is originating from,

$$\mu = \frac{v_d}{F} \quad (2.12)$$

so that we can express the drift velocity of atoms due to the EM force v_{EM} as

$$v_{EM} = \mu Z^*e\rho J. \quad (2.13)$$

Since we are also dealing with a thermal diffusive process, we use Einstein diffusion relation $D = \mu k_B T$ and obtain,

$$v_{EM} = D \frac{Z^*e\rho J}{k_B T}. \quad (2.14)$$

Therefore, the vacancy flux due to EM is given by

$$\Theta_v = -C v_{EM} = -CD \frac{Z^*e\rho J}{k_B T} \quad (2.15)$$

where C is the concentration of vacancies, which is quite small in a single crystal but may be substantial in polycrystalline materials.

Mass flux related to thermal diffusion and EM-induced drift velocity are not sufficient to cause failure in a conducting line (e.g. voids or extrusions). Indeed, to create a void, for instance, less mass has to enter a certain region than the amount of mass exiting it. As depicted in Figure 2.4, if less mass is leaving than arriving, extrusions develop. These particular regions are said to represent point of flux divergence^[32]. Flux divergences are made possible by the fact that mass transport does not depend only on the EM driving force of Eq. (2.11), but also on the sum of all the chemical potentials that may be acting on the diffusing metallic atoms. The most important of

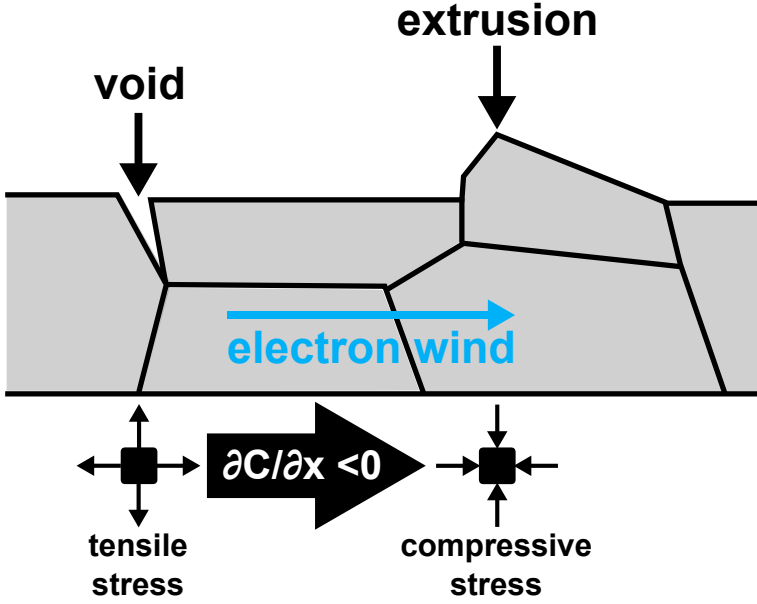


Figure 2.4: **Flux divergences in a granular metallic lattice.** Voids and extrusions form as a consequence of concentration/stress gradients.

these are the stress gradient and the concentration gradient, which are not independent quantities^[32]. Indeed, increasing tensile stress will increase vacancy concentration in thermal equilibrium while the opposite happens for a compressive stress, as it is indicated in Figure 2.4. Therefore it is simpler to invoke only one of these gradients and, if thermal equilibrium is achieved, the mass transport can be expressed as,

$$\Theta_m = D \left(\frac{\partial C}{\partial x} - C \frac{Z^* e \rho J}{k_B T} \right) \quad (2.16)$$

with time dependent behavior given by the continuity equation,

$$\frac{\partial C}{\partial t} = \frac{\partial \Theta_m}{\partial x}. \quad (2.17)$$

The most common condition for visualizing flux divergences is the case of contact points, occurring at the interface between two different materials. This situation is shown in Figure 2.5 for aluminum contacts on a silicon substrate. In this particular case, since diffusion of Al from Si is negligible and vice versa, EM will accumulate aluminum atoms at the contact point, or on the contrary, drive them away. Now that the process of mass transport due to EM has been presented, let us review the key factors that are involved in this process.

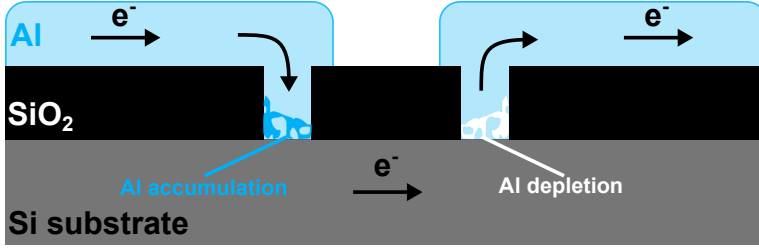


Figure 2.5: **Flux divergences at the contact points of two materials.** Here, aluminum accumulates/depletes at the interface with silicon due to negligible diffusion of both materials in one another.

2.3.4 Activation factors

2.3.4.1 Effect of temperature

From Eq. (2.15) EM-induced mass flow is seen to be directly proportional to the diffusion constant D . Diffusion is a thermally activated process characterized by the Arrhenius relation,

$$D = D_0 e^{-\frac{U}{k_B T}}. \quad (2.18)$$

This equation shows that EM is very sensitive to temperature. This fact is illustrated in Figure 2.6(a) for different diffusion mechanisms.

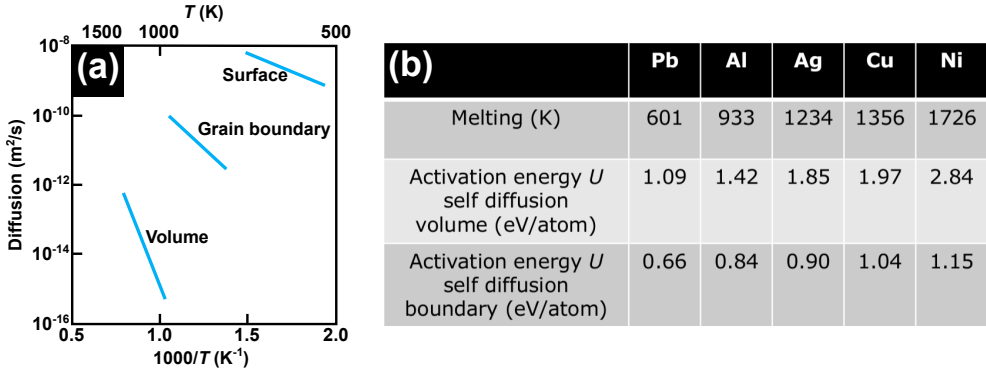


Figure 2.6: **Activation energy considerations for self-diffusion.** (a) Self-diffusion coefficients for silver (Ag) depend on the diffusion path. Adapted from^[35] (b) Activation energy for self-diffusion in different metals.

Another important effect is mass flux caused by temperature gradients. Indeed, the generation of a void along a conducting strip will give rise to current crowding and substantial Joule heating. The consequent localized hot spot will, in turn, generate a temperature profile decaying within a few microns to the temperature of the bath. Thus, temperature gradients as high as 10^4 to 10^7 °C/cm can develop^[36]. The tem-

perature gradients produce flux divergences comparable to divergences at contacts or at microstructural features and need to be included in Eq. (2.17) as,

$$\frac{\partial C}{\partial t} = \frac{\partial \Theta_m}{\partial x} \Big|_T + \frac{\partial \Theta_m}{\partial T} \Big|_x \frac{\partial T}{\partial x}. \quad (2.19)$$

Under the condition that $\frac{\partial T}{\partial x} \gg \frac{\partial \Theta_m}{\partial x}$, the second term of the right hand side dominates, and EM failure will take place at the points of maximum temperature gradient.

In 1969, James Black of Motorola, Inc. proposed an empirical law for the median time to failure of an ensemble of identical devices^[23],

$$\tau = \frac{wt}{A} J^{-2} e^{\frac{U}{k_B T}}. \quad (2.20)$$

where U is the activation energy or barrier needed to be overcome by an atom in the material to start diffusing, T is the local temperature, J is the current density, A is a constant depending of the material, w and t correspond to the width and thickness of the wire, respectively. This law holds for nucleation dominated¹ failures and not for growth dominated² failures.

2.3.4.2 Effect of grain structure

The drift velocity ν_{EM} is a function of the diffusion pathway and its temperature dependence is characterized by the activation energy of the predominant diffusion mechanism^[32]. In general, the diffusion coefficient is greater through less restrictive structural regions^[35]. For instance, the diffusion coefficient along a surface is greater than that along a grain boundary, while grain boundary diffusive transport is more rapid than in the lattice as indicated in Figure 2.6.

As a rule of thumb, the grain boundary self-diffusion activation energy is roughly half that of the lattice whereas surface diffusion activation energies are about 1/3 of that in the lattice. The activation energy for diffusion along other interfaces is quite dependent on the nature of the interface and can be either higher or lower than that in the grain boundary^[32]. For example, in aluminum, depending of the oxide layer covering the surface, EM can be triggered at the surface or at an internal grain boundary.

2.3.4.3 Size effects

The cross-section matters. According to Eq. (2.20), it is clear that EM is sensitive to dimensions. This is actually the reason why EM is not a phenomenon observed in

¹This means that the characteristic time depends mainly on the nucleation.

²On the contrary, here it is the time for growth that dominates.

daily life. Indeed, in household electric cables, the melting point is reached at current densities as low as 10^4 A.cm^{-2} . This is far too low to cause EM, which necessitates current densities between 10^6 and 10^8 A.cm^{-2} . However, at very low dimensions, at the scale of the μm and nm , such current densities can be achieved without reaching the melting point. In order to understand this, we have to consider two factors.

Firstly, it must be considered that heat generation P_{in} will be less when cross-section is reduced. Indeed, we can do the following estimation based on Joule's and Pouillet's laws,

$$P_{in} \approx \frac{\rho L}{S} (SJ)^2 \sim SJ^2, \quad (2.21)$$

where R is the resistance of the wire, J the current density passing through, ρ its resistivity, L its length, S its cross-section.

The second factor lies in the ratio between heat generation P_{in} and heat removal P_{out} , known as the Stekly parameter α , which writes as^[37]

$$\alpha = \frac{\rho J^2 r}{\Upsilon(T - T_B)}, \quad (2.22)$$

where Υ is the heat transfer coefficient, T_B the bath temperature and $r = S/P$ with P the perimeter. One can directly see that if S is reduced, then r and thus α are also reduced and so is P_{in}/P_{out} . In other words, when sample's size shrinks, the surface/volume ratio increases and so does the heat removal. Therefore, self-heating is reduced and it is possible to explore higher current densities without melting the material.

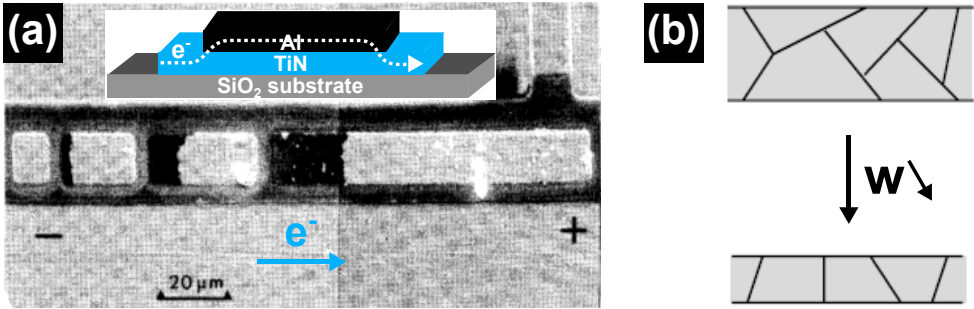


Figure 2.7: **Influence of dimensions, length and width, on EM.** (a) Original figure from Blech^[38]. Direction of electron wind and cross-section of electron path have been added for completeness. When electrical currents are passed through the sample, the aluminum stripe carries most of the current since its sheet resistance ($0.07\Omega/\square$) is much lower than that of the TiN ($10\Omega/\square$). When the Al island is long enough, material is displaced but when it is too short EM does not occur. (b) When the width is reduced, grain boundaries tends not to be in the direction of the current flow, impeding EM process.

The length matters. In 1976 Ilan Blech at Bell Labs studied the behavior of Al islands of different lengths deposited on top of a material with much higher resistivity and the whole submitted to high current densities^[38]. When current was applied through these samples, the upstream side of the stripes moved in the direction of electron flow and the downstream edge erodes away. If the stripe was long enough, extrusions formed on the downstream edge, but if the stripe was short enough, EM essentially stopped. Original figure of Blech is reproduced as Figure 2.7(a). He discovered that there is a critical product of the current density and the length of the stripe, below which EM ceases, that is

$$JL_{Blech} \leq 3000. \quad (2.23)$$

Below this limit, EM is compensated by stress gradient. Above it, ionic drift caused by electron scattering outclasses gradient of stress.

The width matters. It is not surprising that EM failure is inversely proportional to the grain size of the films: the more grain boundaries present, the more atoms can be transported along them, and the shorter the failure time. As line widths become smaller, the conductor lines become comparable in width to the grain size and a "bamboo" like structure appears, providing no continuous grain boundary pathway in the direction of the current flow^[28]. This situation, occurring when width w diminishes, is depicted in Figure 2.7(b). Narrow lines at the same current density become substantially more reliable than wider lines, as long as the grain size is uniform.

2.3.5 Improving the resistance to electromigration

Historically, one of the first implemented solution was to alloy Al with Cu^[27], initially up to 4%. This has changed due to processing considerations and today generally 0.5% Cu is still alloyed with Al. An alternative, although unpractical, approach consist in getting rid of the grain structure by using single crystals^[24] or to shunt junctions with refractory materials that can stand very high temperatures and current densities^[38]. Encapsulated wires or simply resorting to AC currents are also solutions that can be considered. The problem of EM continues today as Moore's law progresses to higher device densities and three dimensional integration. While electronic industry is doing its best to avoid EM, it is sometimes interesting to use it to one's own advantage.

2.4 Controlling atomic migration: state of the art

Examples illustrating the benefits of controlling the EM process include the creation of few nanometer gaps between two Au pads^[39–44] with the aim to electrically address

single molecules^[45–47], the electrical sculpting of nanowires to obtain atomic point contacts^[48–50], metal purification and separation of atoms in binary alloys due to the mass selectivity of the process^[51], current-induced crystallization^[52], and cleaning of graphene layers^[53]. Irrespective of the aimed goal, most of the reports refer to very similar kind of sample layouts and EM control algorithms. We briefly discuss these approaches in the following subsections.

2.4.1 Layout of the structures

EM depends on current density, as it can be seen from Eq. (2.15) or from Black law (Eq. (2.20)). The idea is to introduce a constriction where current crowding will greatly favor EM and ensure that it will be likely triggered in its vicinity. This is why most of the layouts incorporate geometrically constricted portions like bow-ties, Dayem bridges or related^[40,41,48,49,54,55]. An overview of these designs is shown in Figure 2.8.

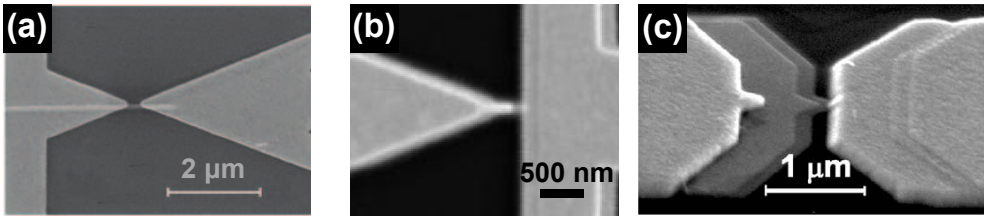


Figure 2.8: **Constricted layouts to favor EM.** (a) Bow-tie geometry to form gold nanogaps used by Esen *et al.*^[40]. (b) Hybrid bow-tie/Dayem bridge geometry to fabricate point contacts used by Campbell *et al.*^[49]. (c) Dayem bridge structure with terraces formed by shadow evaporation to study the role of Joule heating in the formation by EM of gold nanogaps used by Trouwborst *et al.*^[43].

2.4.2 Control loop

There is a variety of different approaches that have been used in the scientific community to control the EM process. Their differences put aside, they are all based on the same observation: self-control of EM process by voltage bias is not easy or simply impractical. To master it, a more or less complex electronic feedback is needed.

2.4.2.1 Limitations of voltage-driven self-controlled EM

Let us consider a sample with a constriction which is fed by a variable voltage source. We know that current crowding will rise the temperature, and thus the resistance, due to Joule heating. Considering their mutual influence on EM as mentioned previously in this chapter, it is not difficult to imagine that if the bias voltage is increased, current

will be, at a certain point, high enough to generate voids. These voids will increase the resistance of the junction which in turn will produce a decrease of the dissipated power $P = V^2/R$.

Though this logic is correct but somewhat misleading. Let us do the math more carefully based on the circuit shown in Figure 2.9(b). The power dissipated at the junction P_j is

$$P_j = R_j I^2 = V_0 I - (R_L + R_W) I^2. \quad (2.24)$$

The current can be expressed as

$$I = \frac{V_0}{R_L + R_W + R_j}, \quad (2.25)$$

which allows to transform Eq. (2.24) as follows

$$P_j = \frac{V_0^2 R_j}{(R_L + R_W + R_j)^2}. \quad (2.26)$$

For a constant bias voltage V_0 sufficient to trigger EM and induce voids formation, an increase of R_j will be observed. Then if $R_L + R_W \gg R_j$, it is clear from Eq. (2.26) that the power dissipated in the junction would first increase before eventually decrease when R_j will be sufficiently high. The same conclusion can be reached from Eq. (2.24) by deducing from Eq. (2.25) that if $R_L + R_W \gg R_j$, current would remain mostly constant if R_j starts increasing and therefore P_j would then increase at first. Actually, this process will lead to a positive gain feedback loop as schematically shown in Figure 2.9(a) and essentially will finish with sudden increase of resistance and damage as it is illustrated in Figure 2.9(c).

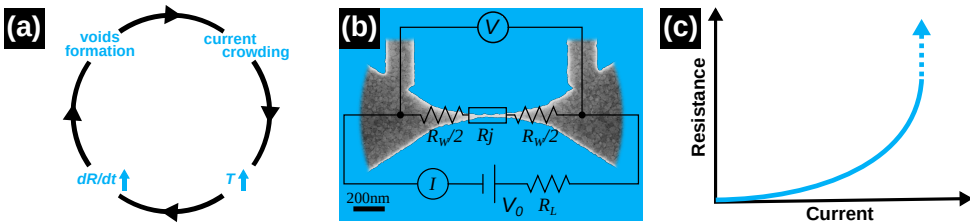


Figure 2.9: **Uncontrolled EM.** (a) Schematic feedback loop of EM: current crowding induces heat and increase of resistance eventually resulting in voids formation, which reinforces current crowding. (b) SEM image of a nanoconstriction on which the equivalent circuit of measure is superimposed: V_0 is the bias voltage, I is the resulting current, V is the voltage drop across the constriction, R_j , R_W and R_L are respectively the resistances of the junction, the wires, and the leads. (c) Typical behavior of EM: resistance of the junction drastically increases and causes failure of the device when reaching a sufficiently high value of current or voltage.

A built-in way to achieve self-control could have been to satisfy the condition $R_L + R_W \rightarrow 0$, keeping P_J essentially constant during EM as it can be seen from Eq. (2.26). Unfortunately, it appears to be extremely difficult to reach experimentally.

2.4.2.2 Electronic control loop

As self-control of EM is nearly impossible to obtain experimentally, an easier solution was widely developed and used by the community: an electronic feedback loop mainly allowing the bias voltage to be quickly adjusted under resistance changes. While several different approaches have been proposed, a scheme common to all of them emerges. The idea is to choose a process variable p and keep it constant in order to brake the EM runaway process, as it is schematized by the modified EM loop in Figure 2.10(a). In the literature, several process variables have been considered to control and monitor the electromigration process in different devices, such as dR/dt ^[56], $(dR/dt)/R$ ^[49,57], $d(1/R)/dt$ ^[40,41] or P_R ^[58], with P_R the dissipated power in the device and R its resistance.

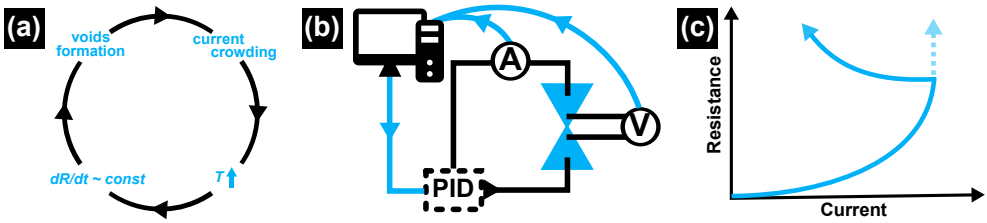


Figure 2.10: **Controlled EM.** (a) The positive feedback loop of EM is stabilized by keeping the control variable constant, in this case dR/dt . (b) Scheme describing most of the designs used so far: a computer is controlling the voltage applied based on the knowledge of voltage and current of the junction. Sometimes, an external PID controller is included to increase the reaction speed. (c) When EM is properly controlled, the resistance increases smoothly while current is being reduced, following a line of constant power and avoiding failures.

Once the process variable is chosen, the algorithm is pretty simple: constantly probe current and voltage across the junction and let the software decide, based on the evolution of the chosen variable, whether or not it should adapt the voltage. This is summarized in Figure 2.10(b). Sometimes, an external proportional-integral-derivative (PID) controller^[49] or a field programmable gate array (FPGA)^[59] are used to increase the reaction speed. All these improvements make possible a relatively good control of EM, and allow the users to induce a smooth increase of resistance while current is being reduced. Failures can then be avoided, or at least their number much reduced. Figure 2.10(c) summarizes the EM behavior resulting from the above cited improvements.

2.5 Controlling atomic migration: the software

Confronted to limitations and drawbacks of the existing softwares, a homemade software was developed and gradually improved over the years by teams at KULeuven and ULiège. The most accomplished version was the object of a joint publication^[60] on which this section is largely based.

2.5.1 Choice of the process variable

Although all the considered process variables are somehow related to the speed of electromigration, a solid motivation for the particular selected variable is lacking in most references. In order to properly identify the suitable process variable, which permits to gain control over the EM process, it is important to first understand the consequences of EM on the properties of the system. In our case, scanning electron microscopy images reveal a progressive reduction of the cross-section during the EM process. The consequent change of geometry affects a region, that we will call a junction, of length L and resistivity ρ . Both the parameters are assumed constant throughout the process, while the cross-section S can vary. As we have seen, EM of this region is the result of an outgoing mass flux and under the aforementioned assumptions, this mass flux Θ_m is proportional to the change of the cross-sectional area S divided by the total cross-section, $\Theta_m \propto (dS/dt)/S = \dot{S}/S$. Since the conductance of the junction is $G_J = S/\rho L$, we obtain $\Theta_m(t) \propto -\dot{G}_J/G_J = \dot{R}_J/R_J$. Based on these considerations, we take $-\dot{G}_J/G_J$ as a measure for the EM speed and adopt it as the process variable to monitor and control the time evolution of EM^[60]. Let us note that the proposed software has the ability to electromigrate different devices using a broad range of process variables, including $-\dot{G}_T$, that implies a crude assumption of the whole device as a junction. Although a solid justification of the latter process variable cannot be made, it is much simpler to handle since no prior knowledge of the exact shape of the junction and its contribution to the total resistance is needed. Both quantities do not have the same time dependence and they are not linked by a linear relation, however a one to one correspondence exists between them^[60], which explains why $-\dot{G}_T$ could be successfully used to roughly control the EM speed.

2.5.2 Pure software-based feedback loop

Most electromigration procedures in the literature follow the general idea of increasing the applied voltage until a threshold value of the selected process variable is obtained. Once this value is reached, the applied voltage is strongly reduced to prevent uncontrolled EM^[40,41,49]. This sequence is repeated until the desired nanoconstriction or nanogap is realized. The obvious advantages of this algorithm are simplicity and min-

imal needs for computer calculation power. Nevertheless, this procedure has several drawbacks. First, it lacks control over the process since the dissipated power, which defines the speed of electromigration, may vary strongly. This low level of speed control implies an irreproducible EM process since the final geometry of a junction depends on the EM rate^[60]. Second, the downtime (time during which no substantial EM happens) is long. Finally, it is required to gradually increase the integration time of the process variable evaluation, since resistance fluctuations become higher with EM (cf. Figure 1c in Ref. 60). This reduces the reaction speed, which is essential to deal with sudden resistance jumps. As a result, commonly used EM procedures demand the continuous attention of an operator correcting parameters during the whole EM process. Nevertheless, large fluctuations in the speed of electromigration will still be present. In order to evade those limitations, we proposed to replace the aforementioned feedback algorithm by a combination of a conventional software-based PID controller, defining the average change of the process variable, with a non-linear algorithm that reacts to sudden jumps in the process variable. The flow chart of the proposed algorithm is given in Figure 2.11.

The right loop (blue) is based on a conventional PID cycle. In terms of PID controller theory, the applied voltage bias is the control variable and the process variable (denoted by p) should be directly related to the electromigration speed, such as $-\dot{G}_J/G_J$ or $-\dot{G}_T$ ^[61]. As in a conventional PID controller, the error between the setpoint and the measured process variable, $e(t) = p - p_{setp}$, is continuously monitored. The PID algorithm is based on proportional, integral, and derivative terms of $e(t)$ that are incorporated in the function $f_{PID}(e(t))$ with corresponding coefficients, which should be adjusted for different devices, materials, and environmental conditions. As discussed in Ref. 60, the EM process is critically dependent on the temperature of the constriction, which is directly related to the dissipated power. A sudden change of resistance could result in an increased power dissipation and destruction of the junction. To deal with this positive feedback, it is important to react promptly to sudden changes of the sample resistance. PID controllers inherently do not work well with non-linear system responses and are too slow to efficiently deal with these. In order to resolve this issue, a non-linear exponential response scheme was added and is represented by the left loop (red) in the flow chart in Figure 2.11. For every control cycle during which the condition $e(t) > k \cdot \epsilon(t)$ is satisfied, the reaction amplitude ($f_{nl} < 0$) is increased until the increase in the process variable is neutralized. Here, $\epsilon(t)$ is the noise RMS and k is a numerical constant. The threshold should be defined such that the algorithm does not react on noise. The reaction amplitude has the following form,

$$f_{nl} = -\delta V_{0\downarrow} \cdot a^N, \quad (2.27)$$

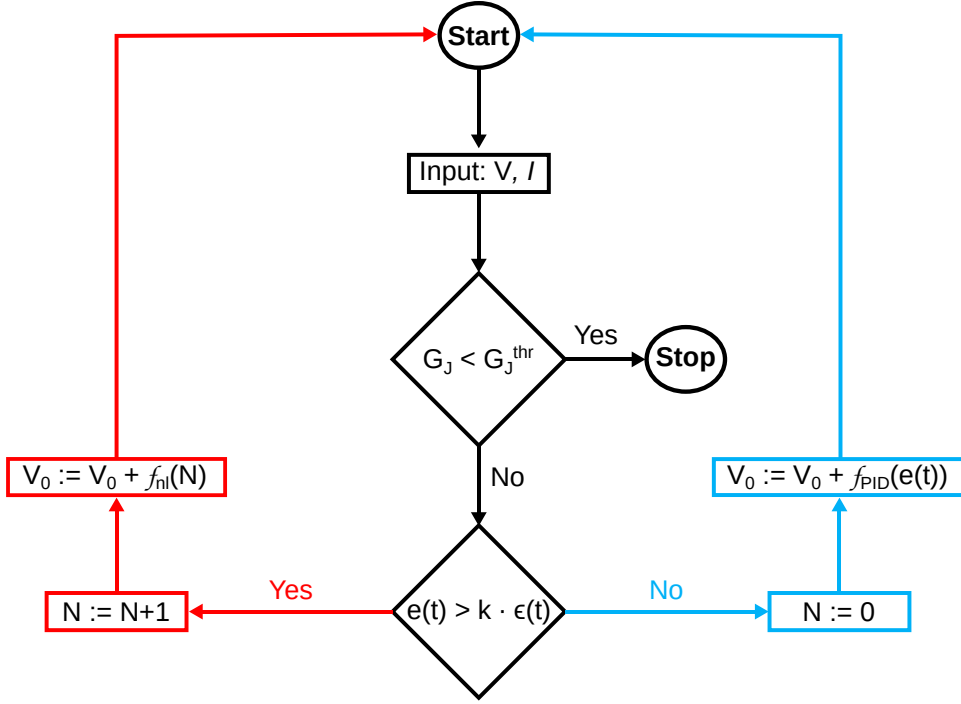


Figure 2.11: **Flow chart of the algorithm to control the EM process with control variable V and process variable p .** The applied bias V_0 is adjusted to keep p as close as possible to the setpoint value p_{setp} minimizing the error $e(t) = p - p_{setp}$. f_{PID} is a response function of the PID controller, whereas f_{nl} is a non-linear algorithm response. $\epsilon(t)$ is the RMS noise value, k is a numerical constant, and N is a counter variable. The algorithm terminates if the conductance of the junction, G_J , reaches the pre-set threshold value G_J^{thr} .

where $\delta V_{0\downarrow}$ and a are constants, while N is the loop index counter. The exponential dependence on N is added to be able to stop positive feedback of the EM process and to reduce the reaction amplitude on insignificant threshold crossings. The values of these parameters are somewhat arbitrary and needs some empirical adjustments

The control cycles terminate once a certain threshold value of the conductance, G_J^{thr} , is achieved. Its value is directly related to the final cross-section of the junction. Due to the high degree of control, the user can accurately estimate the time needed to reach this threshold. The developed protocol allows us to reproducibly change the conductance of a junction and even attain the quantum conductance regime^[60]. In addition, the speed of electromigration can be controlled and switched to different values during the same EM process^[60].

Chapter 3

Experimental techniques

3.1 Introduction

In this chapter, we focus on the experimental aspects (equipments, methods, and procedures) associated to this work. The first part concerns sample fabrication using an electron beam lithography (EBL) system, model Pioneer II commercialized by Raith GmbH and available in the group of Experimental Physics of Nanostructured Materials (EPNM, ULiège, Belgium). The second part will succinctly introduce the cryogenic systems, Oxford continuous flow ^4He cryostat and Oxford ^3He refrigerator from Nanoscale Superconductivity and Magnetism group (NSM, KULeuven, Belgium) and Montana closed-cycle cryostation from our group (EPNM). A fourth system, Oxford ^3He refrigerator from group of Prof. F. Tafuri at University of Naples (Italy), was used to confirm previous results in a cryostat with different noise filtering. As the cooling system is mostly the same as the one at KULeuven, only its filtering systems are presented. The third and final part is devoted to sample installation procedures needed in order to avoid electrical discharges.

3.2 Sample fabrication and observation

Samples used in this work were principally made of two conventional superconductors, aluminum (Al) and niobium (Nb), and two high- T_c superconductors, $\text{YBa}_2\text{Cu}_3\text{O}_{7-d}$ (YBCO) and $\text{La}_{2-x}\text{Ce}_x\text{CuO}_4$ (Lanthanum cerium copper oxide (LCCO)). They were patterned as nanoscaled transport bridges with a central constricted part especially imagined to favor electromigration in its close vicinity^[40,43,49]. Examples of constrictions made of each of the pre-cited material can be found in Figure 3.1. Note that differences in layout and dimensions are present due to material dependent fabrication constraints. Only main steps of sample fabrication processes are presented here, specific technical details (substrate, pressure of deposition,...) are presented along with the corresponding results in the following chapters. As they have been widely involved in sample elaboration, the technologies of electron-beam imaging and lithography are addressed from the viewpoint of the EBL platform at the University of Liège.

3.2.1 Raith PIONEER Two electron microscope

Electron microscopy has been known since the 30's^[62] and its basic principles can be considered as textbook knowledge^[63]. We thus limit this section to the brief description of the Pioneer Two platform, consisting of a dedicated EBL system with capabilities for inspection as a SEM. A home-made third mode, allowing to do observations while performing in situ electrical transport measurements, has been developed and is therefore presented in details.

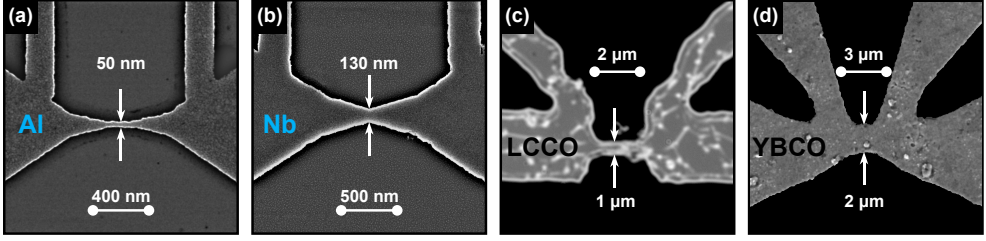


Figure 3.1: **Overview of the investigated samples.** Scanning electron microscopy images of each type of nanojunctions used in this work, respectively made of (a) Al, (b) Nb, (c) LCCO, and (d) YBCO.

3.2.1.1 Scanning Electron Microscopy

An overview of our SEM is given in Figure 3.2(a). It is equipped with a secondary electrons (SE) detector that allows us to have volume visual informations about our samples with a resolution up to few tens of nanometers. This detector resolution is mostly defined by secondary electrons of type two (SE-II), produced where the electron beam comes out of the material^[63]. Better resolution, via elimination of most of the secondary electrons of type two but also of those coming from scattering on the walls of the chamber (said to be of type three, SE-III), can be achieved using another detector installed in close proximity of the objective lens (in lens). This detector's response is dominated by electrons coming directly from the impact site of the beam on the material, the secondary electrons of type one (SE-I)^[63]. The resulting images include information closer to the surface of the sample and possess a resolution that can be pushed to less than five nanometers.

As it can be seen from Figure 3.2(b), there is no load-lock to insert the sample which limits the accessible vacuum level to the range of 10^{-7} mbar. Nevertheless, we profited from this drawback to develop a cutting edge technique of sample visualization while performing transport measurement. The EBL apparatus is installed in an overpressured clean room with stabilized temperature ($\pm 0.1^\circ$), controlled humidity ($<60\%$) and reduced particles contamination thanks to high efficiency particulate air (HEPA) filters.

Figure 3.2(c) shows a zoom in on the sample installation platform. It is provided with two high precision screws which, in combination with laser interferometers, allow the user to set the position of the stage with an impressive accuracy of 2 nm. Further zooming in on the sample holder (Figure 3.2(d)) permits us to see its attributes: a sample area of $2 \times 3 \text{ cm}^2$, two metallic spring clips ensuring charge evacuation and thus good electric contact and a Faraday cup allowing to calibrate the electron beam current.

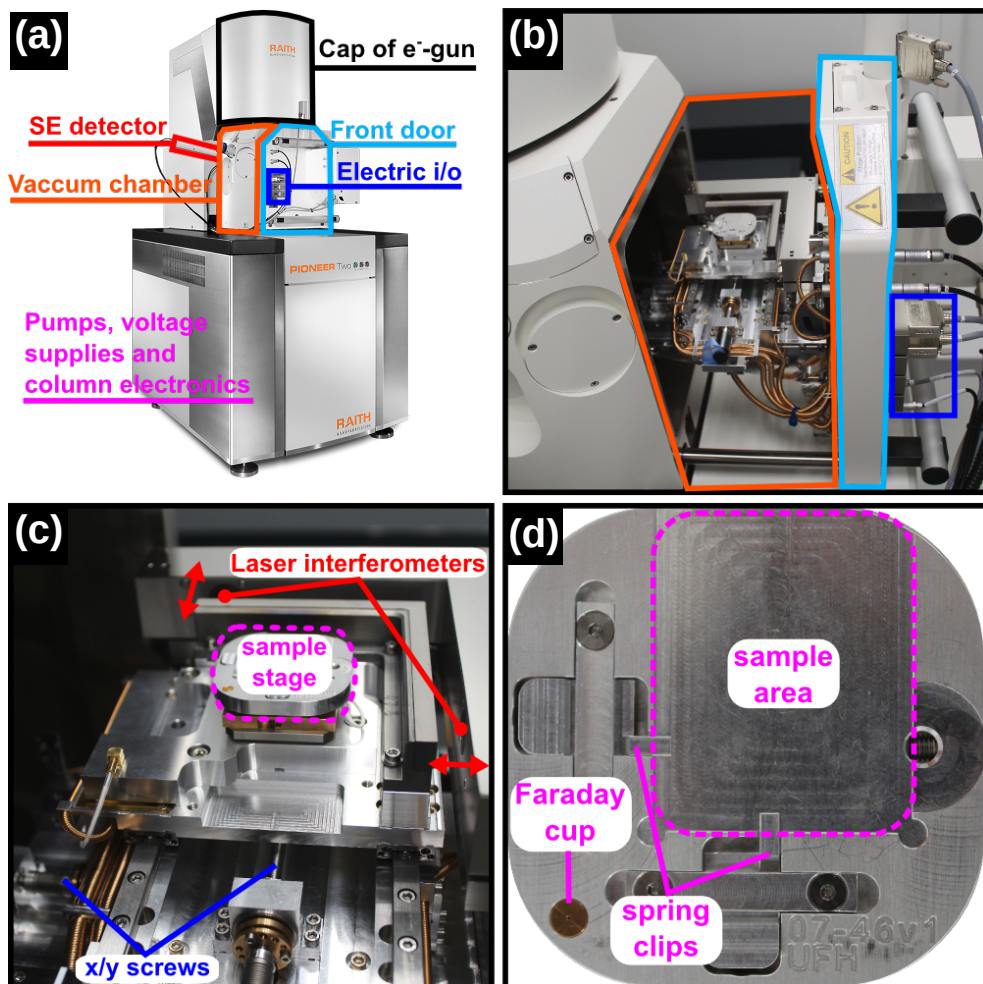


Figure 3.2: **Pioneer Two outline.** (a) Overview of the main parts of the system. (b) Inside of the vacuum chamber (orange) with electrical feedings (dark blue) through the front door (light blue). (c) Sample positioning platform. (d) Zoom of the sample holder.

3.2.1.2 Electron Beam Lithography

The Pioneer Two is provided with a software which automatizes the electron beam exposure of micro- and nanostructures with the desired dose based on proper graphical data file. High resolution is achieved thanks to high performance laser interferometers and the in lens detector. The opportunity to write patterns in several steps, for instance to make multi-layered structures or planar heterojunctions, is made possible by an integrated overlay procedure.

3.2.1.3 In situ observation during transport measurements

The possibility to observe samples while performing electromigration is a quite recent technique^[54,64]. Aiming at visualizing EM and desiring to implement this technique in our lab, we developed a dedicated platform, made of materials entirely compatible with high vacuum conditions. The electrical feedthroughs are highlighted in dark blue in Figure 3.2(a)-(b). As it is shown in Figure 3.3(a), the platform is composed of two essential parts.

The sample holder itself is made of a polymer. It includes a central area intended for the sample, surrounded by 8 copper contacts to realize connections to this sample. Each copper pad extends in a copper wire on which is soldered a serial resistance for protection (limiting the current in case of electrical discharge). A flexible tablecloth electrical connector is attached to this polymeric holder. This flexible part is extended by a more rigid yet bendable grey tablecloth connector ended by a D-sub male connector. This part of the platform is designed to be inserted inside the visualization chamber of the SEM. The sample holder and the flexible connector facilitate the fixation on the sample area (Figure 3.3(b)) while still permitting displacements of the sample stage, the rigid part with the D-sub connector makes possible the insertion in the internal side of the electrical feedthrough (Figure 3.3(c)).

The second section of the wiring, connected to the first one by a female-female D-sub adapter (see central inset of Figure 3.3(a)), is composed of a D-sub male connector prolonged by the same type of grey tablecloth electrical connector leading to a breakout box with 8 Bayonet Neill-Concelman (BNC) outputs corresponding to the 8 copper pads on the sample holder. The breakout box has been thought to satisfy requirements for avoiding electrical discharges. The role of this part of the platform is to connect to the outer part of the electrical feedthrough and to serve as an interface for connecting electrical devices (Figure 3.3(d)).

Observation in a SEM is often hampered by surface contamination during electron irradiation. The gradual build-up of carbon layers on the specimen reduces the image contrast^[65]. Contamination is caused by the cracking of hydrocarbons, present both in the vacuum chamber and on the specimen itself, and by their subsequent surface diffusion to the site being irradiated^[66,67]. This issue is particularly troublesome in the case of in situ observation because sample inspection while performing transport measurements usually spreads over several hours. For this reason, the entire vacuum part of the in situ platform is systematically and properly cleaned with isopropanol. The technique of visualization has also been adapted to minimize the time of irradiation. Indeed, instead of making movies by constantly maintaining activated the electron beam, snapshots are taken regularly during the measurements and recombined afterwards to obtain animated pictures.

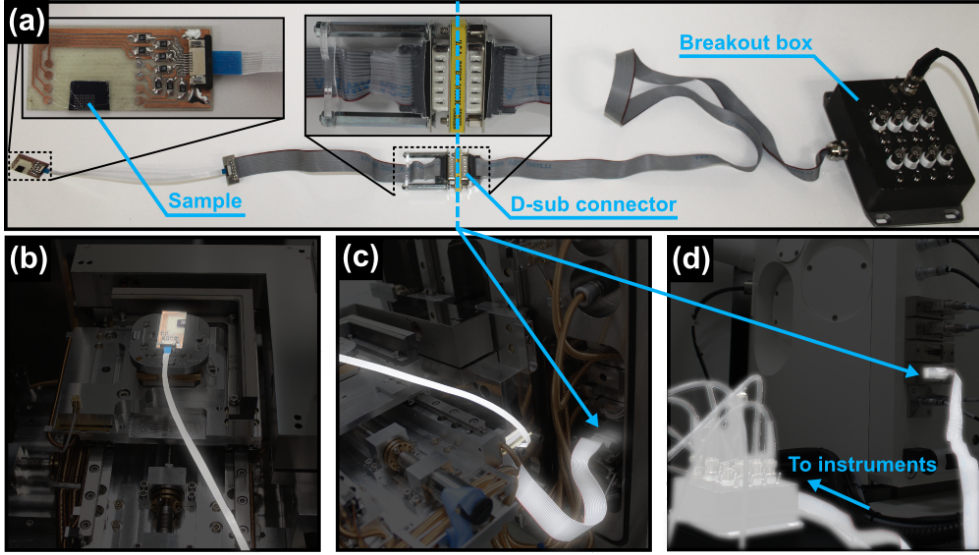


Figure 3.3: **Home-made platform for simultaneous sample inspection and electromigration** (a) Overview of the whole in situ platform including a special polymeric sample holder with protective resistances (left inset), a D-sub adapter to separate the inner and the outer parts of the base (right inset) and a breakout box with BNC connections to serve as interface for measurements. (b) Sample holder is easily placed on the platform inside the Pioneer Two thanks to its flexible connector. (c) The rigid connector is connected to the inner side of electrical feedthroughs. (d) The breakout box is plugged to the outer part of the corresponding feedthrough.

3.2.2 Fabrication processes

The patterning of the samples has been achieved by EBL and/or photolithography followed by either physical vapor deposition (PVD) or reactive ion etching (RIE). The technique is chosen in function of the material deposition conditions and availability at the outsourcing lab.

3.2.2.1 Al nanoconstrictions

Aluminum samples have been principally made at the facilities of NSM (KULeuven) and EPNM (ULiège) by using single EBL procedure, described hereafter. First, a Si/SiO₂ substrate is covered by poly(methyl methacrylate) (PMMA), a special polymer (resist) sensitive to electron bombardment. A good and homogeneous coverage of the surface is achieved by spin coating (Figure 3.4(a)). This is followed by a soft baking at 180°C to evaporate the solvent and fix the polymeric resist, as illustrated in panel (b) of Figure 3.4. The piece of PMMA-covered substrate is then placed inside the chamber of the EBL platform. The controlled electron-beam subsequently exposes

the resist, following a predefined pattern, and results in a change of solubility for the irradiated regions (cf. change of color in Figure 3.4(c)) due to the breaking of polymeric chains. This structural modification is later exploited by immersing the sample in a bath of methyl isobutyl ketone (MIBK) diluted in isopropyl alcohol (IPA), which removes these weakened portions of the resist. This phase, named development, is depicted in Figure 3.4(d). The obtained resist mask is placed, ready for metallisation, in an evaporation chamber, for example by molecular beam epitaxy (MBE) or e-beam evaporation, and a thin film of aluminum is deposited as illustrated in Figure 3.4(e). The final step consists in removing the remaining portion of resist, together with the Al covering it, leaving only the metallic parts which were in direct contact with the substrate. This last part is called the lift-off and its schematic is given in Figure 3.4(f).

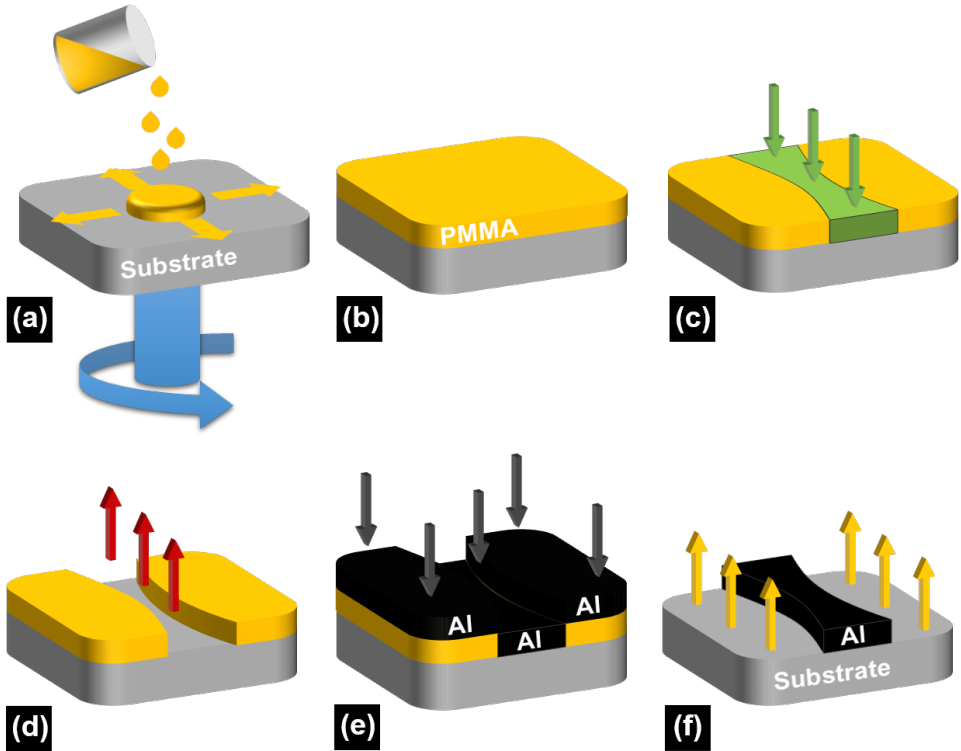


Figure 3.4: **Process flow for the fabrication of Al nanoconstrictions.** (a) Resist is first deposited by spin coating. (b) After baking at 180 °C, a homogeneous thin film of rigid resist covers the sample. (c) The sample is then patterned via EBL (d) and subsequently immersed in a chemical bath to remove the exposed resist (development). (e) Al is deposited on the obtained resist mask. (f) Al excess is finally eliminated by chemical removal of the resist (lift-off).

3.2.2.2 Nb nanoconstrictions

Niobium samples were fabricated by Prof. Roman B. G. Kramer at the facilities of Institut Néel (University of Grenoble, France). The sample fabrication procedure starts with a thin film of niobium which is initially deposited on a substrate with the desired thickness, as represented in Figure 3.5(a). A film of resist is then coated on top of it (cf. Figure 3.5(b)-(c)), patterned via EBL (Figure 3.5(d)) and developed (Figure 3.5(e)). Subsequently, an aluminum layer is deposited (Figure 3.5(f)) so that, after lift-off (Figure 3.5(g)), the Nb film is covered on the desired regions and the rest can be etched away (Figure 3.5(h)). For this step, it is important that the protective layer of aluminum has a sufficient thickness to resist the RIE process, where the plasma attacks the uncovered niobium but does not reach the protected part until the rest has been completely removed. At the end of the etching process remains a small capping layer of aluminum that can be safely removed by wet (chemical) etching (Figure 3.5(i)).

3.2.2.3 $\text{YBa}_2\text{Cu}_3\text{O}_{7-d}$ and $\text{La}_{2-x}\text{Ce}_x\text{CuO}_4$ microstructured bridges

$\text{La}_{2-x}\text{Ce}_x\text{CuO}_4$ samples were made by the group of Prof. K. Jin, at the Beijing National Laboratory for Condensed Matter Physics (Academy of Sciences, China), and $\text{YBa}_2\text{Cu}_3\text{O}_{7-d}$ samples were conceived at Institut de Ciència de Materials in the group of Dr. A. Palau (University of Barcelona, Spain). Both type of samples were made using photolithography followed by ion-beam etching. The procedure starts with the deposition of the high- T_c material by physical (here pulsed laser deposition (PLD) for LCCO)^[68] or chemical (chemical solution deposition (CSD) for YBCO)^[69] means (Figure 3.6(a)). The wafer is then covered, usually via spin coating, by a layer of photoresist, a resist sensitive to UV light (Figure 3.6(b)-(c)). After that, it is illuminated through a mask, specifically designed mechanically or by EBL (Figure 3.6(d)). In the same manner as the PMMA resist, exposure of photoresist to UV light causes a change of solubility, which can be later exploited to remove the exposed parts (Figure 3.6(e)). Note that the soluble parts are here the ones that have not been exposed, which gets them the name of negative resists. Final exposure to an ion-beam allows to get rid of the unprotected regions of LCCO/YBCO (Figure 3.6(f)) and a last chemical bath can remove the remaining layer of photoresist.

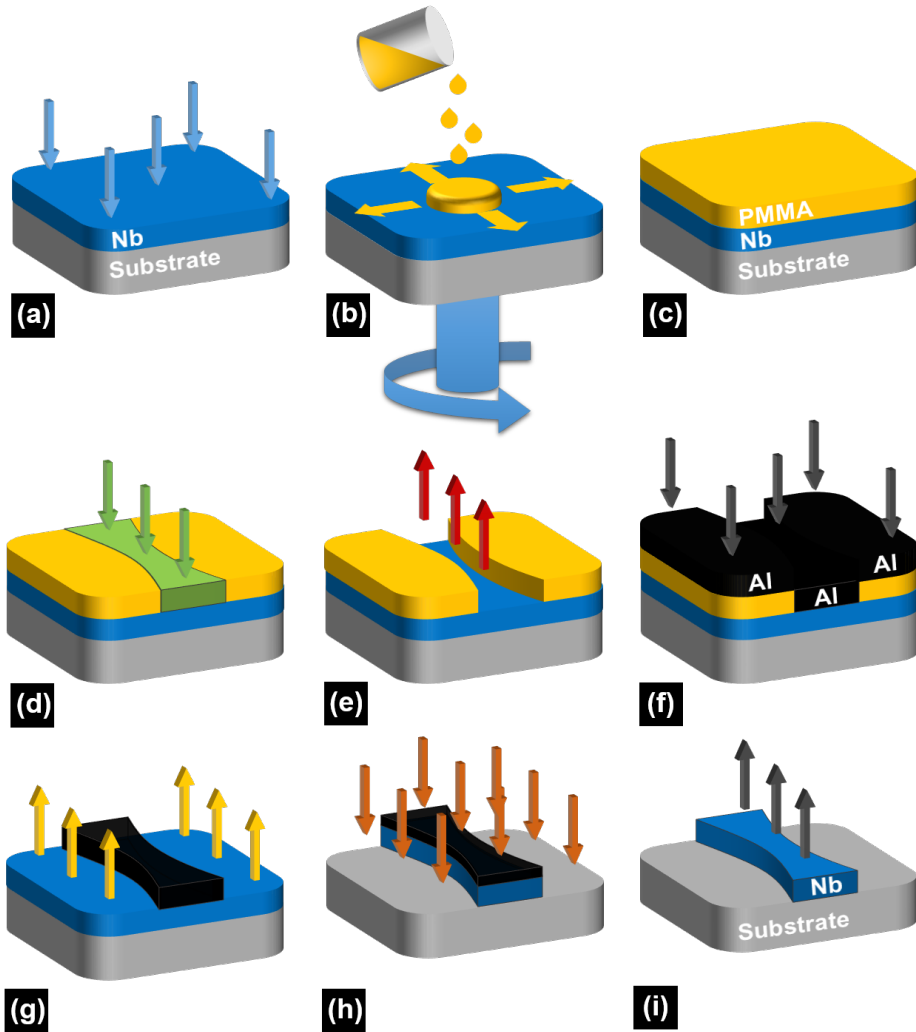


Figure 3.5: **Process flow for the fabrication of Nb nanoconstrictions.** (a) A Nb film is deposited on the sample, (b) followed by deposition of resist by spin coating so that, after baking, (c) a homogeneous thin film of rigid resist is covering the Nb film. (d) The sample is then patterned via EBL (e) and subsequently immersed in a chemical bath to remove the altered resist (development). (f) Al is deposited on the obtained resist mask. (g) Al excess is eliminated by chemical removal of the resist (lift-off). (h) Nb film is then submitted to ion etching leaving only the portion of Nb protected by Al. (i) The remaining layer of Al is finally removed by chemical etching.

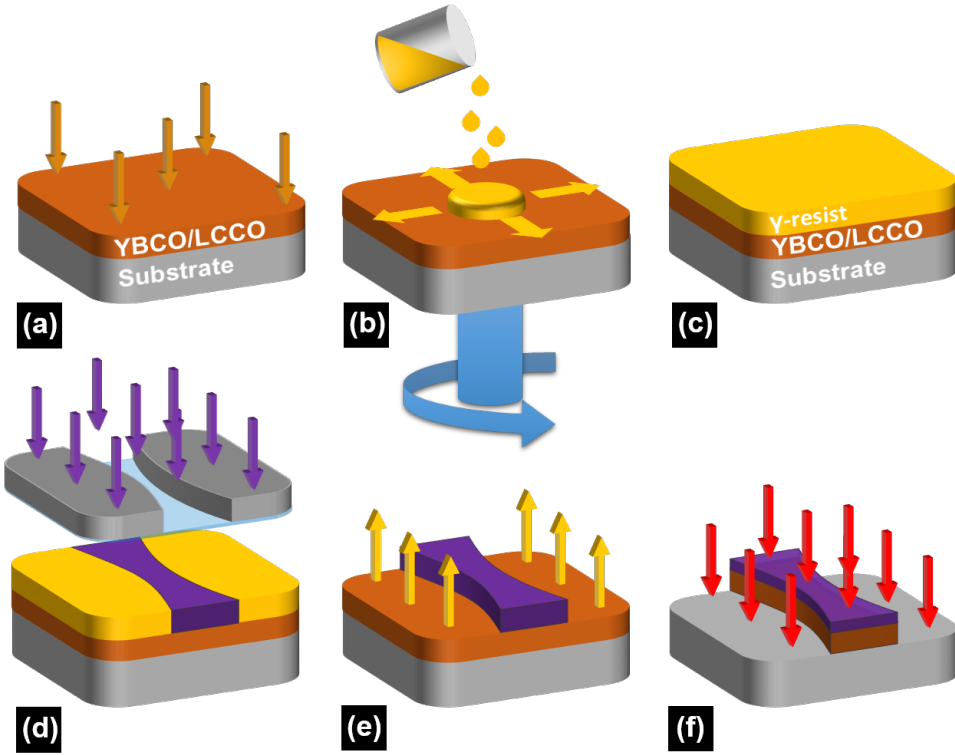


Figure 3.6: **Sketch of LCCO/YBCO samples fabrication.** (a) First, a film of LCCO/YBCO is deposited on the sample, (b) quickly followed by deposition of resist on rotating sample (spin coating) so that, after baking, (c) a homogeneous thin film of rigid resist is covering the superconducting film. (d) The sample is then illuminated through a predefined mask (e) and subsequently immersed in a chemical bath to remove the non-protected resist (development of negative resists). (f) An ion-beam finally takes care of removing the non-protected superconductor, leaving only the desired patterned film.

3.3 Cryogenics and noise filtering

One of the main goals of this work is to study the superconducting properties of nanojunctions, which in turn requires access to low temperatures by means of cryogenic systems. These systems are presented in the following three sections. Their operation is briefly described along with their main characteristics. For the sake of completeness, a small discussion concerning the different sources of noise is also present.

3.3.1 Oxford continuous flow ^4He cryostat

The Oxford continuous flow ^4He cryostat at the NSM group of KULeuven is schematized in Figure 3.7. The sample is glued on a circular sample holder that is connected

to a copper block ending the cryogenic stick. This stick includes all the needed wiring adapted to cryogenic temperatures and is designed to be inserted in the inner helium space. The outer space is occupied by the superconducting magnet. These two reservoirs are filled with liquid helium and they are interspersed by two vacuum shields for thermal isolation. A perforated cap is covering the end of the stick, thus protecting the sample and allowing it to be in direct contact with the liquid helium bath. A special tube allows venting of sample space with room temperature helium gas, thus accelerating the warming up of the cryostat and the de-installation procedure.

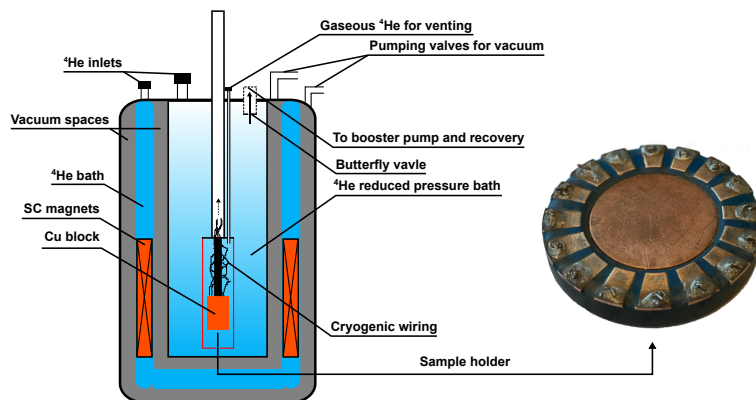


Figure 3.7: **Simplified scheme of Oxford continuous flow ^4He cryostat from KULeuven.** A perforated stick is immersed in an ^4He bath so that the sample is in direct contact with liquid helium.

The sample is initially in a liquid helium bath at 4.2 K. The cryostat is not optimized to cover the range above this temperature. Lower temperatures can be achieved via adiabatic expansion by pumping with a rotary pump combined with a high flow water-cooled booster pump. As is, the system allows the user to reach, and maintain with a nominal stability of 0.1 mK, temperatures between 1.5 K down to 1.1 K. The stability is guaranteed by an electronically-controlled butterfly valve. When this valve is fully opened, the temperature is typically situated around 1.1 K (base temperature) while the highest stable temperature is around 1.6 K when this valve is almost closed. Range between 1.6 K and 4.2 K is accessible, but without control, by stopping the pumping.

In addition to a high stability and a relatively narrow temperature window, what characterizes this system is its cooling power. The sample is indeed directly immersed in liquid helium and the corresponding cooling power is of the order of 10 W. Note that ^4He is superfluid at the working temperatures, which enhances the cooling power.

3.3.2 Oxford ^3He refrigerator

The Oxford ^3He refrigerator is also installed at the NSM group of KULeuven and consists of a commercial Heliox VL stick from Oxford Instruments inserted in a liquid ^4He bath, as depicted in Figure 3.8. The sample holder is mounted on a copper holder at the bottom of the ^3He pot. After mounting, the lower part of the stick is covered with a cylindrical vacuum cap and pumped in order to avoid thermal contact with the ^4He bath. Once insertion of the stick is completed, the sample thermalizes at the temperature of liquid helium, 4.2 K. To achieve further cooling, ^3He absorbed in the sorption pump has to be condensed. This is realized by pumping ^4He from the bath through the cooling circuit with a rotary pump. This allows the so-called 1K pot to be cooled down, its temperature being controlled by the flow through the needle valve. The ^3He gas, released by the sorption pump by warming it up with a resistive heater, condenses around the 1K pot and drop down to the ^3He pot. Once all the gas has been condensed, the temperature can be further reduced by controlling the temperature of the sorption pump and therefore the vapor pressure above the liquid ^3He .

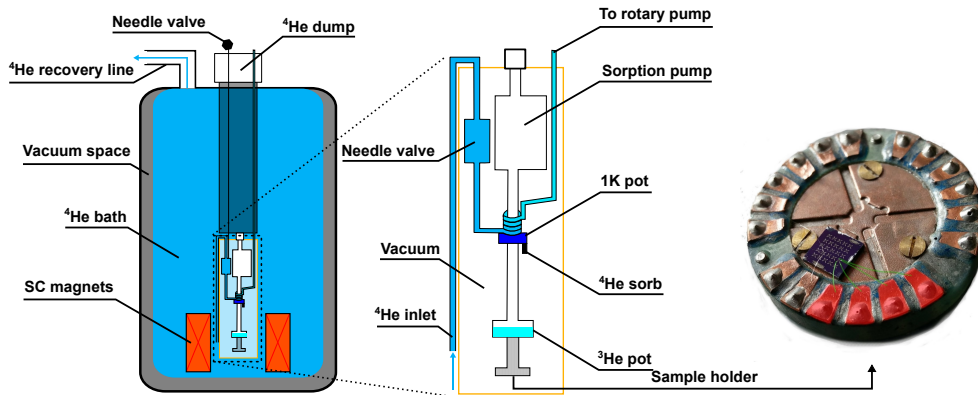


Figure 3.8: **Simplified scheme of Oxford ^3He refrigerator from KULeuven.** The stick is immersed in a ^4He bath. The sample is on a cold finger in vacuum inside the stick. A internal circuit involving liquefied ^3He allows to cool the sample to lower temperatures. A circular sample holder is mounted at the end of the stick, in close contact with the ^3He pot.

A stability of 3 mK can be achieved on temperatures ranging from 1.5 K to 0.3 K. The cooling power of the system is much lower than that obtained by immersing the sample directly in cryogenic liquid, here 40 μW at 300 mK.

The Oxford ^3He refrigerator from KULeuven was equipped with low-pass π -filters with cut-off frequency of 1 MHz at room temperature. Measurements were also conducted on a very similar system in the group of Prof. F. Tafuri at University of Naples in order to have a higher degree of filtering. This second system had electromagnetic interference filter at room temperature, RC filters with a cut-off frequency of 1.6 MHz

anchored at 1.5 K and a combination of copper powder and twisted pair filters thermally anchored at the mixing chamber of the dilution refrigerator. This latter system is described in Ref. 70.

3.3.3 Montana closed-cycle cryostation

The helium closed-cycle cryostation commercialized by Montana Instruments is located in the facilities of EPNM group at ULiège. The customized configuration consists in the basic system with an extended connection between the cryocooler and the sample chamber which maximizes the access to the sample for optical purposes. A global view of the cryostat, as well as zooms on the sample chamber and holder are represented in Figure 3.9.

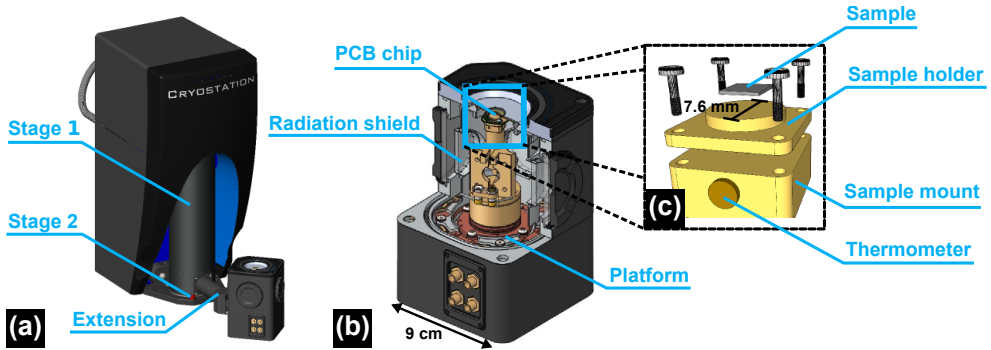


Figure 3.9: **Overview of Montana cryostation from ULiège.** (a) The cryostation is based on two cooling stages with base temperatures respectively of 30 K and 2.8 K. An extension allows to maximize the optical access to the sample chamber. (b) The PCB chip is installed in the sample chamber and protected by a radiation shield. (c) The sample can be mounted on the central circular part of the square sample holder, itself screwed to the sample mount that includes a thermometer.

It is of paramount importance to have a good thermal link between the sample, the sample holder and the sample mount. In order to achieve that, the sample is glued with silver paste on the square gold-coated sample holder. Apiezon N vacuum grease is used between sample holder and sample mount to fill in the apertures, the layer of grease being as thin as possible to avoid thermal isolation as its thermal conductivity is situated around $0.1 \text{ Wm}^{-1}\text{K}^{-1}$. The sample holder and the sample mount are made of oxygen-free high thermal conductivity copper (also called C101 or OFE), which has a thermal conductivity of $630 \text{ Wm}^{-1}\text{K}^{-1}$, more than twice the value of standard grade copper (C110). In this configuration, the cryostation can achieve a minimum base temperature of 3.5 K. The accessible range extends up to 150 K with a stability of the order of 1 mK for large periods of time. Values situated between this upper limit and room temperature are gradually and fleetingly accessible during the cooling down or

the warming up of the cryostat. The cooling power at the sample level is 100 mW at the base temperature. The cooling is based on the principles of the Gifford-McMahon cycle who is discussed in details in the original paper of W. E. Gifford^[71]. More details about this cryostat conception and operation can be found in Ref. 72.

3.3.4 Relevant types of noise in the system

Electronic noise is generally defined as the combination of unwanted disturbances in an electrical signal^[73]. This vague definition could be made more accurate by excluding distortion and interferences that are also undesired disturbances of a signal but are typically distinguished from pure noise.

In the absence of an external signal, the quantity measured by a sensor (for example, an electrical voltage V) will fluctuate about an average value $V_{average}$ ^[74]. This noise can be described more accurately by recording $V(t)$ over a certain time t and then expressing it in terms of its Fourier transform in frequency space. In this case, one obtains the distribution of the spectral power $S_\omega = dV^2(\omega)/d\omega$, known as power spectral density or simply power spectrum. The dimension of S_ω is $[V^2/\text{Hz}]$ ^[74]. For a given bandwidth $\Delta\nu$, the root mean square voltage noise is given by

$$V_{rms} = \sqrt{S_\omega} \sqrt{\Delta\nu}. \quad (3.1)$$

A standard classification of noises is based on the frequency dependence of the power spectral density $1/\nu^\alpha$. While white noise corresponds to a signal whose spectrum has equal power within any equal interval of frequencies ($\alpha = 0$, no frequency dependence)¹, red, pink, blue and purple noises refers to $\alpha = 2, 1, -1, -2$ respectively.

3.3.4.1 Johnson-Nyquist noise

This is a type of white noise whose origin lies in thermal agitation of the charge carriers which happens regardless of any applied voltage. When limited to a finite bandwidth, thermal noise has a nearly Gaussian amplitude distribution^[75]. The power spectral density is given by,

$$S_\omega = 4k_B T R. \quad (3.2)$$

In our system, we can thus expect thermal noise levels of the order of nanovolts or lower, depending on operation temperature and bandwidth.

¹That name was given by analogy with white light, which was (incorrectly) assumed to have such a flat power spectrum over the visible range.

3.3.4.2 Shot noise

Shot noise is also a type of white noise but distinct from thermal noise in the sense that it consists of additional current fluctuations that occur when a voltage is applied and a macroscopic current starts to flow. The result, by Schottky, based on the assumption that the statistics of electrons passage is Poissonian, reads for the spectral noise density^[76],

$$S_{\omega} = 2eRV_{average}. \quad (3.3)$$

This type of noise could be significant if we consider very small currents (nanoamperes) and large bandwidths (short time scales, nanoseconds), which is not our case. Considering its independence on temperature, it is expected to become the dominant source of noise at very low temperatures.

3.3.4.3 Flicker noise

Flicker noise is the only example of pink noise and is thus often referred as "1/f" noise. Its power spectral density is not well defined, depending strongly on the underlying mechanisms^[77], but is clearly inversely proportional to the frequency,

$$S_{\omega} \propto \frac{1}{\nu}. \quad (3.4)$$

Depending on the case, its origin can be attributed to presence of impurities, parasitic electron-whole recombinations, etc. It is strongly related to direct current and one can thus minimize it by working with a high frequency alternating current^[77].

3.3.4.4 Coupled noise

In addition to all the sources of noise in the circuit itself described above, other noise energies can be coupled into a circuit coming from the external environment. Among all the possible sources, let us cite cosmic noise, static noise, industrial noise,... The radiation shield, pi-filters (low-pass), twisted pair filters and copper powder filters used in our experiments are there to minimize their influence.

3.4 Avoiding electrostatic discharges

Electrostatic discharges (ESD) are the nightmare of any scientist working with tiny conductive samples. They are unpredictable: they can happen anywhere at any time and their causes are often unclear. Especially in our case, with nanoscale aluminum and niobium samples², the consequences can be disastrous. It is not uncommon that

²YBCO and LCCO are far from being good conductors and thus are less susceptible to this kind of issue.

sample breaks just after the 24-hours-long installation or between two measurements during a successful campaign of measures. In order to avoid this painful setback and the consequent frustration, it is imperative to respect a protocol for careful handling of the samples.

Usually, as long as the sample is not installed, meaning that its pads are all floating, the risk of failure is negligible. It was indeed confirmed during our investigations that disconnected stored samples stay alive with no exceptions. The problems start when samples are connected, in our case using a wirebonder. This is the reason why a technique known as make-before-break (MBB) in engineering sciences has been adopted. The basic principle behind consists in maintaining all the sample pads at the same potential, preferably the ground, and disconnect them from each other only when it is required and after they were connected to devices, typically to perform a measure. In the next sections, we detail the specific adaptations made to each device so that these requirements can be satisfied. We allow ourselves to warn the reader here that what follows is rather technical and aims at furnishing to future users a small guide for anti-ESD protocol.

3.4.1 Sample holder

Three types of sample holders have been used, one for each cryostat. They may look different in shape but they are exactly the same in essence. Considering this similarity, only one model will be described, say the one of the Montana cryostation. The same remark applies to wirebonding and installation in a cryostat.

The first part of the sample holder consists in a small square piece possessing a central circular area of 7.6 mm in diameter and adapted to our cryostation (Figure 3.9(c)). On this gold sub-holder is screwed a homemade printed circuit board (PCB) compatible with electric connections of the cryostation. The combined result can be seen in Figure 3.10(a). It includes 4 rows of 5 gold contacts, forming a square around the sample area, making the sample connection quite flexible.

In addition to that, a breakout box, of which a side view is displayed in Figure 3.10(b), was specifically designed to be very stable and adjustable in height, thanks to a large threaded foot, to satisfy wirebonding requirements. This bonding base is meant to host the PCB with the sample glued on it. Indeed, visible in Figure 3.10(c), the central area of the platform possesses four rows of plugs adapted to the PCB dimensions. All these plugs are connected to corresponding BNC connections, situated in the periphery of the platform. Protective $270\ \Omega$ resistances are placed on each line and as close to the sample as possible to limit the current in case of ESD.

When a connected sample is present on the bonding platform, the corresponding BNC are always covered with end caps (Figure 3.10(b) and (c)). Their role is to

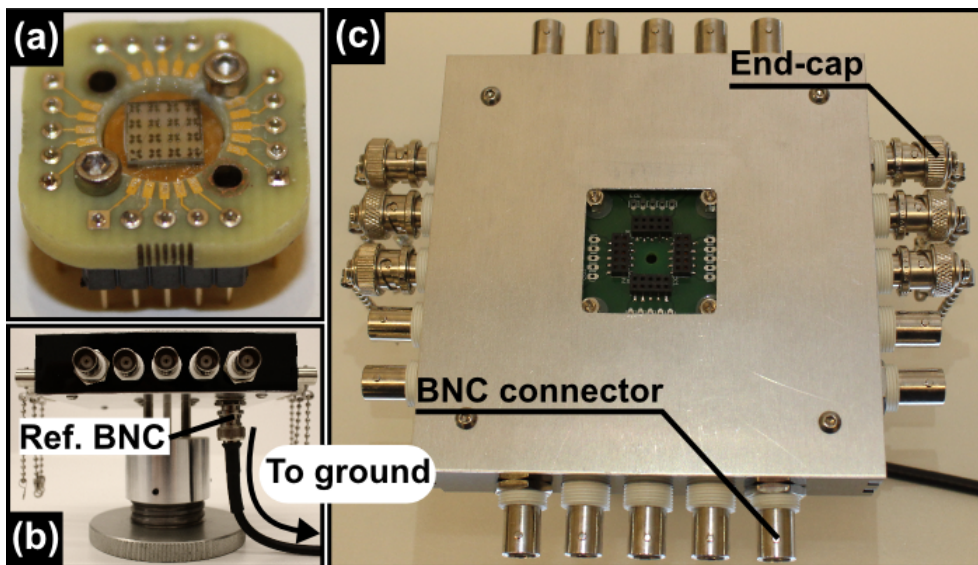


Figure 3.10: **Sample holder and bonding platform.** (a) Sample pasted on the homemade PCB, especially designed to adapt to the gold sample holder of the Montana cryostation. (b) Side view of the bonding platform. A large foot, adjustable in height thanks to a screw thread, ensures a high stability. Bottom BNC connection can be connected to a chosen reference. (c) Top view of the same bonding platform. Central area is made to receive the sample on its PCB holder. The twenty available gold pads of the PCB are directly linked to side BNCs.

connect the inner part of the coaxial connection to its outer part. In our design, the outer parts of the peripheral BNCs are all connected to the bottom BNC, visible in Figure 3.10(b). They are thus all connected together, and by plugging the ground (or any other reference) to this bottom BNC, they are then all in a common potential. As additional precaution, the operator should wear a conductive bracelet also connected to the same reference.

3.4.2 Wirebonding

The wirebonder at EPNM is an iBond5000 Series produced by Kulicke & Soffa (Figure 3.11(a)). It is a mechanical wedge bonder with an advanced graphical user interface. It can achieve wedge bonding on a variety of materials (Au, Cu, Pb, Al,...) with different types of wires (Au, Al, Cu, ribbon). It has a deep access capability, which means that the feeding of the wire through the needle is vertical, as it is illustrated in Figure 3.11(b). It allows our bonder to access regions with complex relief, which could be inaccessible with conventional 45 degrees wire feeding.

The principle of bonding is simple and is depicted in Figure 3.11(b). The idea is that the needle will apply force in combination with ultrasonic power to make the wire

adhere to the surface. In the case of our design, the first bond is made on a pad of the PCB and the second bond is realized on the sample pad. The result can be seen in Figure 3.11(c) which shows a sample with four bonded pads. High stability and well-adjusted height compared to the needle are required to obtain good bonds, hence the previously described design of the platform.

Prior to sample bonding, a connection scheme is made and the most adequate pads of the PCB are chosen. Then the corresponding BNC connections are all covered with end caps, so that sample pads will be all short-circuited after bonding. The bonding needle, when getting in touch with a pad of the sample, could produce ESDs. This is why the reference of the bonding platform is also connected to the reference of the wirebonder (including the needle). In this way, the needle is always at the same potential as all the sample pads.

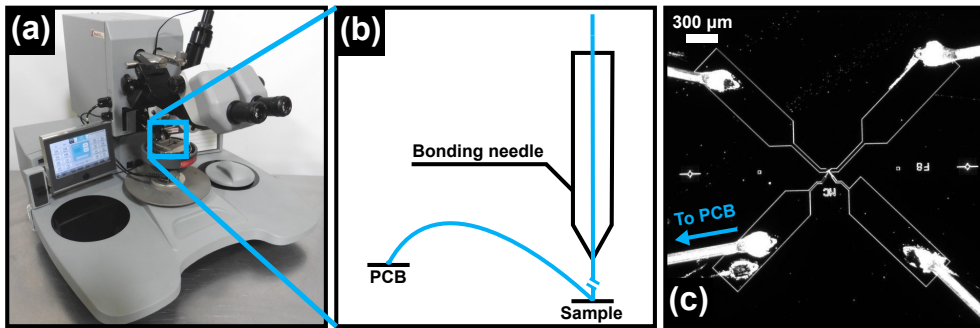


Figure 3.11: **Wirebonding process.** (a) Picture of iBond5000 Series wirebonder from ULiège. (b) Sketch of a needle used to perform a bond between a pad of the holder and a pad of the sample. (c) Optical image, in dark field for better high contrast, of a bonded sample with a typical layout.

3.4.3 Installation

Before installation, a natural step consists in checking if the sample has survived to electrical connection. The bonding platform has been thought also for that purpose. To check the condition of the sample, we disconnect the reference from the bottom BNC, we disconnect all the end caps and we check all pairs of contact by using a voltage source with pre-applied 1 mV and a compliance of a few microamperes. Observation of a flowing current (usually around 1 μ A) corresponding to the resistance expected from our sample and its leads confirms the survival of our sample. Once it has been established for all contacts, we reconnect all the end caps and the reference and we proceed to installation. Depending on the type of measurements, the procedure is slightly different, mostly because the sample holder is also different. We detail hereafter the installation in a cryostat for low temperature measurements and in an

electron microscope for in situ transport measurements.

3.4.3.1 Cryogenic environment

The installation in the cryostat necessitates to take the PCB with the sample paste on it (Figure 3.10(a)) out of the bonding platform (Figure 3.10(c)) and to put it inside the cryostat (Figure 3.9). One can directly see that there is no choice but to have the sample with all its contact floating in an intermediate state. The idea is to ensure that there is no potential difference between the bonding platform and the cryostat. To satisfy this criterion, we have equipped our cryostat with a box that serves as an electrical intermediate between devices and cryostat inner connections. This home-made adapter is showed in Figure 3.12(a).

In Figure 3.12(b) is given an explicative scheme for the first three BNC connectors, which can be straightforwardly extended to all the connectors of the box possessing right and left switches. As it can be understood from Figure 3.12, each BNC connector possess a right (R) and a left (L) switch. There is also a general (G) switch in blue and a plug for the reference (REF) in red. When a L-switch is in position A, the line is open and the corresponding BNC is disconnected from the pin inside the cryostat. In position B, the line is closed and the BNC allows connection to the inside pin. When a R-switch is in position B, it means that the line, downstream from L-switch, is isolated from the common line. Of course, when a R-switch is closed (position A), the corresponding line is connected to the common line. The G-switch is unique to the box and allows to connect (position A) or disconnect (position B) the common line from the REF-plug. Finally, REF can be plugged to the chosen reference, usually the ground.

The initial condition of the sample that has to be transferred to the cryostation corresponds to it being plugged in the bonding platform. All BNCs corresponding to bonded pads are covered with end caps and the ground is connected to the bottom BNC, which means that all sample contacts are connected together and to the ground (cf. Sample holder section). The same ground is then connected to the REF of the cryostat connection box and we make sure that, when connected: sample will be isolated from the external world (L-switch in position A), all of its pads will be connected together (R-switch in position A) and to the ground (G-switch in position A). In this way, the transfer results in passing from a position where all contacts are grounded (bonding platform) to a position where they are still all at the same ground (cryostat).

The only remaining issue is the intermediate state where the sample is with all its contacts floating. Usually, this is not sufficient to cause failures. For particularly fragile samples (Al samples for example), further protection is provided by an air ionizer. This

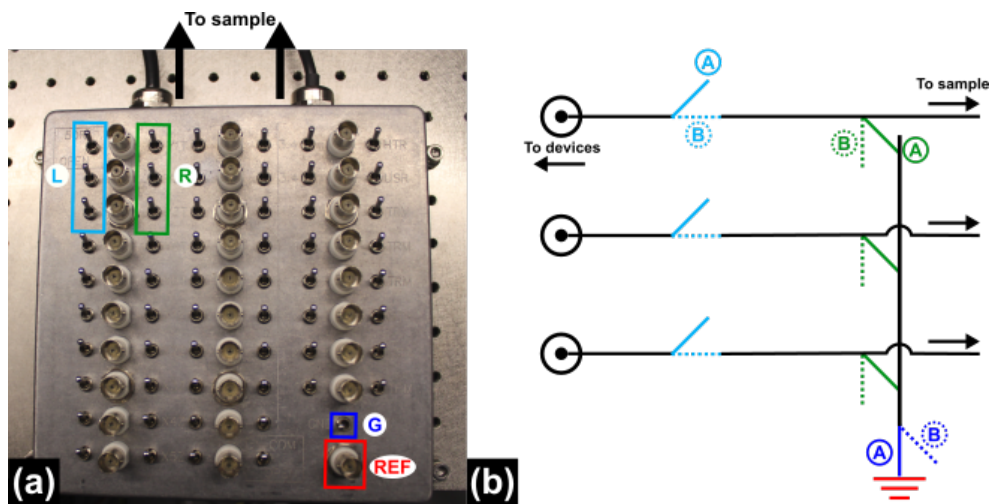


Figure 3.12: **Overview and technical scheme of an anti-ESD box.** (a) Picture of the box with multiples BNCs connected to inside pins of the cryostation. A typical box possesses two switches per BNC (light blue and green rows), a general switch (blue) and a plug for a reference (red). (b) Technical scheme of the box, with corresponding colors.

instrument is often used to reduce static electricity build up in electronics. Here we use it during the transfer, connected to the same and shared ground between bonding platform and cryostat. Its presence improves the survival chances of our sample during transfer. A sketch of the transfer procedure to the cryostation is shown in Figure 3.13.

3.4.3.2 Electron microscope

The installation of the samples into the electron microscope requires slightly different anti-ESD procedures. This is mostly due to the fact that the sample holder is not the same. Indeed the sample is directly glued on the small polymeric plate of the in situ platform, which possesses already its own MBB box (black box in Figure 3.3). Thanks to this box, whose mechanism is exactly the same as the box of the cryostat, sample contacts can be put together to the ground. For wirebonding, a reference connected to the needle can also be plugged.

When installation starts, the platform is separated at the level of the D-sub adapter. The part with the box is first connected to the external part of the electrical feedthrough of the Pioneer while, in a second time, the flexible part with the sample is placed on the sample holder and connected to the internal part of the corresponding electrical feedthrough. Thereby the sample is again floating and reconnected to the same ground through the door. In the same way as for the cryostat, for delicate samples, an air ionizer connected to the same ground can also be used. A sketch of

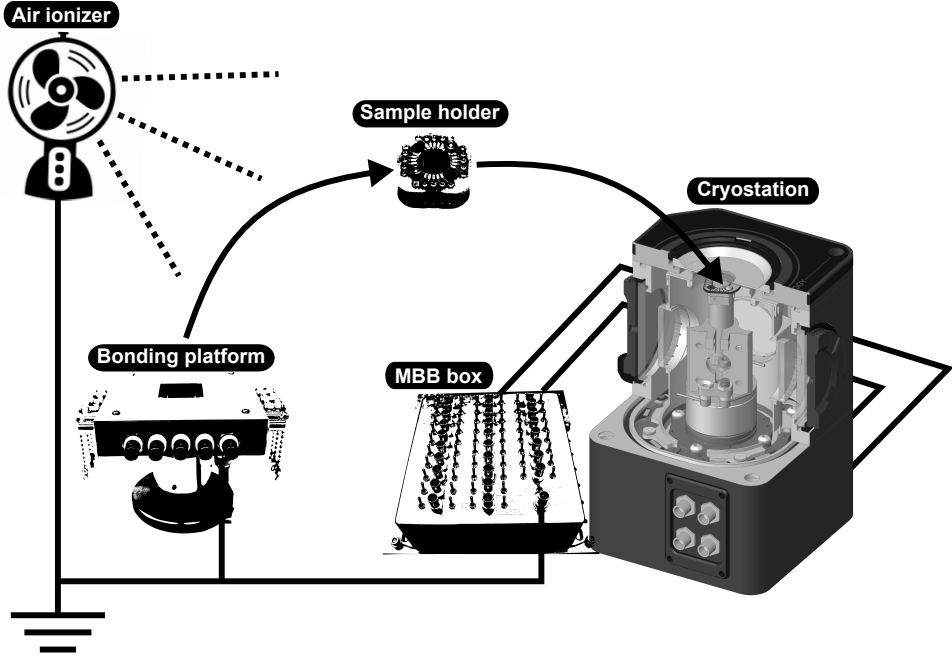


Figure 3.13: **Schematic view of sample transfer to cryostat.** The sample is initially taken out of the bonding platform and connected to the cryostat. Both departure and arrival points share the same ground. This, in combination with the use of an air ionizer, is supposed to drastically reduce the risk of ESDs.

the installation in the EBL Pioneer Two is shown in Figure 3.14.

3.4.4 End of installation

After the installation and before proceeding with measurements the box is initially in the state $(L, R, G, REF) = (A, A, A, \text{Ground})$ so that the sample is isolated from any exterior perturbations and its pads all connected together and to the ground (see Figure 3.12). The first step is to connect all necessary devices to the corresponding BNC on the box, and to turn them on. As the connections are completely disconnected from the sample, this has to be done as a start because turning on a device can result in spikes being produced by internal circuitry changes. The second step is to put L-switches on position B, so that connection is established between devices and sample. At this stage, $(L, R, G, REF) = (B, A, A, \text{Ground})$ sample pads are still all grounded so that sample is protected. The final step is to put the G-switch and then R-switches to position A so that sample pads are first floating and then are disconnected from each other, $(L, R, G, REF) = (B, B, B, \text{Ground})$. At this stage, one can proceed with measures.

Before switching to other devices, everything has to be disconnected. To achieve

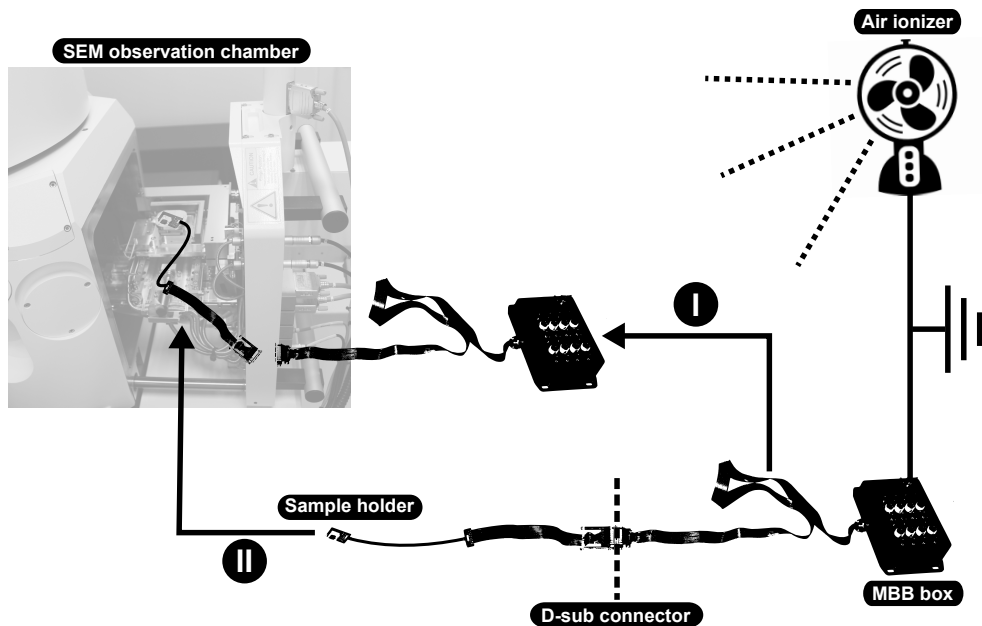


Figure 3.14: **Schematic view of sample transfer into the electron microscope.** The in situ platform is initially separated in its two sub-parts and connected at the corresponding feedthroughs, outside and inside the cryostat. The outside part has to be put in place first to be sure that the ground reference is connected when the inner part including the sample is plugged in. An air ionizer can also be used to increase the chances of success.

that, one must simply keep the devices on (to avoid spikes) but ensures that nothing is applied. At first R-switches, and then the G-switch, can be put to position B, the system thus ending up in the state $(L, R, G, REF) = (B, A, A, \text{Ground})$. Sample pads are then protectively grounded. L-switches can thus be opened, $(L, R, G, REF) = (A, A, A, \text{Ground})$, so that lines going to the sample are opened. In this configuration, it is safe to change any cables going to the box.

Finally, when measurements are finished, either one should desire to stop there or to come back and continue the day after. In the first case, complete disconnection as described in the last paragraph followed by de-installation is sufficient. In the second eventuality, one usually leaves the sample connected to devices with a small current (a few microamps) passing through. This has proven to be a more stable and thus safer solution than trusting the quite unstable ground reference.

Chapter 4

Anti-electromigration of superconducting nanowires

This chapter is largely based on the following work:

X. D. A. Baumans *et al.*, *Healing effect of controlled anti-electromigration on conventional and High- T_c superconducting nanowires*, *Small* **13**, 1700384 (2017).

4.1 Introduction

Arguably, one of the most appealing aspects of EM is the reversibility of the mechanism. Indeed, it has been shown that nanogaps, once created, can be closed by using voltage spikes^[48,55] whereas refilling of previously generated voids has been demonstrated in metals such as Al and Pd-Pt^[64,78,79] by simply reversing the polarity of the dc current.

In this chapter, we introduce controlled EM as a powerful tool to explore superconducting nanoconstrictions. We show that this technique successfully works for Al, Nb, and $\text{La}_{2-x}\text{Ce}_x\text{CuO}_4$ (LCCO), three dissimilar superconductors. The reversed migration, here coined as anti-electromigration (anti-EM), allows us to heal the modifications previously produced by EM and partially recover the original superconducting properties of the nanoconstriction. In addition, we establish the possibility to fine-tune the resistance of such a nanowire by using successive runs of EM/anti-EM. A similar effect is observed in non-conventional (cuprate-based compounds) superconducting microbridges, whereas it works only partially in Nb. In addition, we investigate an alternative controlled EM procedure consisting of electro-pulsing. This method is more accurate in terms of reaching the aimed resistance, is faster than continuously monitoring EM, and much simpler to implement without the need of complex feedback loop controllers. The presented effects could be used as an appealing and interesting alternative for manipulating the superconducting properties of nanowires. Particularly relevant is the possibility to reversibly change the stoichiometry of high temperature superconductors without the need to fabricate different samples.

4.2 Investigation of anti-electromigration on conventional and high- T_c superconductors

The investigation has been conducted on three different superconducting compounds, Al ($T_c=1.39$ K), Nb ($T_c=8.7$ K) and $\text{La}_{2-x}\text{Ce}_x\text{CuO}_4$ (LCCO, $T_c=26.1$ K), covering a wide range of superconducting parameters (see next subsection). All samples consist of a transport bridge with a central constricted section, as it is shown in Figure 4.1 for Al [a,b], Nb [d,e] and LCCO [f-h]. The sudden reduction of the width at the centre of the bridge is intended to increase the probability to migrate atoms in its vicinity. This is a natural consequence from the fact that electromigration is driven by temperature T and current density J as described by Black's formula for the mean lifetime of the nanowire (Eq. 2.20)

Figure 4.1c represents a simplified diagram of the main algorithm used to control EM. For all measurements presented in this chapter, the electromigration has been

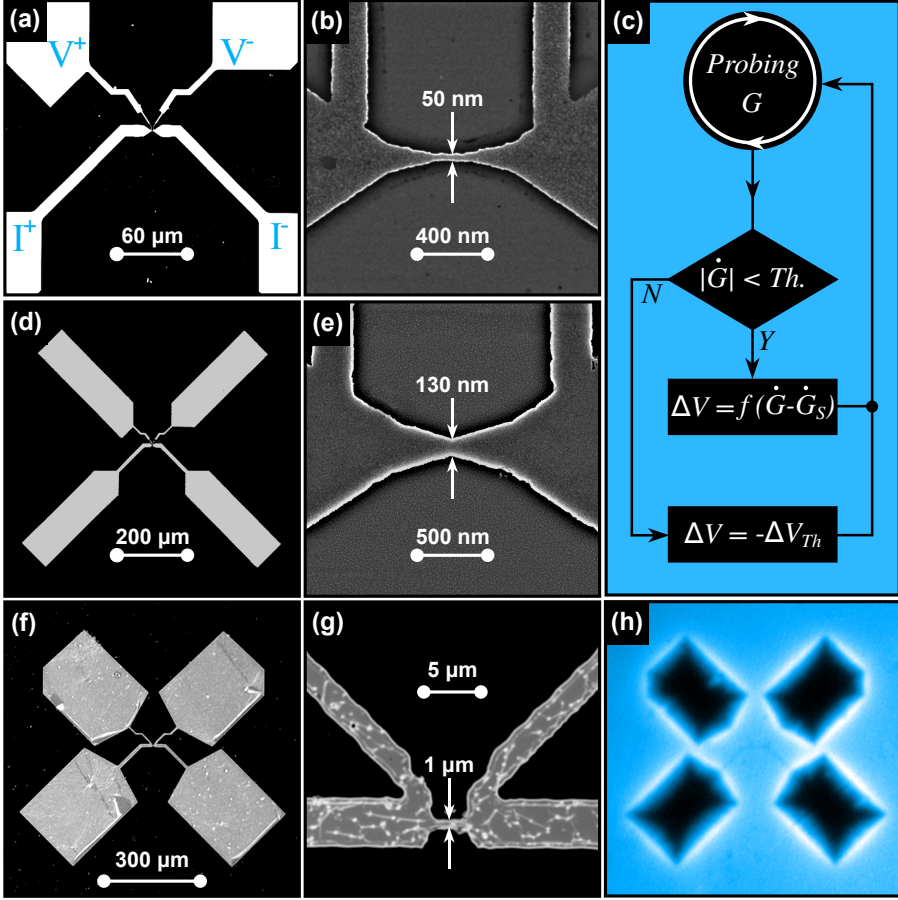


Figure 4.1: **Sample layout and flowchart of the control feedback loop.** (a-b) Scanning electron microscopy images of the investigated Al samples obtained for two different magnifications. (c) Schematic diagram of the algorithm used to achieve controlled electromigration. (d-e) Scanning electron microscopy images of the investigated Nb samples obtained for two different magnifications. (f-g) Optical microscopy images of the investigated LCCO samples at two different magnifications. (h) Magneto-optical image of a LCCO sample obtained at $H = 1$ mT and $T = 3.6$ K, illustrating the smooth penetration of magnetic flux.

carried out in a cryogenic environment with bath temperature T_B just above the critical temperature of the concerned superconductor.

4.2.1 Samples technical details

Aluminum samples were patterned by EBL on a Si/SiO₂ substrate (750 ± 50 μm Si, 300 ± 25 nm SiO₂) covered by a double layered PMMA resist mask, using a nanofabrication system from Raith GmbH. Subsequently, an Al thin film (~ 25 nm) was de-

posited using MBE with a deposition rate of 1 \AA/s and a pressure in the chamber under 10^{-8} mbar. The deposition was followed by a lift-off process. Scanning electron micrographs showing the sample layout with different magnifications are shown in Figure 4.1a-b. Figure 4.1c sketches the combined digital feedback loops used to carry out controlled electromigration. It consists of two algorithms working in parallel while ramping up the voltage: one intended to stabilize EM rate and another to prevent thermal runaways in case of fluctuations in the junction. In that context, $Th.$ represents the threshold rate defining thermal runaway, $f(\dot{G} - \dot{G}_S)$ the feedback function minimizing $|\dot{G} - \dot{G}_S|$, \dot{G}_S the desired EM rate (set-point) and ΔV_{Th} the bias change needed to damp the thermal runaway.

The Nb samples with a thickness of 50 nm have been deposited by electron beam evaporation under a pressure of 10^{-8} mbar at a rate of 1.5 \AA/s . On top of it, 5 nm of Si has been deposited for protecting the samples (pressure of $3 \cdot 10^{-9}$ mbar and rate of 0.5 \AA/s). The lithographic electron exposure has been carried out in a Nanobeam nB5 platform with an electron beam energy of 80 keV. Afterwards, an aluminum mask was fabricated by e-beam evaporation, followed by a lift-off. To remove the Nb not covered by the aluminum, we performed reactive ion etching using SF_6 during 10 s. Finally, the aluminum was removed using the base developer MF-26A. Scanning electron micrographs showing the sample layout with different magnifications are shown in Figure 4.1d-e. The initial constriction width was about 130 nm, as indicated in Figure 4.1e.

The 100 nm thick high- T_c (LCCO) films were grown on (001)-oriented SrTiO_3 substrates by pulsed laser deposition, at temperatures ranging from 720 to 760 °C in an atmosphere of 0.13 mbar of pure oxygen. After the deposition, the films were annealed at the same temperature in vacuum for a few minutes to remove the excess of apical oxygen atoms, which are harmful to the superconductivity of electron-doped superconductors. The films were then slowly cooled down to room temperature in vacuum and finally patterned into microbridges by photolithography and Ar ion beam etching. Optical microscope images of the complete layout and the microconstriction are shown in Figure 4.1f and g, respectively. The white lines and dots observed in Figure 4.1g correspond to leftovers of the polymer resist mask and have no influence on the superconducting properties of the system. Figure 4.1h shows a magneto-optical image of a LCCO microbridge, evidencing a smooth penetration of magnetic flux into the sample. Dark areas correspond to low fields, while blue-white regions represent high fields. The homogeneity of the penetration is a strong indication of the high quality of the film, confirming excellent superconducting behaviour and absence of macroscopic defects. More information about the magneto-optical setup can be found in Ref. 80.

4.2.2 Electromigration of Al nanoconstrictions

The polycrystalline structure and the associated grain boundaries have been recognized as essential ingredients for explaining electromigration. This has been clearly demonstrated by the fact that electromigrating Al single crystals is considerably more difficult than EM polycrystalline Al^[24]. While electromigration of relatively large (several micrometers) Al bridges has been reported in Ref. 23,78,79, little is known about electromigration in nanoscale Al wires and constrictions. Figure 4.2a shows a typical evolution of the sample resistance, R , as a function of the applied current, I , during a controlled electromigration process of Al. The nearly parabolic increase of R with increasing I arises from the local increase of temperature due to Joule heating. Indeed, on the one hand, the sample resistance is given by $R(T) = R(T_B)(1 + \alpha_T(T - T_B))$ with α_T the thermal coefficient. On the other hand, the temperature at the constriction results from the balance of input power, $R(T)I^2$, and heat removal $h_r(T - T_B)$, which gives $R(I) \approx R(T_B)(1 + \alpha_T R(T_B)I^2/h_r + \mathcal{O}(I^4))$, where h_r characterizes the heat removal mechanism which combines heat transfer to the substrate, the thermal conduction towards the leads, χ , and the convection with the surrounding medium (liquid He in the present case). For Al, this part of the $R(T)$ curve is fully reversible and does not lead to mass transport. Electromigration takes place in the region where the current through the constriction diminishes while the resistance increases. This regime with negative dR/dI is irreversible and leads to permanent damage of the nanoconstriction as evidenced by the SEM image shown in the inset of Figure 4.2e. A careful look at this SEM image reveals two important features. First, the void does not take place exactly at the isthmus of the constriction. This is a consequence of the fact that EM occurs mainly along grain boundaries and it is not solely ruled by the point of highest current density. Second, the section of the constriction on the right hand side of the void does not exhibit the same granularity as the virgin sample. This observation lead us to believe that a change of crystalline structure happened during the EM process. This is in agreement with previous investigations^[52].

Notice that EM starts at $I \sim 5$ mA, corresponding to a maximum current density of 400 MA/cm^2 at the narrowest point along the bridge. This value is obtained with a constant rate of decreasing conductance dG/dt . Based on Eq. (2.20), we can conclude that the lower the T , the higher the J needed for achieving the point where dR/dI changes sign. This is confirmed by the linear relation between $\ln(J)$ and $1/T$ as shown in the inset of Figure 4.2g. Here the (T, J) points correspond to the maximum current density and the local temperature at this current value. The slope of this graph provides an activation energy $U \sim 0.3 \text{ eV}$ which is significantly smaller than the 1.4 eV for the lattice self-diffusion of Al^[81,82] but not far from the 0.48 eV reported by Black^[23] in polycrystalline samples. This is not surprising considering that both,

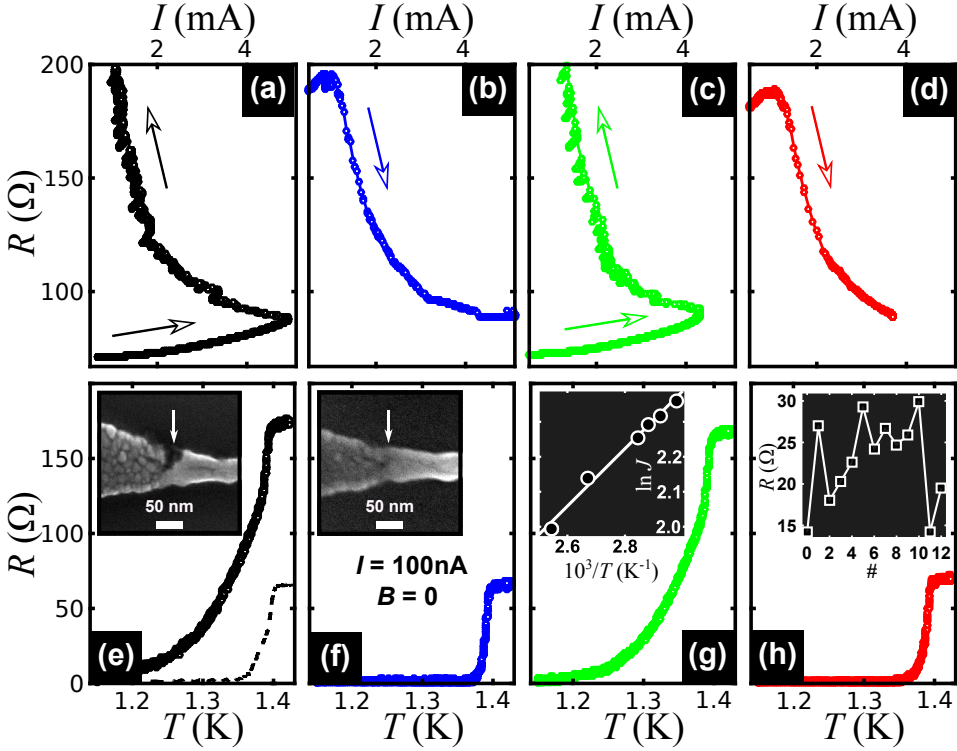


Figure 4.2: **Anti-electromigration in Al nanowires.** (a-d) Electromigration curves showing the evolution of resistance as a function of current. Panels (e-h) show the $R(T)$ curves obtained after each EM ((e) and (g)) and anti-EM ((f) and (h)). Insets in (e) and (f) are scanning electron micrograph evidencing the creation and healing of a void at the constriction of the nanowire. The dashed line in panel (e) shows the response of the virgin sample. The inset in panel (g) shows the linear relation between $\ln J$ and T^{-1} , for the (T, J) points corresponding to the maximum current density and local temperature. Inset in (h) represents the chronology of the resistance obtained during 12 successive runs of EM/anti-EM on the same nanowire at $T_B = 1.5$ K.

grain boundary and surface diffusion, are the predominant transport mechanisms with a reduction factor depending on the size of the grains^[27]. When constructing the plot shown in the inset of Figure 4.2g, care must be applied to calculate the temperature T at the constriction, which can largely exceed the bath temperature T_B . Numerical simulations of the heat transfer equation for our particular geometry and cryogenic environment^[50] showed that the electromigration starts when the local temperature at the constriction is about $T \sim 200$ K for $T_B = 1.5$ K. Similar values can be obtained using the analytic expression for the temperature of the current-heated nanowire given in Ref. 83. A rougher albeit simpler estimate of the temperature along the parabolic segment of the $R(I)$ curve can be obtained from the expression,

$$T = T_B + \alpha_T^{-1} \frac{R(T) - R(T_B)}{R(T_B)}, \quad (4.1)$$

This formula is valid as long as a linear temperature dependence of the resistance and no change of the structure of the system is observed. Application of Eq. (4.1) to the particular case of the electromigration curve shown in Figure 4.2a, for which $\alpha_T = 0.80 \times 10^{-3} \text{ K}^{-1}$ (residual resistivity ratio (RRR)=1.85), suggests that EM already starts at 100 K. Eq. (4.1) implicitly assumes that the temperature rise is rather uniform between the voltage contacts. This is justified by the fact that the width of the spatial temperature distribution, so called thermal healing length^[84], $\delta = \sqrt{\chi t / h_r} \sim 1 \mu\text{m}$ for granular Al^[85], is larger than the separation between the constriction and the voltage contacts. Still, the temperature values obtained from Eq. (4.1) represent an underestimation by about 30% of the temperature of the hottest spot along the nanowire^[36,86].

After the first EM shown in Figure 4.2a, the normal state resistance has increased by a factor of 3. Only based on transport measurements it is highly non trivial to draw any reliable conclusion concerning the effective cross section reduction of the nanoconstriction. Indeed, depending on the chosen parameters driving the electromigration, voids can develop either at the center of the bridge or along its perimeter^[60]. To that end, it is essential to carry out direct imaging of the induced damage as shown in the inset of Figure 4.2e. The $R(T)$ curve obtained in zero field condition and with an applied current $I = 100 \text{ nA}$, much smaller than the one needed to initiate the EM, reveals a superconducting transition substantially broader than the one corresponding to the virgin sample shown with a dotted line in Figure 4.2e. This has been interpreted in terms of thermally activated phase slips phenomena^[50] where $R(T) = R_0 \exp(-\Delta F / k_B T)$, with $\Delta F \propto w$ the activation energy associated to the creation of a phase slip excitation. As w decreases, so does ΔF and consequently the rate of phase slips and the associated dissipation increase. It is also worth noting that the narrowing of the constriction does not seem to produce a change in the critical temperature as could be expected from previous reports^[87]. This effect results from the fact that the voltage contacts are 500 nm apart from the constriction and therefore capture also the superconducting transition of the leads which remains unchanged after EM. Further electromigrating the sample accentuates the narrowing of the constriction and consequently increases the rate of phase slips and broadens the superconducting transition even more.

The most interesting result is summarized in the second column of Figure 4.2. Panel (b) of Figure 4.2 shows that by inverting the direction of the electromigrating current, it is possible to anti-electromigrate, i.e. to reduce the resistance as current increases. A similar effect has been reported for Au and Pd-Pt nanowires^[64]. As shown

in the inset of Figure 4.2f corresponding to the SEM image after anti-EM, the void has been refilled with material, naturally explaining the observed decrease in resistance. It is important to remark that all SEM images have been acquired *ex-situ*, which requires removing the sample from the cryostat at expenses of risking an electrostatically induced damage. Figure 4.2f confirms that a sharp superconducting transition, very close to the initial virgin sample (dotted line in Figure 4.2e), is recovered after anti-EM. An extra sequence of EM (panels (c) and (g)) followed by anti-EM (panel (d) and (h)) unambiguously shows the reversibility of this process in Al samples.

Further evidence of the controllability of the normal state resistance by alternating EM and anti-EM is shown in the inset of Figure 4.2h. Here, each resistance value achieved by EM differs from the targeted value by less than $0.25 \, \Omega$, demonstrating the fine tuning capability of the process. Considering that this process is realized in the very same sample, being reversible and with high level of control, it can be considered as an appealing approach to study the evolution of the physical properties of nanoconstrictions of different conducting materials. The question now arises as to whether Al is a particularly malleable material permitting this manipulation and if the observed behaviour can be generalized to other compounds. In the next sections we will discuss the cases of Nb and LCCO and show that there are some particularities in the electromigration process which are unique to each material.

4.2.3 Electromigration of Nb nanoconstrictions

The electromigration of Nb has not received much attention so far. The early works of Serruys^[88,89] deal with mm size samples and focus on the displacement of iron, cobalt and chromium immersed in Nb as measured by a radioactive tracer method. The electromigration force is given by Eq. 2.11, where e is the electron charge and Z^* is the effective valence of the carriers combining the effect of electron wind and direct electric force on the ions^[33,34]. As recognized by Gupta et al.^[90], the electron-wind force, responsible for electromigration, depends on an integral over the Fermi surface which is rather complicated and essentially hole-like in Nb, i.e. $Z^* > 0$. This is in contrast to Al for which $Z^* < 0$.

In Figure 4.3a we show the evolution of the resistance of a Nb constriction during the EM process. The general aspect of the curve resembles the response of Al nanoconstrictions, but a more careful analysis permits us to identify two important differences. First, the initial increase of resistance is, unlike for Al, irreversible and leading to changes in the superconducting properties of the constriction. Second, the current at which dR/dI changes polarity (threshold of severe electromigration) is not sharply defined but rather a smooth transition is observed. We estimate at about $140 \, \text{MA}/\text{cm}^2$ the threshold current density needed to start severe electromigration

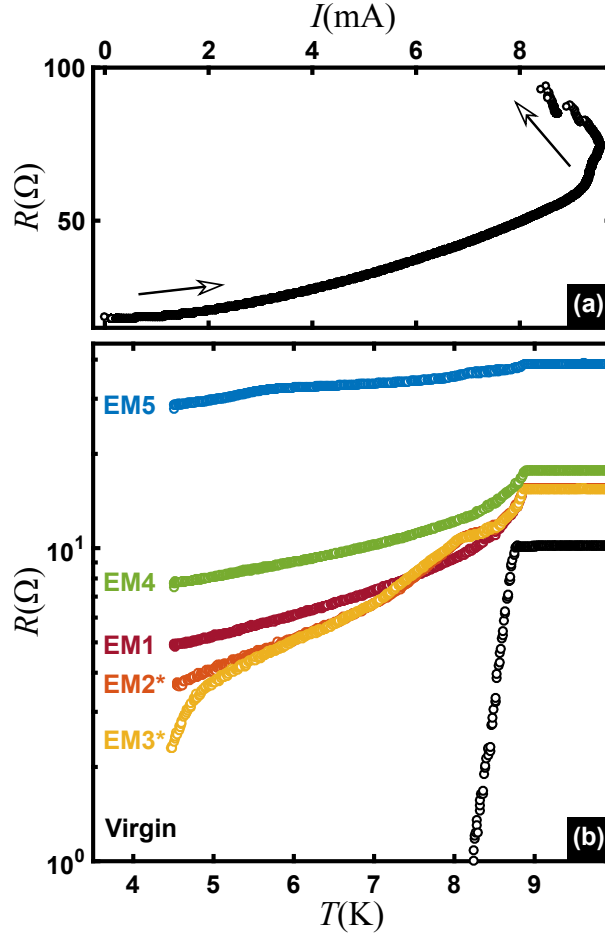


Figure 4.3: **Electromigration in Nb nanoconstrictions.** (a) Evolution of resistance as a function of current during an electromigration process. (b) Resistance vs temperature obtained at low drives ($1 \mu\text{A}$) obtained after a series of EM/anti-EM processes. Numbers indicate the chronological order. Asterisks denote anti-electromigration runs.

at a bath temperature of 10 K. From the normal state resistance we obtain a resistivity $\rho \sim 9 \mu\Omega\text{cm}$ for the Nb films at 10 K and a $\text{RRR}=3.65$ corresponding to $\alpha_T = 9.08 \times 10^{-3} \text{ K}^{-1}$. From these parameters and using Eq. (4.1) we can deduce, assuming minor changes in the structure, that the temperature at the maximum applied current is $T \sim 760 \text{ K}$. It should also be mentioned that the transport measurements in Nb have been performed in a chamber with a He pressure of 2 mbar with most of the heat removal through the substrate.

Figure 4.3b shows $R(T)$ curves obtained at low drives ($1 \mu\text{A}$) after different electromigration histories. As for Al, the onset of the superconducting transition does not

change after electromigration, indicating that this criterion denotes the transition in the electrodes rather than at the constriction. The first electromigration (EM1), obtained after applying 8.4 mA, gives rise to an increase of the normal state resistance as well as a much broader transition than the virgin sample. This effect is very similar to the Al constrictions and can thus be attributed to the enhanced effects of thermal fluctuations. Interestingly, even though this EM has been carried out at a current smaller than the one corresponding to the transition to the $dR/dI < 0$ regime, a clear change in the material properties is still observed. SEM images acquired at this stage of the process show no hint of structural damage. Starting from this point, two consecutive attempts of anti-EM (EM2 and EM3) lead to a rather weak recuperation of the superconducting state, but producing no noticeable change in the normal state resistance. Changing the polarity of electromigration back into the initial condition and always dwelling within the regime where $dR/dI > 0$, we are able to further increase the normal state resistance and widen the superconducting transition as shown in EM4. The curve EM5 results from a severe electromigration in the $dR/dI < 0$ regime.

In general, we confirm that forward electromigration in Nb seems to operate correctly whereas anti-EM produces very weak recovery of the superconducting properties. In other words, there is little influence of the current polarity into the final resistive state. This is in striking contrast to what is observed in Al. In order to understand this behavior it is necessary to recall that Nb is not in a pure state but it contains interstitial solute atoms of oxygen. De Sorbo^[91] has shown that for each 1% at. of O in Nb, the superconducting transition T_c decreases by 0.93 K and the normal state resistivity increases by $5.2 \mu\Omega \text{ cm}$. The fact that the critical temperature of our samples lies about 0.4 K below the expected value for pure Nb can be interpreted as an indication of O diffused into the structure. In Ref. 92 it was shown that O diffusion in Nb becomes important above 400 K whereas at 300 K the diffusion of O in defect-free Nb is only of 0.1 nm in three days. Considering that our rough estimate of the sample temperature at the point of starting the electromigration lies largely above 400 K and that the chamber of the cryostat is not in ultra high vacuum conditions, it is plausible that O diffusion takes place during the EM. In addition, the strain along grain boundaries and defects is known to yield an enhanced O concentration and diffusion^[93,94]. Based on this information and the presented experimental results, we envisage a scenario where EM in Nb occurs in two steps. At low currents, O atoms are subjected to migration thus leading to clear changes in the superconducting properties and the normal state resistance. In this regime, no noticeable changes of the structure are expected. At large bias currents ($dR/dI < 0$), Nb atoms can be displaced and a more conventional electromigration takes place.

Considering that a strong directional bond between Nb and O gives rise to large

binding energies above 5 eV^[95,96] it would be interesting to verify our hypothesis in an alternative system where O atoms were more susceptible to be displaced by an electron current. To that end, in the next section we focus our attention on a copper oxide superconducting compound.

4.2.4 Electromigration of LCCO microconstrictions

A pioneer investigation of electromigration of oxygen in the prototypical high critical temperature superconductor $\text{YBa}_2\text{Cu}_3\text{O}_{7-\delta}$ at 200 °C has been reported in Ref. 97. Later on, Moeckly and co-workers^[98–100] have addressed the electromigration in micron size bridges of this material at room temperature. These authors reported an improvement of the normal and superconductive properties of the microbridge, raising J_c , and lowering the normal state resistivity by up to 30% for currents below a threshold bias of about 5 MA/cm². Above this threshold the transport properties were shown to rapidly degrade. The detrimental effects were attributed to the electromigration of basal-plane oxygen and the resultant formation of inhomogeneous oxygen deficient and disordered distributions giving rise to filamentary superconducting regions of nanometer scale within a nonsuperconducting background. Interestingly, the authors also reported that moderately damaged structures may be effectively restored by subsequent application of a large dc current with the opposite polarity. In other words, similarly to the case described for Nb, the effect of EM is not to produce a morphological change but to create oxygen deficient regions.

We have extended these early investigations to a sister compound, $\text{La}_{2-x}\text{Ce}_x\text{CuO}_4$. In our case, the EM is carried out at low temperatures, allowing us to access a regime of rather cold electromigration. As shown in Figure 4.4a, the electromigration process resembles that of Nb, with an initial parabolic shape of the $R(I)$ characteristic followed by a smooth transition to the region where $dR/dI < 0$. Along the region where $dR/dI > 0$, the response is reversible as in Al. In the region of negative slope the response is irreversible although it generates no visible damage to the structure. This is shown by comparing the SEM images corresponding to the virgin sample in Figure 4.5a to that of the same sample after electromigration in the negative slope regime (see Figure 4.5b). If, however, very high current densities are applied, a clear imprint of the damage caused in the structure is observed, as indicated by the arrow in Figure 4.5c after applying 80 MA/cm². We argue that at relatively low current densities, only oxygen atoms are displaced by the electron wind, whereas at sufficiently high current densities heavier atoms are able to migrate within the unit cell. In addition, in our polycrystalline LCCO sample, highly strained grain-boundary regions may contain excess O vacancies as reported for YBCO^[101], and can further influence the change of local oxygen doping via electromigration.

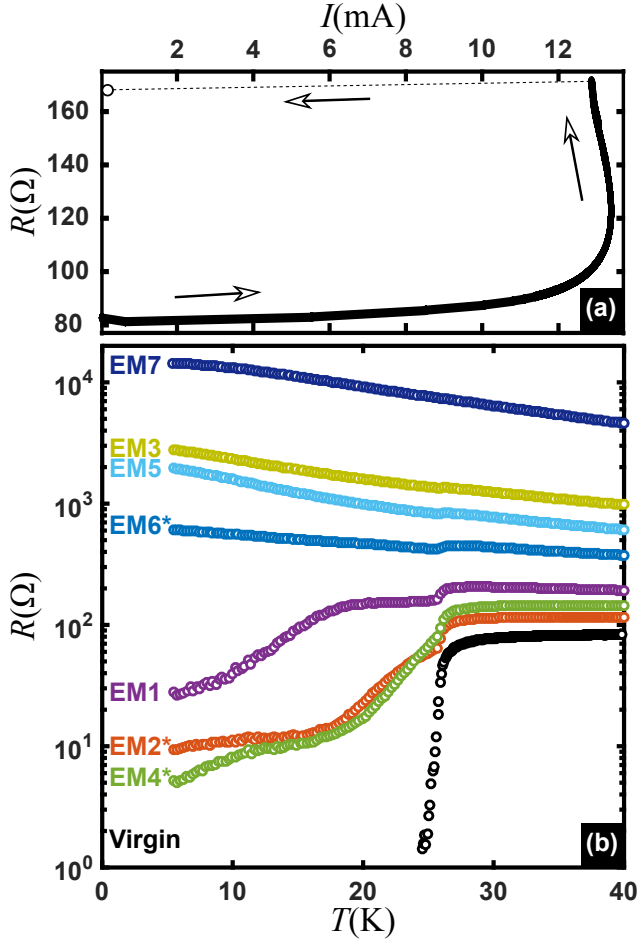


Figure 4.4: **Electromigration-healing sequences in LCCO microwires.** (a) typical $R(I)$ response during an electromigration process in LCCO at a bath temperature of 30 K. (b) Resistance versus temperature characteristics of a LCCO microbridge after successive electromigrations. Numbers indicate the chronological order. Asterisks denote anti-electromigration runs.

Evidence of the irreversible response obtained after electromigration with weak currents is shown in Figure 4.4b where the $R(T)$ characteristics obtained with a bias current $I = 1 \mu\text{A}$ are shown after successive electromigrations. The virgin sample, i.e. before electromigration, exhibits a superconducting transition at about 26 K. After the first electromigration process (EM1) the normal state resistance has been increased by 110 Ω and the superconducting transition defined at 50% criterion, has diminished by a factor of 1.7. This change can be partially healed by reversing the current direction (EM2). If the resistance of the constriction is brought above 350 Ω the superconducting transition is no longer present in the range of temperatures here

investigated. Instead, an increase of resistance with decreasing T , characteristic of an insulating state, is observed. Interestingly, the superconducting state can still be recovered by anti-EM (see curve EM4).

To our knowledge, this is the first evidence of current-driven superconductor-insulator transition (SIT) in LCCO films. In order to dig into the possible scenarios describing the mechanism behind this phenomena, let us first remind some important facts concerning these materials. The electron-doped LCCO is in the so called T' structural phase, while the hole-doped counterpart $(\text{La,Sr})_2\text{CuO}_4$ (LSCO) has a T-type structure. In the T-phase, one Cu atom and six oxygen atoms form an octahedron, whereas in the T' -phase the two apical oxygens are removed or moved to the rare-earth blocks (see Fig1 in Ref. 102). The YBCO has a T^* structure, where only one apical oxygen is detached from the octahedron. Interestingly, a T' -to-T structure transition with tuning pressure was observed in $(\text{Pr,Ce})_2\text{CuO}_4$, accompanied with a superconductor-insulator transition^[103] which might suggest that large current densities can play the same role as pressure on oxygen migration. Another plausible interpretation of the reversible SIT is that oxygen is pushed away from the original position under high current density, resulting in a gradual distortion of the lattice along the bridge. This is consistent with the increase of the residual resistivity with increasing oxygen content as reported in Ref. 102. Similar electrically driven redox reaction and the associated structural change has been observed in Ce oxides^[104]. We should also mention that the reversible change of the bridge resistance could be associated to the resistive switching observed in transition metal oxides, for which the generation of oxygen vacancies has been identified as one of the possible mechanisms. Clearly, further investigations are needed to discern which among the above listed phenomena, is the dominant one.

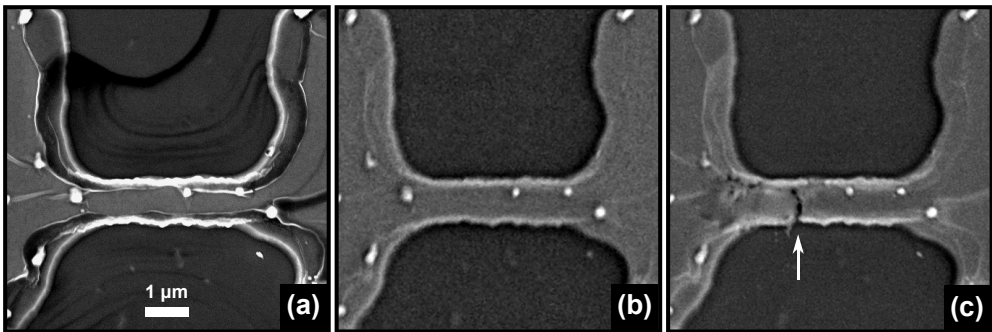


Figure 4.5: **Structural characterization of electromigration in LCCO micro-bridge.** (a) Scanning electron micrograph of virgin high- T_c microbridge. (b) Micrograph of the same bridge as in (a), taken after electromigration (EM2). (c) Very last state of the bridge taken after having applied high voltage to increase resistance until measuring current values characteristic of tunnelling.

It is worth noting that the transition point where dR/dI changes sign takes place at a critical current density of 13 MA/cm^2 when done at a bath temperature of 50 K. We estimate a resistivity $\rho \sim 150 \text{ } \mu\Omega\text{cm}$ for the LCCO films at 50 K and a $\text{RRR}=5.3$ corresponding to $\alpha_T = 17.3 \times 10^{-3} \text{ K}^{-1}$. From these parameters and using Eq. (4.1) we can estimate that the maximum temperature during the electromigration is $T \sim 70 \text{ K}$.

Finally, it is interesting to consider the possibility that the critical current density of a superconductor can exceed the density of current needed for EM. This may be achieved in high critical temperature superconductors like YBCO where $J_c \sim 3 \text{ MA/cm}^2$ at 77 K and $J_c \sim 30 \text{ MA/cm}^2$ at 10 K. Since these values of current densities lie above the current needed to migrate oxygen atoms, in case the dissipative regime of the superconductor is achieved, EM takes place and the properties of the material change irreversibly. Notice as well that if the stoichiometry of the compound is detuned by current, also the carrier density should be affected. We are not aware of studies addressing these issues.

4.2.5 Electropulsing

As we have pointed out above, severe electromigration starts at the point where dR/dI diverges, i.e. where a transition from $dR/dI > 0$ to $dR/dI < 0$ takes place. It is important to emphasize that this transition results from the reaction to the feedback signal and therefore its degree of abruptness reflects the speed with which this feedback control needs to operate. In other words, more pronounced is the curvature of the $R(I)$ at the transition, faster the feedback loop needs to react. The electromigrations performed in Nb (Figure 4.3a) and LCCO (Figure 4.4a) exhibit a rather smooth transition suggesting that the EM process corresponds to a progressive damage instead of an explosive phenomenon. This finding encouraged us to propose the simpler method of electropulsing as an alternative to achieve controlled electromigration, without the need of costly and complex feedback loops. This approach consists in applying voltage pulses of magnitude similar to that needed to reach the critical current density of the virgin structure during a short period of time. The results obtained through this technique are summarized in Figure 4.6.

The main panel of Figure 4.6 shows the evolution of the final resistance of the constriction after a series of voltage pulses of amplitude 15 V and duration 1 s. The initial resistance of the sample ($300 \text{ } \Omega$) was first increased up to $1100 \text{ } \Omega$ and subsequently reduced to its initial value by applying pulses of negative polarity. A similar procedure applied to Nb (see inset of Figure 4.6) shows an increase of the initial resistance by a factor of 7. Pulses of negative polarity in Nb lead to very weak healing effects (not shown), in agreement with the electromigration results obtained by controlled

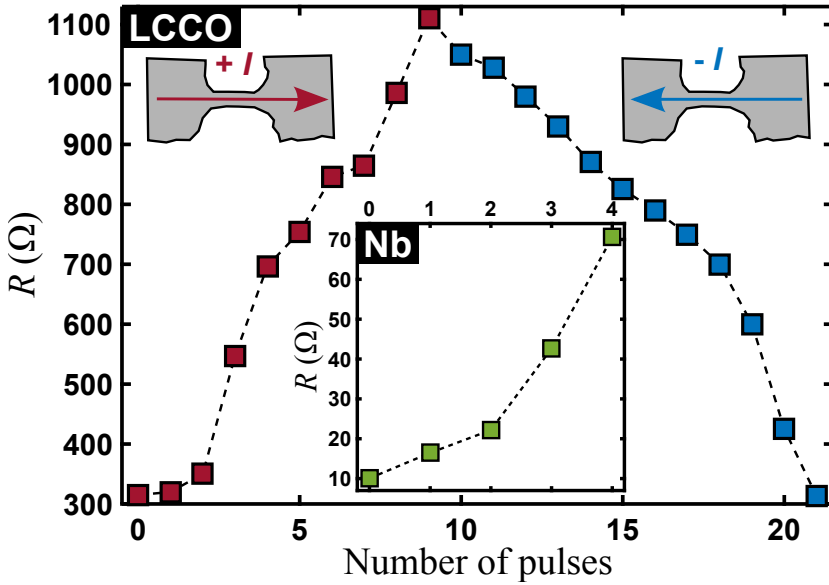


Figure 4.6: **Electro-pulsing.** Main panel: values of resistance obtained after applying voltage pulses to a LCCO microbridge. Amplitude and duration of a single pulse were respectively 15 V and 1 s. Red points are taken after pulses of same polarity, blue points are taken after pulses of reversed polarity. Inset: same as in main panel but for Nb.

feedback in this material.

We should mention that due to the rather abrupt transition observed in the electromigration curve of Al, electropulsing in this material requires a very short dwell time and very well tuned voltage pulses. Attempts of achieving electropulsing in Al with few seconds scale pulses lead to immediate irreversible damage and the creation of nm scale gaps, similar to those reported in Ref. 48,55 for Au nanowires. Note that increasing the duration of the pulse allows to increase the local temperature at the electromigrated spot, which leads to an exponential change in the probability to induce damage, as suggested by Eq. (2.20). On the other hand, increasing the amplitude of the voltage pulse increases the current density at the constriction which appears quadratically in Eq. (2.20). We have succeeded in obtaining partial EM of Al constrictions by using pulses shorter than ms scale and by varying the amplitude of the pulse.

4.3 Conclusions

In conclusion, we investigated the benefits of controlled electromigration and its healing counterpart as a knob to adjust the normal state resistance of pre-indented supercon-

ducting nanoconstrictions down to fractions of Ohms. The forward electromigration works for the three investigated superconducting materials, whereas healing effects exhibit a material dependent performance. While EM in Al always leads to structural changes at the nanoconstriction, in Nb and $\text{La}_{2-x}\text{Ce}_x\text{CuO}_4$ there is a regime at low current densities where an irreversible response is observed but without associated structural damage. We attribute this effect to the selective electromigration of oxygen atoms. We also discuss the possibility to achieve rather efficient controlled electromigration by electropulsing, which can be straightforwardly implemented without investing efforts in costly analogue feedback systems or complex software controlled feedback loops. We highlight the appealing aspect of electromigration for investigating superconducting nanoconstrictions, with the possibility to beat the state-of-the-art lithography methods complemented by the reversibility of the process. We illustrate this fact by unveiling for the first time a current induced superconductor-to-insulator transition in $\text{La}_{2-x}\text{Ce}_x\text{CuO}_4$.

Chapter 5

Transition between phase slips dominated regimes in narrowed superconducting wires

This chapter is largely based on the following works:

X. D. A. Baumans *et al.*, *Thermal and quantum depletion of superconductivity in narrow junctions created by controlled electromigration*, Nature Communications **7**, 10560 (2016).

5.1 Introduction

During the last decades, nanotechnology has set the stage for a new industrial revolution. Not only because it made possible the continuous miniaturization of larger devices, but mainly due to a plethora of unexpected emerging properties that have no bulk equivalent. When crossing over from macro, through the meso, for eventually reaching the micro-world, we can identify two main physical properties that play an increasingly important role. Firstly, surface effects arising from the increase of surface to volume ratio and the fact that surface atoms have a different coordination number than atoms in the bulk. Secondly, confinement effects, giving rise to a discretization of the electronic levels, a change of the density of states and the overall electronic properties^[105].

Superconducting materials at the nanoscale show no exceptions to this transformation. However, due to the multiple characteristic length scales of superconductivity, i.e. magnetic penetration depth λ , coherence length ξ , and Fermi wavelength λ_F , nanoscale superconductors exhibit a far richer spectrum of phenomena^[106]. More specifically, in superconducting devices with lateral dimensions ranging from 100 nanometers to a few micrometers (the so-called mesoscopic regime, size comparable to ξ and/or λ) strong confinement effects of the superconducting condensate are observed^[107]. In even smaller nanostructures, with at least one dimension comparable to λ_F , electron confinement effects come into play. As such, a profound size dependent effect is expected on the superconducting gap and the critical temperature, T_c ^[108,109].

As explained in Chapter 1, while bulk superconductivity is characterized by a macroscopic wave function for the whole Cooper pairs condensate $\psi_s(x)e^{i\varphi}$ with a well defined phase φ , in low dimensional systems the long-range order of superconducting Cooper pairs is not possible due to phase fluctuations. As a consequence, a 2D nanofilm goes through a phase transition from a superconducting state to an insulating state at low temperatures^[110]. In a 1D superconducting nanowire of cross section $S < \xi(T)^2$, phase fluctuations (PS) lead to a premature destruction of the superconducting properties^[111–114]. We saw it, these PS represent activation processes that can be triggered either thermally^[115,116] or through quantum tunneling^[111–113]. As phase fluctuations cause dissipation, their growing importance with reducing dimensions seems to settle the lower limit for developing useful superconducting devices.

Although the aforementioned mesoscopic regime has been widely explored both experimentally and theoretically, the superconducting micro-world has received much less attention. One of the main reasons for the limited amount of experimental results is the difficulty of sample fabrication, as conventional lithographic techniques are unable to reach these dimensions. As a result, researchers are exploring alternative approaches in order to develop controlled nano- and subnano-scale fabrication^[111,117–119].

One promising direction here is the use of EM. Indeed, we saw in the previous chapter that we are able to use it in a controlled way and make the most of the reversibility of the process to further decrease and accurately adjust the size/resistance of a nanowire.

In this chapter, we investigate the conditions for nucleating PS in pre-indented Al nanowires, and the transition from thermally induced to quantum driven PS as the nanowires are narrowed down via in situ controlled EM, i.e without the need to fabricate new samples. Our results are in agreement with the assumption that EM occurs at a constant power of $110 \mu\text{W}$ at the constriction, irrespective of the constriction size. We estimate that the transition from TAPS to QPS takes place at $\sqrt{S} \sim 12 \text{ nm}$, and we show that sufficiently narrow constrictions lead to a negative magneto-resistance (NMR), previously reported as a fingerprint of PS dominated dissipation^[120]. We demonstrate that this NMR arises from the suppression of the rate of activated PS, as normal quasiparticle current is injected through the leads into the constriction. For a constriction with normal resistance about twice as much as the superconducting quantum resistance, we found clear signatures of a superconducting-to-insulator transition. These findings show the possibilities of EM to create and explore superconducting devices with ultimately small dimensions^[108].

5.2 Structural characterization

The Al nanowires fabricated by electron beam lithography have a constriction in the central part (bow-tie shape) as shown in the scanning electron microscopy image of Figure 5.1a. They were defined on Si substrate ($275 \pm 25 \mu\text{m}$) covered by a resist mask (single layered, 3% PMMA 950K in chlorobenzene solvent). The Si wafer had crystal orientation $\langle 100 \rangle$, was p-doped (with Boron at concentrations $10^{16} - 5 \cdot 10^{14}$ atoms per cm^3) and has a native oxide layer (SiO_2) on top ($\sim 10 \text{ \AA}$). Subsequently, an Al thin film ($\sim 25 \text{ nm}$) was deposited using MBE with deposition rate of 1.2 \AA s^{-1} and pressure in the chamber under 10^{-8} mbar . Deposition was subsequently followed by lift-off process.

Moreover, ex-situ scanning electron microscopy images of a bow-tie sample before and after EM, Figure 5.1b, clearly show that the constriction acts as nucleation point and guarantees that the EM will be triggered in its vicinity. We have investigated several different samples, with minor adjustments on the exact geometry, and all of them exhibit a quantitative correspondence between the normal state resistance and its temperature dependence after repeated EM. Therefore, for the sake of clarity we will not explicitly indicate the sample source of each reported measurement.

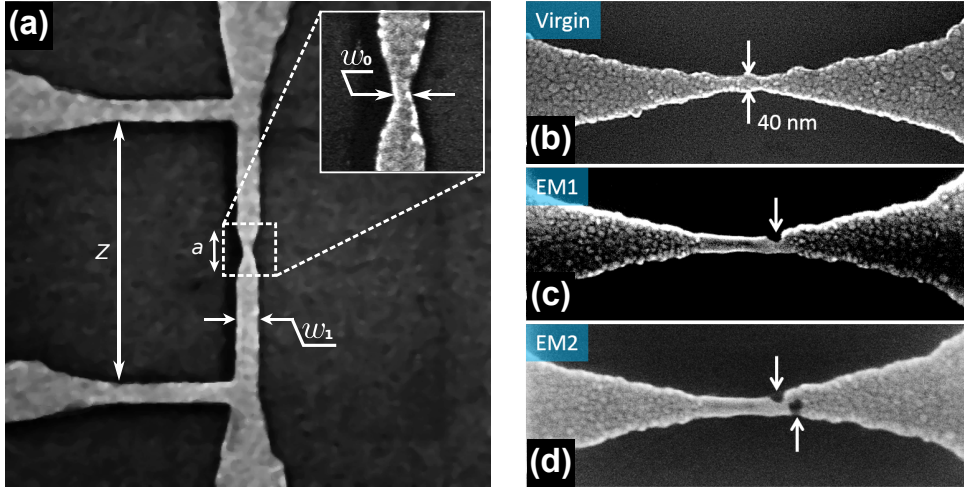


Figure 5.1: Layout of Al microbridges. (a) Representative SEM image of one of the samples investigated in this chapter, before electromigration. The bow-tie shaped bridge is a thin film made of aluminum with dimensions : $Z = 2000$ nm, $a = 400$ nm, $w_1 = 150$ nm, $w_0 = 50$ nm. Scale bar, 300 nm. (b)(c)(d) Ex-situ scanning electron micrographs of a sample illustrating the shrinking of the constriction due to subsequent electromigrations. (b) corresponds to the virgin sample with arrows indicating the approximate width. (c) and (d) represents respectively the sample after the first and the second run of electromigration with arrows pointing out the created voids in the junction.

5.3 Characterization of electromigration

The EM procedure was performed under two complementary cryogenic environments, namely a ^4He cryostat with the sample immersed in liquid He and a ^3He refrigerator with cooling achieved through a cold finger. Electromigration carried out in the former system exhibits a higher degree of control and less unexpected breakdowns. This cryostat allows temperature control down to $100 \mu\text{K}$ accuracy and has a large cooling power. Its main disadvantage lies on the relatively high base temperature of 1.1 K. EM performed in the ^3He refrigerator seems to be less stable, the cooling power is limited to $50 \mu\text{W}$ and the temperature control to 5 mK accuracy, but the system offers a much wider temperature range (base temperature of 300 mK). Throughout this chapter, measurements performed in both systems will be presented.

It is worth noting that the geometry of our sample is unambiguously known only before the first electromigration process takes place. For the bow-tie geometry used in this chapter, it is easy to derive the exact analytical formula for the resistance of the structure,

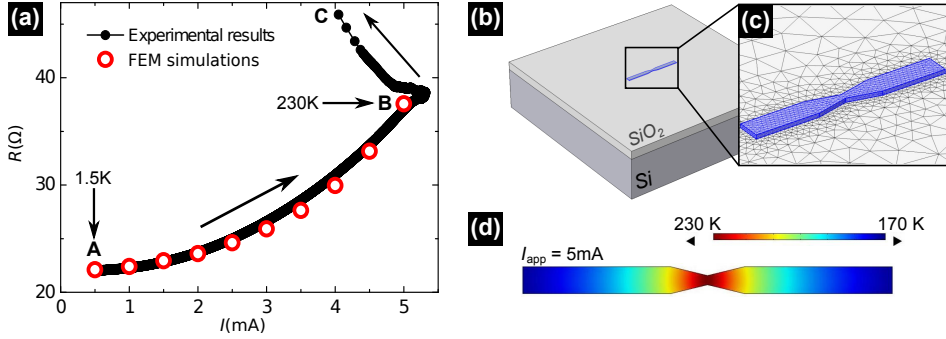


Figure 5.2: Inhomogeneous temperature distribution along the Al bridge before electromigration. (a) Non-monotonous resistance rise as a function of current during the first electromigration process. The solid black symbols represent the experimental data and open red dots are FEM simulations for a temperature coefficient of resistance given by $\alpha_T = 3.6 \cdot 10^{-3} \text{ K}^{-1}$. Large black arrows indicate the temporal evolution of the acquired experimental data. Small arrows indicate the temperature of the junction at two points: at the beginning of the measurement (A) and at the onset of electromigration (B). (b) Al transport bridge on Si/SiO₂ substrate immersed in liquid helium considered for FEM simulations. The sample dimensions are the same as for the real sample shown in Figure 5.1 and the thickness of the SiO₂ was taken as 100 nm. (c) Layout of the grid used for FEM simulations. (d) Simulated temperature profile of the bridge for an applied current of 5 mA.

$$R = \frac{\rho}{t} \left[\frac{a}{w_1 - w_0} \ln \left(\frac{w_1}{w_0} \right) + \frac{Z - a}{w_1} \right], \quad (5.1)$$

where ρ is the thin film resistivity of Al, t is the thickness of the film, w_0 is the width of the bridge at its narrowest point, w_1 is the width of the bridge at its largest point, a is the length of the bridge where the cross section increases, and Z represents the total length of the bridge (see Figure 5.1a). From this dependency, and knowing the exact geometry of our samples as well as their normal state resistance $R_n = R(T > T_c)$, we can estimate the resistivity of the Al bridges as $\rho(1.5\text{K}) = 5 \pm 1 \mu\Omega \text{ cm}$. Using the relation $\rho\ell = 4 \cdot 10^{-6} \mu\Omega \text{ cm}^2$ valid for thin Al films^[121], we obtain an electronic mean free path $\ell = 8 \text{ nm}$, i.e. substantially smaller than any initial dimension of the bridge. We should point out that differences up to a factor of 4 in $\rho\ell$ for polycrystalline samples were reported^[122], meaning that the mean free path here estimated does not represent an accurate value but merely an order of magnitude. Nevertheless, the obtained mean free path is consistent with the rather small $\text{RRR} = R(300 \text{ K})/R(4.2 \text{ K}) \sim 1.85 \pm 0.05$, which indicates that our system falls in the diffusive transport regime.

In Figure 5.2a, we show the resistance change observed during the first electromigration process (solid black symbols) in the ⁴He cryostat. The initial parabolic

increase of resistance when increasing current results from a combination of two phenomena, (i) an inhomogeneous Joule heating and the consequent temperature rise, and (ii) a temperature dependent resistance. In other words, between points *A* and *B* in Figure 5.2a, the $R(I)$ curve does not follow an isothermal line, even if the sample is immersed in superfluid ^4He . Furthermore, along this segment there is no electromigration, i.e. no change of the initial geometrical shape, in agreement with the reversible response observed when decreasing the current from any point in this region.

We can gain further insight about the initial virgin branch of the $R(I)$ curve by performing Finite Element Method simulations using the commercial software COMSOL^[123] to model temperature fields and corresponding resistance of the nanowires. An electrical current density was simulated through the wire, substrate was considered electrically insulating. The layout of the modelled system, depicted in Figure 5.2b, consists of a transport bridge lying on top of a SiO_2/Si substrate all immersed in liquid helium at $T = 1.5$ K. It has the exact same geometry as the experimentally measured one but without voltage contacts. The discrete grid of nodes with variable spatial density used for the FEM simulations is illustrated in Figure 5.2c. The electrical resistivity of aluminum was chosen to be $3.6 \mu\Omega \text{ cm}$. The thermal conductivity for aluminum, Si and SiO_2 were assigned to $160 \text{ W m}^{-1} \text{ K}^{-1}$, $130 \text{ W m}^{-1} \text{ K}^{-1}$, $1.4 \text{ W m}^{-1} \text{ K}^{-1}$, respectively. Heat transfer coefficient for convective cooling had a value of $30.000 \text{ W m}^{-2} \text{ K}^{-1}$.

The simulated Al sample has a temperature dependent resistivity given by the first order Taylor expansion $\rho(T) = \rho(1.5\text{K}) [1 + \alpha_T(T - 1.5 \text{ K})]$ with $\rho(1.5 \text{ K})$ and $\alpha_T = d\rho/dT (= 3.6 \cdot 10^{-3} \text{ K}^{-1})$ obtained experimentally. The results of the simulations shown by open symbols in Figure 5.2a nicely reproduce the $R(I)$ dependence followed by the experimental data. The small discrepancy between the experimental data and the numerical estimates most likely results from the assumption of a constant α_T . Moreover, the simulations allow us to obtain an estimate of the temperature along the parabolic segment *A* – *B*. In Figure 5.2d, we show the temperature distribution along the transport bridge for $I = 5 \text{ mA}$, i.e. just before starting the electromigration, indicated by point *B*. At this current value the temperature is as high as 230 K at the constriction. It is interesting to compare this value with previous reports. Indeed, Esen *et al.*^[40] estimated experimentally the temperature of the constriction during electromigration between 145 K and 290 K. Independently, Trouwborst *et al.*^[43] obtained a $T = 400 \text{ K}$ for the breaking process claiming that this value is rather independent of the temperature of the sample environment.

From point *B* till point *C* in Figure 5.2a, a continuous electromigration occurs, as evidenced by a decrease of the current in the feedback circuit with a consequent increase of sample resistance. From the moment that the first electromigration occurs

the curve becomes irreversible and it is no longer possible to be certain about the geometry of the constriction. We have found that all the $B-C$ segments corresponding to experimental data where EM is occurring, follow the very same law $R \approx P_c/I^2$ from which a constant power of $110 \mu\text{W}$ was deduced. This value is similar to that previously reported in the literature for Au structures^[41].

5.3.1 TPS to QPS transition for electromigrated constrictions

Let us now investigate the evolution of the superconducting state in the electromigrated nanowires. More precisely, in this section we will study the development of phase fluctuations in constrictions with cross sections controlled by EM.

Figure 5.3a shows the superconductor-normal metal phase boundary determined by a criterion of $0.9R_N$ for a virgin sample down to 300 mK and for magnetic fields applied perpendicularly to the plane of the sample. The inset in this panel shows the high temperature part of $H-T$ phase boundary for a virgin sample and for the same sample after 16 electromigrations. It is interesting to note that besides a vertical shift towards lower T_{c0} caused by the broadening of the $R(T)$ in the EM sample, both phase transition lines are very similar. These lines do not follow the linear phase boundary expected for an Al plain film (black line in the inset of Figure 5.3a) but rather exhibit a parabolic dependence characteristic of small dimension bridges ($w < \xi(T)$) given by^[107,124,125],

$$\frac{T_c(H)}{T_{c0}} = 1 - \frac{\pi^2}{3} \frac{w^2 \xi_0^2 (\mu_0 H)^2}{\Phi_0^2}. \quad (5.2)$$

The fact that the phase boundaries before and after EM do not show significant differences suggests that the constriction has little influence on the nucleation of superconductivity, which probably takes place first along the leads. Based on this consideration, it is reasonable to take $w = w_1$ in Eq.2, which gives a value for the superconducting coherence length of $\xi(0) = 85 \pm 5$ nm. This value is substantially smaller than the Pippard coherence length ($\xi_0 \approx 1600$ nm) thus indicating that our nanostructured superconductor falls in the dirty limit. In this case, $\xi(0) = 0.855(\xi_0 \ell)^{1/2}$ and we can estimate $\ell \approx 6$ nm which is consistent with the value obtained from the normal state resistivity value.

As anticipated above, the shifting of the phase boundary after EM arises from a broadening of the superconductor-normal transition. This is more apparent in Figure 5.3b which shows $R(T)$ curves after subsequent electromigrations. It is evident from this figure that after EM, (i) the normal state resistance increases as a consequence of the cross section reduction of the constriction, and (ii) the superconducting transition broadens.

There are several sources of $R(T)$ broadening that should be considered separately

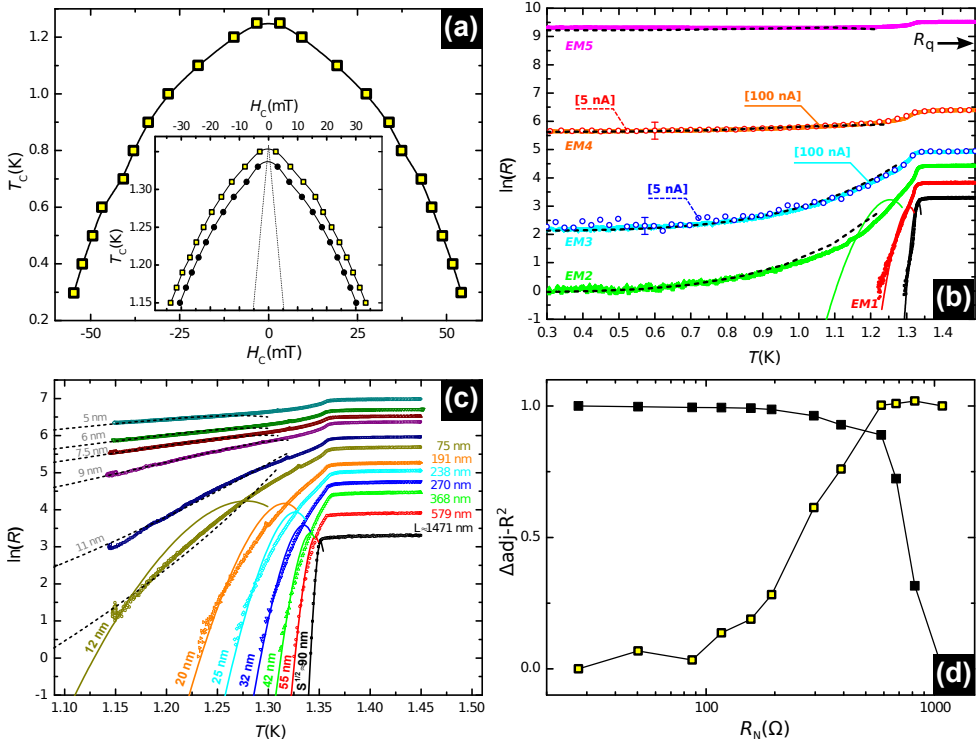


Figure 5.3: Transition from thermal to quantum PS. (a) Phase boundaries of the virgin sample. Inset: comparison of the phase boundary before (yellow squares) and after 16 runs of electromigration (black circles). The dotted line indicates the expected phase boundaries for bulk aluminum. (b) Logarithm of the resistance as function of temperature after several electromigrations. The same curves are obtained for $I = 100$ nA (continuous) as for $I = 5$ nA (circles). For the sake of clarity, the curves taken at 5 nA show a limited amount of points. The error bars represent the standard deviation around the mean value obtained by averaging 200 data points. Black arrow indicates the position of the superconducting quantum resistance, R_q . (c) All the successive $R(T)$ curves after each run of electromigration. The cross section of the constriction (S) and the length (L) after each electromigration are obtained as adjusting parameters of the model. In panels (b) and (c), the continuous lines are fits using Eq.3 for TAPS. The dashed lines are fits by the GZ model for QPS. (d) Normalized adjusted- R^2 (goodness of fit parameter), as a function of the resistance in the normal state. Black squares represent the fits using TAPS while yellow squares denote the fits using QPS.

and in detail. First of all, the widening could result from the fact that a too high current has been used during the measurements. Therefore, as the constriction shrinks, for the same applied current, the current density increases after each EM and so does the dissipation^[126]. In order to rule out this possibility, we have also acquired $R(T)$ curves for much smaller current values. In Figure 5.3b, we plot an example of two $R(T)$ curves measured after electromigrations, for alternating current $I = 5$ nA (open

symbols) and $I = 100$ nA (solid symbols). It can be clearly seen that decreasing the current has no major effect besides increasing the noise of the measured curve which is indicated by an error bar in Figure 5.3b. Another possible cause of transition broadening could be the local heating at the constriction. This effect can also be disregarded based on the current independent result shown in Figure 5.3b.

It has been recently recognized by Zgirski *et al.*^[87] that inhomogeneities along the nanowire might lead to broad superconducting transitions. In our particular case, the bow-tie bridge could be regarded as inhomogeneous in width. However, the $R(T)$ transition at zero magnetic field for the virgin sample is rather abrupt (~ 50 mK). In addition, since thinning the superconductor leads to a reduction of the effective mean free path which in turn results in an increase of T_c , we expect a broadening caused by an increase of T_c ^[87]. This is clearly not the case, since we observe the same T_c irrespective of the size of the constriction. Moreover, inhomogeneities along the wire cannot explain a finite dissipation below $T_c^{bulk} = 1.1$ K, as already suggested by Zgirski *et al.*^[87].

A more plausible explanation for the $R(T)$ broadening is the excitation of PS at the constriction. Indeed, as originally proposed by Langer and Ambegaokar^[115], the phase of the superconducting order parameter can slip by 2π generating a normal region of core size ξ which gives rise to an excess of quasiparticles in a larger scale $2\Lambda_Q \gg \xi$, known as charge-imbalance length^[115]. When the triggering of PS is thermally activated (TAPS)^[115,116], resistance can be described by Eq. (1.39) following the LAMH theory with the energy barrier for PS obeying Eq. (1.35) where $H_c^2(T)$ is the thermodynamic critical field and $\xi(T)$ is the coherence length. After each electromigration, the cross section of the constriction, S , and as a consequence the barrier ΔF , are reduced, thus increasing the frequency of nucleation of PS.

In Figure 5.3c we have made an attempt to fit all the $R(T)$ transitions at high temperatures by only adjusting the parameters S and L which are explicitly indicated in the figure. The fitting is relatively good for the low temperature part of the curves, but only for the first six electromigrations. The model clearly fails to follow the progressive change of concavity of the $R(T)$'s for the subsequent EM. This effect is captured by the parameter normalized adjusted- R^2 representing the goodness of fit, as shown in Figure 5.3d with square black symbols. A similar procedure was used to fit the $R(T)$ curves shown in Figure 5.3b covering a much wider temperature range. Here also the TPS model only accounts for the fast drop of resistance with decreasing temperature for curves with low normal state resistance, i.e. wide constrictions.

A simpler alternative to the LAMH model (Eq.3) with a temperature independent pre-factor has been proposed by Bezryadin and co-workers in Ref. 127. Following this approach does not change significantly the value of the effective cross sections deduced from the fitting. It has been also proposed by Newbower *et al.*^[128] to take

into account the parallel conduction channel provided by normal quasiparticles near T_c . By including this model, we did not note significant improvements in the fittings or changes for the values of S and L .

In Chapter 1, we explained that the observed breakdown of the TAPS model can come naturally from the fact that once the barrier ΔF has been sufficiently reduced, tunnelling is the most likely to happen. We saw that GZ predicted a temperature dependence of the resistance given by Eq. (1.41)^[112]. In this formula, all values are known except A and L .

In Figure 5.3b-c we showed with dashed black lines the fitting corresponding to the QPS model using as free parameters: A and L . We can clearly see that the QPS fit works well where the TAPS model fails. This is also reflected in the goodness of fit parameter shown in Figure 5.3d with yellow squares. From these fits, values of $L \approx 85 \pm 10$ nm and $A \approx 1.1 \pm 0.1$ are obtained. By using alternative formulas, one coming from a heuristic argument from Giordano^[129] echoed, among others, by Lau *et al.*^[113] and Altomare *et al.*^[130] and the other used by Bae *et al.*^[127], we obtained very similar results. The disadvantage of these approaches is that they contain two additional numerical fitting constants.

As a warning note we would like to emphasize that the presented analysis should be regarded as purely qualitative though clearly suggesting that a transition from thermal to quantum excitation of PS at the nanoconstriction takes place. Although the S values obtained from the TAPS fitting should be taken with precaution and are only given (as well as L) for \sqrt{S} values higher than ~ 12 nm, since the model clearly fails to adjust the tendency from and below that value. It is remarkable that this transition value is in good agreement with those previously reported in the literature. Zgirski *et al.* estimate a crossover at $\sqrt{S} \leq 20$ nm for the appearance of QPS^[126] whereas Bezryadin *et al.*^[111] reported $\sqrt{S} \leq 10$ nm. The values of \sqrt{S} in light grey given for the high resistance curves in Figure 5.3c are indicative as they were extrapolated from the previous values of S as a function of R_N . Indeed, $S(R_N)$ plot in logarithmic scales has been found to be clearly linear.

Another important evidence for the presence of PS comes from the development of a NMR effect as shown in Figure 5.4a. Indeed, it has been shown experimentally and modelled theoretically that the presence of PS (TAPS or QPS) in superconducting nanowires leads to an unusual NMR for sufficiently narrow bridges. As today, the origin of this effect is not yet fully understood. A possible mechanism could be the suppression of the rate of activated PS as a consequence of the decrease of the charge imbalance length A_Q with magnetic field^[131–135].

An alternative proposed model suggests that the NMR arises from the suppression of superconductivity in the leads. This effect causes an increase of the normal component of the current (I_n) running through the bridge and consequently a decrease

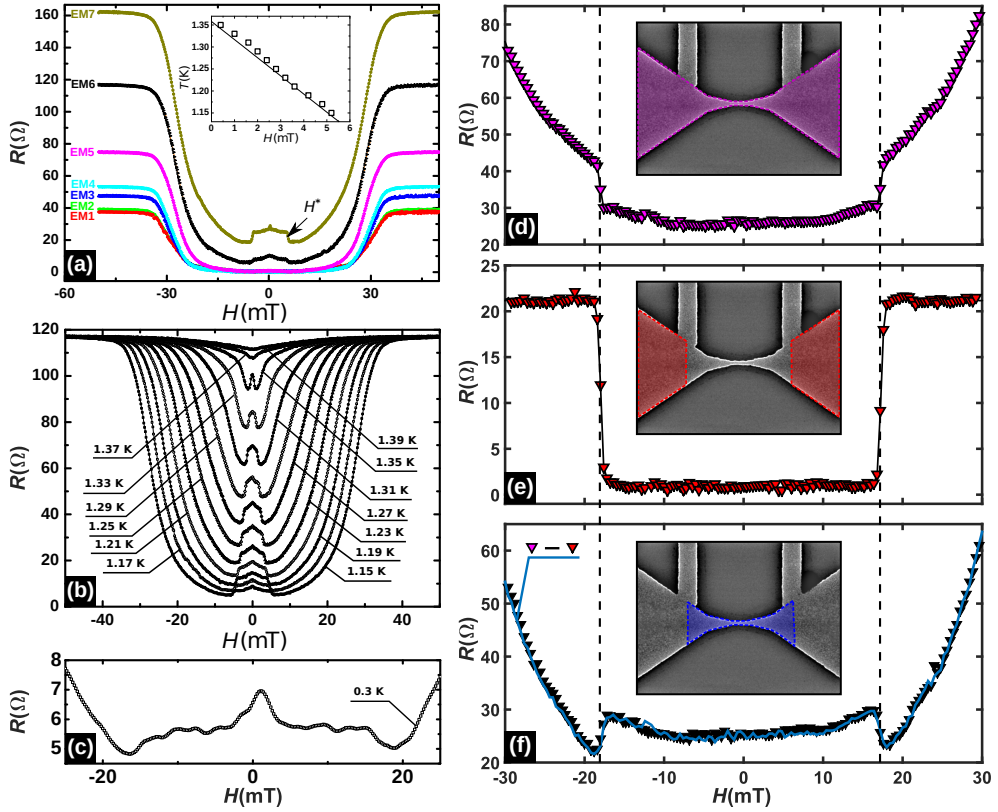


Figure 5.4: Negative Magneto-Resistance. (a) Resistance as function of applied magnetic field at 1.15 K, for one single sample after each run of EM. The inset shows the position of the NMR transition, H^* , as a function of temperature (black empty squares). The black line corresponds to H_{c2} of the contact leads. (b) Resistance as function of applied magnetic field at different temperatures between 1.15 K and 1.39 K increasing by steps of 0.02 K. These multiple $R(B)$ curves were taken just after the black curve (EM6) of panel (a). Panel (c) illustrates the persistence of the NMR effect down to 300 mK, where the electric response is dominated by QPS. Panels (d), (e), (f) correspond to the magneto-resistance of a full sample (constriction + leads), only the leads and the constriction alone, respectively.

of the rate of appearance of PS (triggered by the superconducting current I_s)^[131]. This second mechanism would lead to the observed sharp transition (corresponding to the destruction of superconductivity by the applied magnetic field in the leads). If this were the case, the limit of the NMR should coincide with the position of H_{c2} of the plain film. In Figure 5.4b we show the evolution of the plateau as a function of temperature and in the inset of Figure 5.4a, we show the position of the NMR transition (with a 50% criterion) compared to the phase boundaries obtained for the Al leads. The clear correspondence between destruction of superconductivity in the leads on the one hand, and NMR transition on the other hand, seems to reinforce

this interpretation^[120]. Let us note also that this interpretation is consistent with our sample dimensions, considering that the value of the charge imbalance length (Λ_Q) in aluminum is situated around few μm ^[136–138]. Figure 5.4c shows the presence of the NMR at the lowest accessible temperature, in the regime dominated by the QPS.

A compelling evidence is given by a set of measurements furnished in the right column of Figure 5.4. Figure 5.4d corresponds to a two-point measurement of the whole sample, thus a combined magneto-resistive response of the central constriction and the leads. Figure 5.4e shows the response of the leads only (three-point) while Figure 5.4f is the signal given by the constriction alone (four-point), exhibiting the characteristic plateau of the NMR response. We see directly that the position of the jump in resistance in Figure 5.4e (destruction of superconductivity in the leads) perfectly matches the one of the plateau in Figure 5.4f and to a lesser extent the one of the jump in Figure 5.4d. Moreover, the blue curve, corresponding to the mathematical subtraction between the purple (full signal) and the red curve (leads' signal), fit perfectly with the experimental signal coming from the constriction in Figure 5.4f.

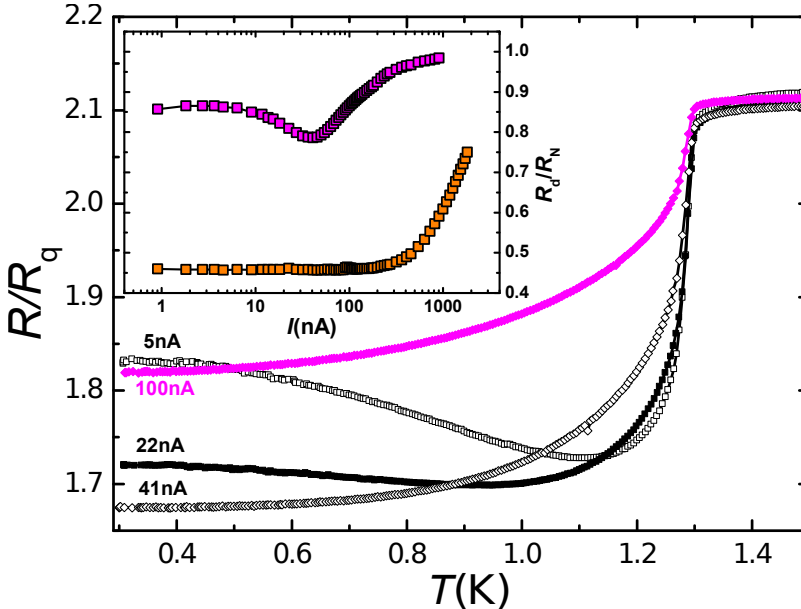


Figure 5.5: Superconducting to insulator transition. Resistance vs temperature at different currents for a constriction with $R_N > R_q$. At low currents and temperatures, $dR/dT < 0$ is characteristic of an insulating state. The inset shows that for $R_N \ll R_q$ (orange squares), the differential resistance is rather independent of the applied current, whereas for $R_N > R_q$ (purple squares), the differential resistance maximizes at zero bias. Measurements presented in the inset were taken at a temperature of 300 mK.

The measurements performed in a sample with $R_N > R_q$ unveiled further interesting results. Indeed, once the normal state resistance of the electromigrated sample increases above the quantum resistance (indicated by a black arrow in the Figure 5.3b), the adjustment with the QPS model no longer reproduced the $R(T)$ shape at low temperatures. This behavior, similar to a superconductor-insulator transition, has been already reported in ultra thin nanowires by Bezryadin *et al.*^[111] and attributed to a quantum dissipative phase transition (DPT)^[139,140] analogous to the Schmid phase transition^[141] observed earlier in Josephson junctions^[142]. Notice that, as mentioned in^[112], DPT can be observed only provided that QPS are easily created at the constriction. Furthermore, unlike the superconducting state where dR/dT is always positive irrespective of the current value or temperature, the insulating phase is characterized by a negative dR/dT at low temperatures, as shown in Figure 5.5 for the lowest values of the applied current. In addition, a differential resistance $R_d = dV/dI$ decreasing with increasing current, as shown in the inset of Figure 5.5, represents also a signature of superconductor to insulator transition. Curves in this inset correspond to measurements done after EM4 and EM5 on the sample of Figure 5.3b, as it is highlighted by the corresponding colours.

5.4 Conclusions

We have proposed a new approach to further push the limit of conventional lithography techniques. The phenomenon of electromigration has been used to gradually reduce the size of aluminum transport nanobridges. We have shown that, even at the lowest achievable temperature, there is a clear residual resistive response when the size is sufficiently reduced. We have thus been able to estimate the cross-section where the transition from TAPS to QPS occurs ($\sqrt{S} \sim 12$ nm). Another evidence of PS is the observed NMR, for which we have been able to furnish a convincing explanation. It is indeed now clear that this NMR is linked to the destruction of superconductivity in the leads of the junction. Finally, electromigration has allowed us to reach ultimately small dimensions (conductance quantum) and to unveil another exotic phenomenon, namely the superconductor-to-insulator transition. These findings reveal perspectives of the proposed fabrication method for exploring various fascinating superconducting phenomena in atomic-size contacts.

Chapter 6

Localized phase slips statistics in narrowed superconducting junctions

This chapter is largely based on the following works:

X. D. A. Baumans *et al.*, *Statistics of localized phase slips in tunable width planar point contacts*, Scientific Reports **7**, 44569 (2017).

6.1 Introduction

Small physical systems behave differently than their bulk counterparts partly due to the increased effect of fluctuations at low dimensions. In the extreme case of one-dimensional structures, long-range order and phase transitions may even be fully suppressed^[143,144]. Superconducting systems, where the long-range correlation is given by the phase coherence of the entire condensate, are no exception in this respect. Indeed, in a superconducting nanowire with cross section $S < \xi$, where ξ is the superconducting coherence length, phase fluctuations (PS) of 2π multiples prevent the formation of persistent currents.

The life cycle of a PS consists of a transformation of all the supercurrent (i.e. charge carriers are Cooper pairs) into normal current (i.e. charge carriers are quasiparticles), thus leading to power dissipation. If heat removal is very efficient or if the nanowire's specific heat is large, the temperature rise at the core of the PS is insignificant and these phase fluctuations can be considered as having a negligible time-correlation, i.e. the development of one event at a time t does not favor a second event at the same spot at a later time $t' > t$. For a sufficiently large current, the height of the effective barrier approaches zero, and a series of PS events regularly spaced in time is triggered thus leading to the formation of a persistent voltage step $V < R_N I$, where R_N is the normal state resistance of the nanowire. In long nanowires, where several PS can coexist, as I is further increased, the appearance of a new PS is accompanied by an additional voltage step.^[145]

Real systems possess certain thermal inertia implying a finite lifetime $\tau_{PS} \sim 0.1$ ns of the footprints left by a PS. This lifetime is linked to the heat diffusion time, which is substantially longer than the order parameter variation and the quasiparticle thermalization time τ_E ^[37]. Giving the fact that depleting the order parameter at an already weakened position is energetically favorable, inefficient heat removal brings about time-correlation between consecutive events. Once the mean delay between consecutive PS events becomes shorter than τ_{PS} , a cumulative heating occurs. As a result, an avalanche of events is triggered leading to a noticeable increase of the local temperature at the constriction, known as hot spot. The most prominent consequence of this effect is a sudden transition to the normal state ($V = R_N I$) allowing one to define a switching current I_{sw} as the current at which the dissipationless state is lost and which is typically determined by a predefined voltage criterion.

Due to the randomness of the activation processes, I_{sw} exhibits a statistical distribution with mean value $\langle I_{sw} \rangle$ and standard deviation σ depending on τ_{PS} . If heat removal is absent ($\tau_{PS} \rightarrow \infty$), it may happen that a single event is able to trigger a thermal runaway. In this case the width of the distribution reflects the stochasticity of individual events. In the opposite scenario of very efficient heat removal ($\tau_{PS} \rightarrow 0$),

a detectable voltage jump is only possible after a train of closely packed events. Now, the switching current approaches the critical current of the nanowire (i.e. the depairing current) and the width of the distribution tends to zero. An in-depth theoretical analysis of this phenomenon for the case of long nanowires has been reported in Ref. 17,146 and for Josephson junctions in Ref. 147. Besides the time scales imposed by the rate of PS events Γ , and the heat evacuation time τ_{PS} , there is also an additional time scale imposed by the sweeping rate of applied current. If we were able to ramp up the current with an infinite rate, i.e. much faster than the attempt frequency of single events, we should also attain the critical current of the system^[118]. In this limit, of course, the information concerning the activation mechanism is lost. In contrast to that, the statistical distribution of I_{sw} at finite sweep rates encodes information about the main physical mechanism triggering the events and whether it is of quantum or of thermal origin.

Thus far, most of the investigations have focussed on long nanowires^[117,130] where the loci of the events along the nanowire are undetermined, or on short suspended nanowires with poor heat removal conditions^[111,148,149] where single PS events may have more dramatic consequences. In the present report, we explore the opposite situation of a point contact between two Al superconducting banks forcing the appearance of PS to be highly localized in space. In addition, with the Al film being deposited on a Si/SiO₂ single crystal wafer, heat removal is rather efficient. The possibility to narrow down the size of the constriction in situ through controlled migration of atoms, allows us to switch, on the very same sample, between strong and weak self-heating regimes after the switching process. Furthermore, an analysis of the statistical distribution of I_{sw} for different temperatures reveals that the main dissipative mechanism can be ascribed to a train of thermally driven PS events. The physics addressed in the present chapter might provide a new approach for understanding the statistics of flux avalanche triggering of thermomagnetic origin in thin superconducting films or the escape distribution for magnetization reversal in small particles, although sampling events distribution might be harder in these systems.

6.2 Evidence of weak to strong self-heating transition

Scanning electron micrographs showing the sample layout are presented in Figure 6.1(a-c) for three different magnifications covering two orders of magnitude on the spatial scale. The Al nanowires were defined by Electron Beam Lithography (EBL) on Si/SiO₂ substrate ($750 \pm 50 \mu\text{m}$ Si, $300 \pm 25 \text{ nm}$ SiO₂) covered by a resist mask (double layered, PMMA 950K, 3.5% solid content in ethyl lactate solvent + PMMA/MA 33%, 4% solid content in methoxy propanol solvent, $150 \text{ nm} + 200 \text{ nm}$), using nanofabrication system from Raith GmbH. The Si wafer had crystal orientation (100). Subsequently,

an Al thin film (~ 25 nm) was deposited using Molecular Beam Epitaxy (MBE) with deposition rate of 1 \AA s^{-1} and pressure in the chamber under 10^{-8} mbar. The deposition was followed by a lift-off process. The 25 nm thick Al film shows a clear contrast with respect to the substrate. Current-carrying wires can be readily identified since they are wider than the voltage probes. The granular structure of the Al film is visible in the highest magnification image, Figure 6.1(c) and in the inset of Figure 6.1(d) evidencing the polycrystallinity of the Al film. The probability distribution of grain size is shown in the main panel of Figure 6.1(d) with a log-normal fitting. Note that the starting size of the constriction is larger than mean grain size. The rather sharp decrease of the nanowire's width following a nearly hyperbolic shape ensures high probability that PS will be localized in between the voltage probes due to the fact that the number of PS events decreases exponentially as the wire cross section increases.

The samples are highly sensitive to electrostatic discharges and special care has to be taken during bonding, transport, installation and testing (see Chapter 3). Measurements were conducted in two ^3He cryostats with 300 mK base temperature with proper high-frequency noise filtering, as described in the Chapter 3. The matching of results from both cryostats is almost perfect. A preliminary investigation of the temperature dependence of the resistance, giving evidence of the transition from thermally driven to quantum excited PSs when shrinking the constriction below a critical size ~ 12 nm via electromigration (EM), has been reported in Ref. 50. The present chapter focusses on the analysis of the stochastic nature of PS processes and the influence of thermal removal efficiency at the constrictions. We have investigated several samples, with minor adjustments to the exact geometry, and all of them exhibit qualitatively similar results. For the sake of clarity we will report here the results obtained on three of those samples labelled as S1, S2 and S3.

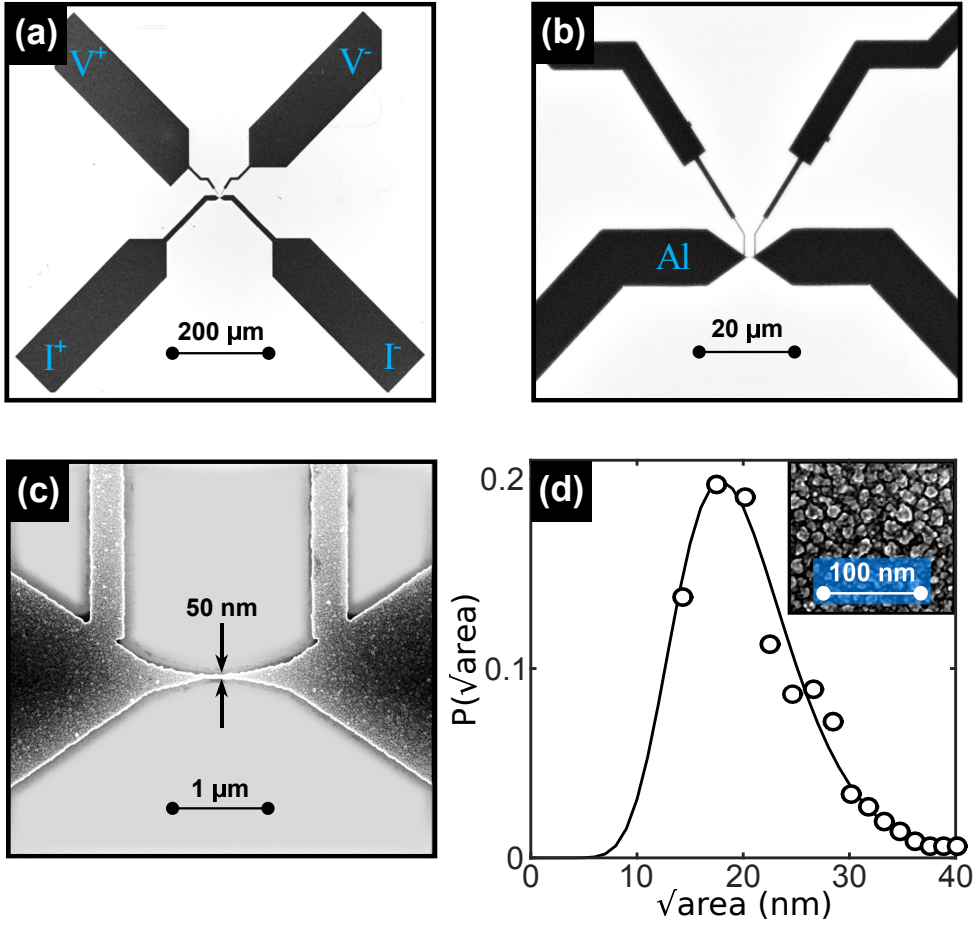


Figure 6.1: **Sample layout.** (a-c) Scanning electron microscopy images of the investigated samples obtained for three different magnifications covering two orders of magnitude on the spatial scale. V^+ and V^- marks on panel (a) denotes the voltage pads with associated polarity, while I^+ and I^- denotes the pads used to inject current. (d) Probability distribution of the grain size displayed with a log-normal fitting. The inset shows a scanning electron microscopy image of the Al surface close to the constriction evidencing the polycrystallinity of the material.

A typical set of voltage-current ($V - I$) characteristics obtained in current driven DC mode for several temperatures and at zero applied magnetic field, are shown in Figure 6.2(a). The low temperature response exhibits an abrupt transition from the superconducting state at low bias currents to the normal state at certain switching current $I_{\text{sw}}(T)$. At this current, the lifetime of the PS footprints becomes longer than the time elapsed between consecutive PS events and a cumulative heating load triggers the transition to the normal state. In other words, the PS is a precursor of a hot spot and therefore, the temperature at the constriction undergoes a strong

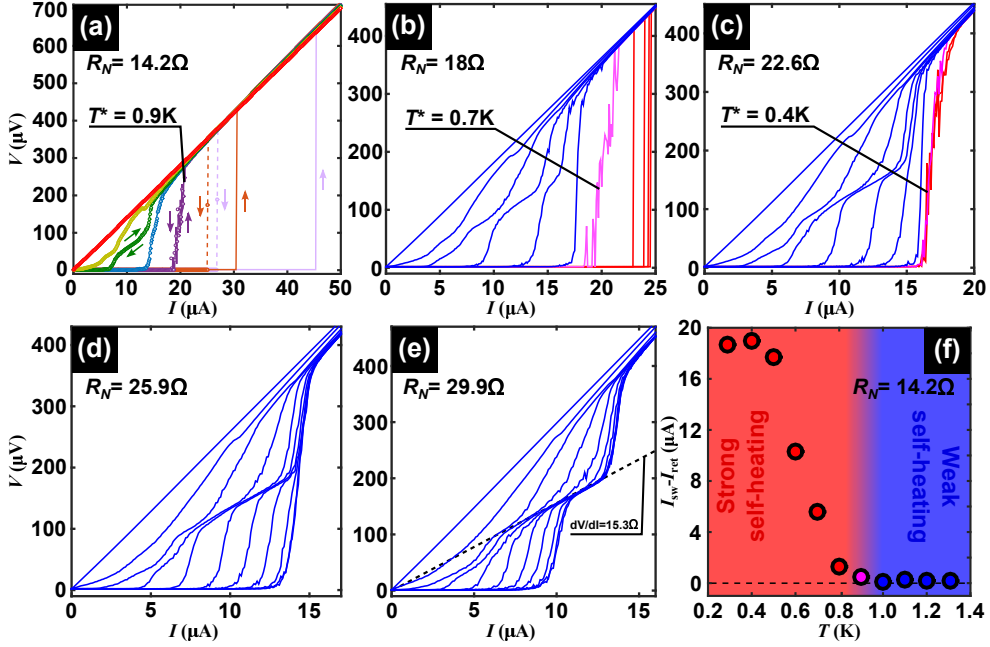


Figure 6.2: **Voltage-current characteristics demonstrating a weak-to-strong self-heating transition.** Panels (a)-(e) show DC current-voltage characteristics for several temperatures ranging from 1.3 K (leftmost curve) to 0.3 K (rightmost curve) with a step of 100 mK for sample S1. For clarity, only curves taken at temperatures of 1.3 K, 1.2 K, 1.1 K, 1 K, 0.9 K, 0.7 K and 0.3 K have been shown in panel (a). Panel (a) corresponds to the virgin sample whereas panels (b) to (e) correspond to the same sample after consecutive reduction of the constriction size via electromigration (as evidenced by the normal state resistance R_N). Abrupt jumps of the voltage at low temperatures are indicative of self-heating effects, whereas intermediate voltage plateaus develop in a more isothermal regime (i.e. low self-heating). The transition between both regimes is characterized by a noisy response (magenta line) taking place at a temperature T^* . The plateau corresponds to a resistance roughly half of the normal state resistance as shown in panel (e). The $V(I)$ curves in the strong self-heating regime are irreversible and become reversible in the weak self-heating regime as shown by the arrows in panel (a). Panel (f) shows the irreversibility parameter $I_{\text{sw}} - I_{\text{ret}}$, the difference between respectively the switching and the retrapping current, as a function of temperature, for the virgin sample ($R_N = 14.2 \Omega$).

increase when switching from the non-dissipative to the dissipative branches of the $V(I)$ curve. At higher temperatures, the combination of a more efficient heat removal together with a reduced heating power as a consequence of a lower critical current and a higher thermal capacity, allows the PSs to be present without necessarily transforming themselves into a hot spot. This leads to a resistance plateau above the switching current resembling those well documented in long superconducting whiskers^[145]. The fact that the differential resistance of this plateau nearly coincides with half of the normal state resistance, arises from the time averaging of the dissipation during the acceleration/quench cycle of a PS at the constriction, similarly to the process described by the Skocpol-Beasley-Tinkham model^[150]. Note that the formation of a PS at the center of the constriction will perturb the condensate on a scale length $\sim 2\Lambda_Q$ much larger than the distance d between voltage probes, where $\Lambda_Q \approx 5 \mu\text{m}$ is the charge imbalance relaxation length for Al^[137]. Therefore, we can rule out the possibility that the voltage plateau could be ascribed to a normal state switching of a portion (smaller than the distance between voltage contacts) of the constriction.

The transition from weak to strong self-heating after switching is a natural consequence of the steady-state heat balance equation^[37]. On the one hand, the heat generation $P_{in} = \rho(J, T)J^2$ by the current density J traversing a section of material with resistivity $\rho(J, T)$, heats up the nanowire. On the other hand, there is a heat removal $P_{out} = h(T)(T - T_B)/r$ towards the cryogenic environment at temperature T_B , where $h(T)$ is the heat transfer coefficient and $r = A/P$, being A the area and P the perimeter of the cross section of the sample^[37]. The ratio $\alpha = \rho J_c^2 r / h(T_c - T_B)$, known as the Stekly parameter, accounts for the transition from a weak self-heating regime when $\alpha \ll 1$ to an important self-heating regime when $\alpha > 1$. In the case where an efficient heat removal is obtained (i.e. high h and thus low α), the above described plateau in the $V(I)$ curves should be also present at lower temperatures.

Possible ways to influence the heat removal could be achieved by changing the substrate material or by immersing the sample in a superfluid ^4He bath. The former method is unreliable since it implies comparing two different samples, whereas the latter is very limited since only two extreme situations can be contrasted. A more elegant approach for reducing the parameter α consists in narrowing down the constriction in a controlled way. By doing so, the critical current decreases and so does the parameter r and, as a consequence, a lower power dissipation and a better heat removal are expected. The result of this process, achieved via electromigration, is shown in Figure 6.2. In the virgin sample (panel (a)), the temperature about which the transition from nearly isothermal to severe self-heating happens is characterized by a noisy response observed at $T^* = 0.9 \text{ K}$ while a clear plateau develops at 1.1 K . As the width of the constriction is progressively reduced (see panels (b)-(e) in Figure 6.2), the plateau appears at lower temperatures in agreement with our interpretation of the

plateau as a unique signature of an efficient heat removal. It is interesting to point out that the noisy curve results from the fact that the constriction temperature in the steady state is defined by the equation $P_{in}(T) = P_{out}(T)$ which has at least two T values as solution at the transition^[37]. As a consequence of this bistability and the switching between these solutions, a noisy response is observed.

Further evidence supporting our interpretation that $V(I)$ curves with a single jump to the normal state correspond to strong self-heating effect, whereas curves exhibiting the plateau correspond to a regime where self-heating is unimportant, comes from the irreversible response under reversal of the current sweep^[151]. Indeed, in Figure 6.2(a) it can be seen that at high bath temperatures, the $V(I)$ curves are fully reversible, whereas at low bath temperatures a clear irreversible response develops when sweeping the current up and down. The switching current I_{sw} corresponds to the onset of dissipation when increasing current, and the retrapping current I_{ret} indicates the transition to the non dissipative regime when decreasing current. Figure 6.2(f) shows that the irreversibility width $I_{sw} - I_{ret}$ as a function of temperature starts to grow exactly at the same temperature where the plateau ceases to exist, in agreement with the scenario of a weak to strong self-heating transition. We have also found out that I_{ret} is rather independent on temperature, which is consistent with the fact that in the overheated regime, the bath temperature plays a minor role in its determination, as has been already discussed for long nanowires^[17,152]. We have noticed that different sample batches exhibit the crossover of thermal regimes at different values of the normal resistance of the constriction most likely due to important changes in the heat conductance through the substrate. This fact points out the importance of identifying the crossover temperature T^* as that where the plateau in the $V(I)$ appears rather than relying on the sample's normal resistance values.

It is worth mentioning that the here reported transition between thermal regimes of the nanoconstriction is quite similar to the well known thermomagnetic instability observed in superconducting thin films. In the latter, a balance between magnetic and thermal diffusion delimits the transition point^[153].

6.3 Switching current distributions

Due to the stochastic nature of the process triggering the switching events, repeating the same experiment under exactly the same external conditions of field and temperature does not necessarily provide the same value of $I_{sw}(T)$. Instead, the obtained I_{sw} will be distributed around a mean value $\langle I_{sw} \rangle(T)$. In order to map the functional form of this statistical distribution, a large number (10^4) of $V(I)$ curves needs to be measured. This can be achieved in a reasonable time when the current sweep rate is high enough. However, as has been pointed out above, the statistical distribution

depends on the chosen current sweep rate^[118]. This is illustrated in Figure 6.3(a) where several distributions obtained for different current ramps have been obtained on the same (non electromigrated) sample at 300 mK. The continuous curves shown in Figure 6.3(a) correspond to fits using the Gumbel function as described in Methods. The switching current was determined using a criterion of 33 % of the voltage jump. Since the number of experiments is constant, so is the area under each distribution curve. As explained in Ref. 118 the vertical axis in Figure 6.3(a) corresponds to the probability density of switching $P(I_{sw})$ multiplied by the bin size $\Delta I = 100$ nA.

In the present case a triangular shape sweeping function has been used with a constant maximum current of 30 μ A. It can be seen in Figure 6.3(a) that increasing the rate leads to an increase of $\langle I_{sw} \rangle$, as explained before^[118]. However, unlike in the uncorrelated PS model where a continuous narrowing down of the distribution is expected^[118], we now observe that the standard deviation of the distribution follows a non-monotonic trend. A possible explanation for the widening of the distribution when increasing the rate is the fact that as $\langle I_{sw} \rangle$ increases, heat dissipation also increases and so does the imprint left by PS events. Using the reasoning of Shah et al.^[146], the smaller the number of PSs in the sequence inducing the superconducting-to-resistive thermal runaway, the larger the stochasticity in the switching process and, hence, the wider the distribution of switching currents. In other words, as the sweeping rate increases, shorter train of PS events are needed leading to wider distributions. This trend, i.e. an increasing width of the distribution and increase of $\langle I_{sw} \rangle$ as current ramp increases, has been reproduced by Monte-Carlo simulations including self-heating effects (see Methods).

It has been theoretically shown^[118,154] that the distribution of switching currents depends on the frequency ν and amplitude A through the sweep rate νA . To illustrate this fact, the rightmost curve of Figure 6.3(a) shows data corresponding to different values of maximum current (30 and 60 μ A) and period (500 and 250 Hz) while keeping the same rate of 30 mA/s.

When the sweeping rate is increased to infinity, the critical (depairing) current of the nanoconstriction I_c should be reached. Although an infinite sweeping rate can not be achieved experimentally, it is possible to estimate this value by extrapolating the data corresponding to finite sweeping rate as shown in the inset of Figure 6.3(b) for $T = 900$ mK. The main panel of Figure 6.3(b) shows $I_c(T)$ determined by repeating the same extrapolation procedure for several temperatures. Note that the particular geometry of the used nanoconstriction could be regarded as a short nanowire (also known as S-c-S junction) or rather as a diffusive S-N-S junction^[155]. For the former, Kulik and Omel'yanchuk^[156,157] have provided a solution from the microscopic theory for the critical current for superconductor-constriction-superconductor junctions at arbitrary temperatures. This prediction is compared to the extrapolated points in

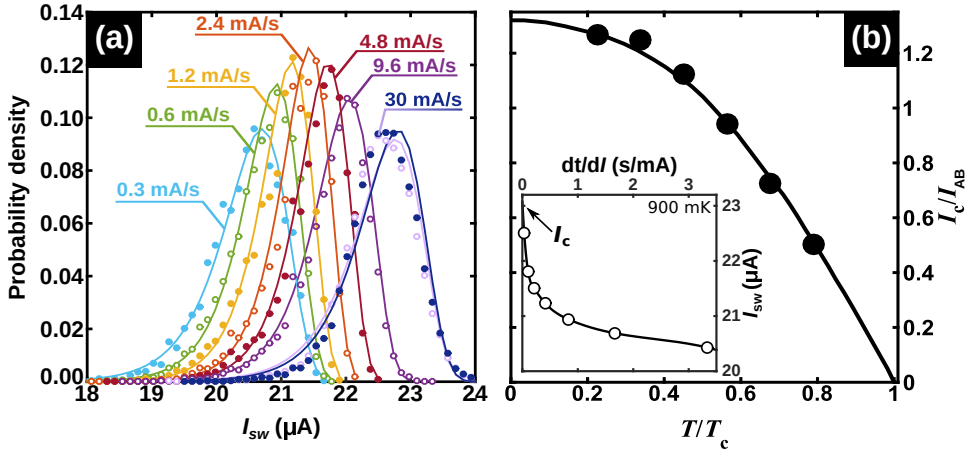


Figure 6.3: **Influence of sweeping rate on the current switch distribution.** (a) Distributions of switching current for different sweeping rates obtained at $T = 300$ mK for sample S2. Dark blue and light purple distributions (on the extreme right) were taken at the same rate but for different peak amplitude and frequency of sweep. Solid lines are attempts to fit the distributions with an Extreme Value Probability Density (or Gumbel) function. (b) Critical current as extrapolated for an infinite rate ($dt/dI = 0$), as a function of temperature for sample S3. The normalization factor $I_{AB} = \pi\Delta/2eR_N = 33 \mu\text{A}$ corresponds to the Ambegaokar-Baratoff expression of the maximum current for a tunnel junction. An example of extrapolation using splines is shown in the inset for $T = 900$ mK. The size of the experimental point exceeds the error bars as estimated from the difference between a linear and a parabolic extrapolation.

Figure 6.3(b). The normalization factor $I_{AB} = \pi\Delta/2eR_N = 33 \mu\text{A}$ corresponds to the Ambegaokar-Baratoff expression of the maximum current for a tunnel junction. As we suggested above, our samples could also be regarded as diffusive S-N-S microbridges. A detailed analysis of these systems can be found in Ref. 155 and the references therein. These authors show that for values of the ratio $\epsilon_c/\Delta \gg 1$ (short junctions limit), where $\epsilon_c = \hbar D/2\pi L^2$ is the Thouless energy scale, and Δ is the superconducting energy gap, the Kulik-Omel'yanchuk formula is recovered. This limit is satisfied in our samples for which we find $\epsilon_c/\Delta \sim 23$.

As pointed out before, the limiting case of infinite sweeping rate pushes I_{sw} towards I_c and therefore conceals the physics of PS events. This has been addressed in Ref. 148 where the temperature dependence of I_{sw} in Mo_3Ge nanowires obtained at finite sweeping rates exhibits a change of the functional dependence which was attributed to the transition from TAPS to the macroscopic quantum tunneling of the superconducting phase. Motivated by this approach, we have investigated the switching current distributions at a finite rate of 1.2 mA/s. Figure 6.4(a) summarizes the obtained switching current distributions for the virgin sample at several bath temperatures, whereas panel (b) of this figure shows the distributions for the same sample

after narrowing down the constriction in such a way that resistance increased by a factor of three. Assuming that the electromigration takes place in a single spot at the narrowest point of the isthmus^[42], this change of resistance roughly corresponds to a reduction of the constriction width down to ~ 17 nm. This width falls above the critical value of ~ 12 nm where a crossover towards QPS driven dissipation has been reported for similar samples^[50] suggesting that in the present samples, TAPS should be the dominant mechanism. As recently reported in Ref. 50, further electromigrating the sample allows one to access the QPS regime where a critical current becomes negligible, therefore preventing the study of the switching statistics.

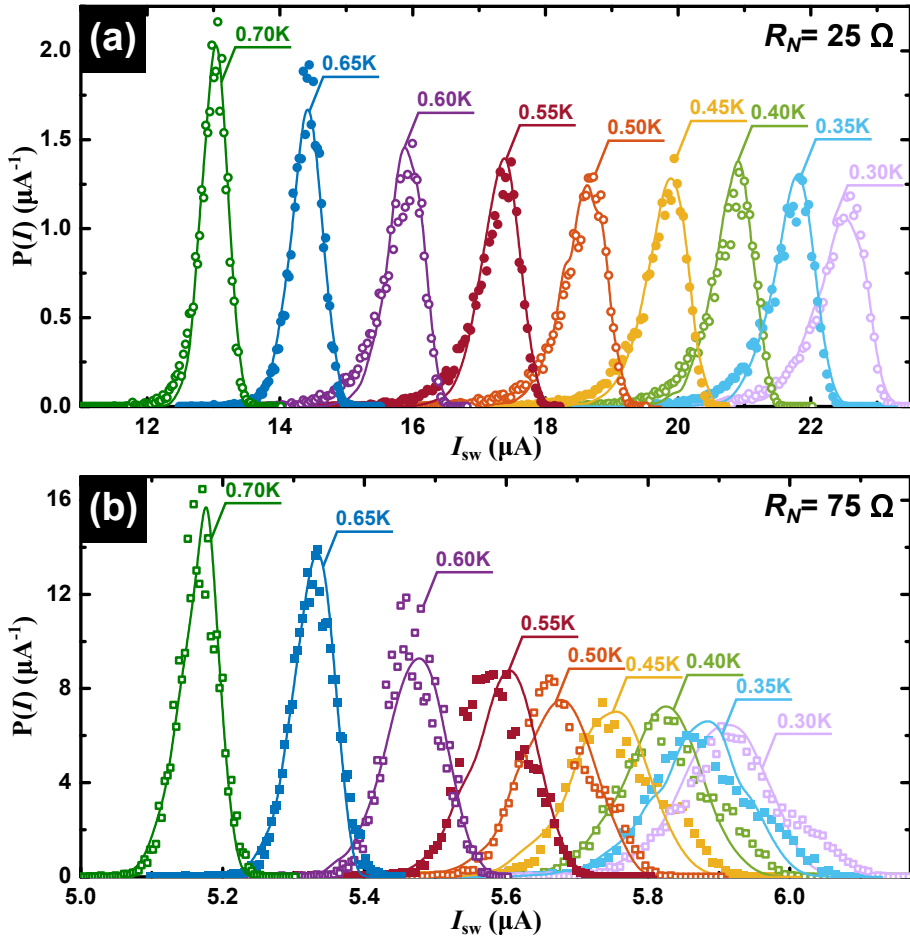


Figure 6.4: **Switching current distributions.** Temperature scan of switching current distributions obtained at a rate of 1.2 mA/s, (a) before and (b) after electromigration for sample S2. At each temperature, ten thousands $V(I)$ and the corresponding values of I_{sw} are recorded. Solid lines are attempts to fit the distributions with Monte-Carlo simulations including the effects of self-heating by multiple PS.

The continuous lines in Figure 6.4 are Monte Carlo fittings to the data taking into account self-heating effects produced by thermally excited PS, following the procedure described by Massarotti et al.^[147] and detailed in Methods. These fittings reproduce reasonably well the dependency of the experimental data for the virgin sample, whereas a somewhat less goodness of fit is observed for the electromigrated sample. A careful look to the low temperature distribution in the narrower sample reveals the existence of a second satellite hump next to the main peak which we attribute to the existence of a second competing nucleation point of PS events. Indeed, it has been shown that not only the current crowding effects produced by the reduced cross section of the wire lead to electromigrated voids, but that grain boundaries may also serve as nucleation points of this process^[25,26]. As a consequence, it is likely that the electromigration does not occur exactly at the narrowest part of the bridge, thus giving rise to two weak points with different critical currents^[50]. In view of the fact that two contiguous nucleation points will inevitably and mutually influence each other, the total probability density function cannot just be considered as the product of two individual and independent processes, a problem that has not been addressed so far.

A direct determination of the mean switching current $\langle I_{sw} \rangle(T) = (\sum_{i=1}^N I_{sw})/N$ and the standard deviation $\sigma(T) = \sqrt{\sum_{i=1}^N (I_{sw} - \langle I_{sw} \rangle)^2/N}$ can be obtained from the experimental data shown in Figure 6.4. The results are presented in Figure 6.5. Panel (a) shows the mean switching current $\langle I_{sw} \rangle$ for the virgin sample, along with the critical current I_c^{FIT} obtained from the fitting and Bardeen's expression^[158] $I_c(T) = I_{c0}(1 - (T/T_c)^2)^{3/2}$ (dashed line). The modelling considers a bias current I ramping from zero to $I_c^{\text{FIT}}(T)$. As soon as the temperature of the system reaches a threshold value T_{th} the system is defined to be in the resistive state and the relative value of the current is recorded as switching current I_{sw} . The $I_c^{\text{FIT}}(T)$ estimated from the simulations and shown in Figure 6.5 should be considered as the critical current (at the corresponding bath temperature) in absence of thermal fluctuations. In this sense it is expected and indeed observed in Figure 6.5(a),(b), that its value become larger than the experimentally determined $\langle I_{sw} \rangle(T)$. Panel (b) shows the same parameters for the sample after electromigration. In both panels, it is also included in the right vertical axis (grey square points) the number N_{PS} of PS events needed to trigger the switching process. Notice that for the virgin sample at the lowest measured temperature $T=0.3$ K, $N_{PS}=1$ and therefore a single PS is sufficient to increase the wire temperature above its critical temperature and trigger the switching process. After narrowing down the constriction (Figure 6.5(b)) the switching process takes place at lower currents, as expected. The fact that heat removal has been improved by reducing the constriction also leads to a higher number of PS needed to trigger the switching, consistent with the scenario described above. Furthermore, for both cases (virgin and electromigrated sample), N_{PS} monotonously increases with temperature, implying a better heat re-

moval, a weaker heating power and a lower level of stochasticity as T increases. This is also in agreement with the monotonous decrease of the standard deviations σ of the distributions shown in Figure 6.5(c) and the fact that the electromigrated sample exhibits a smaller σ .

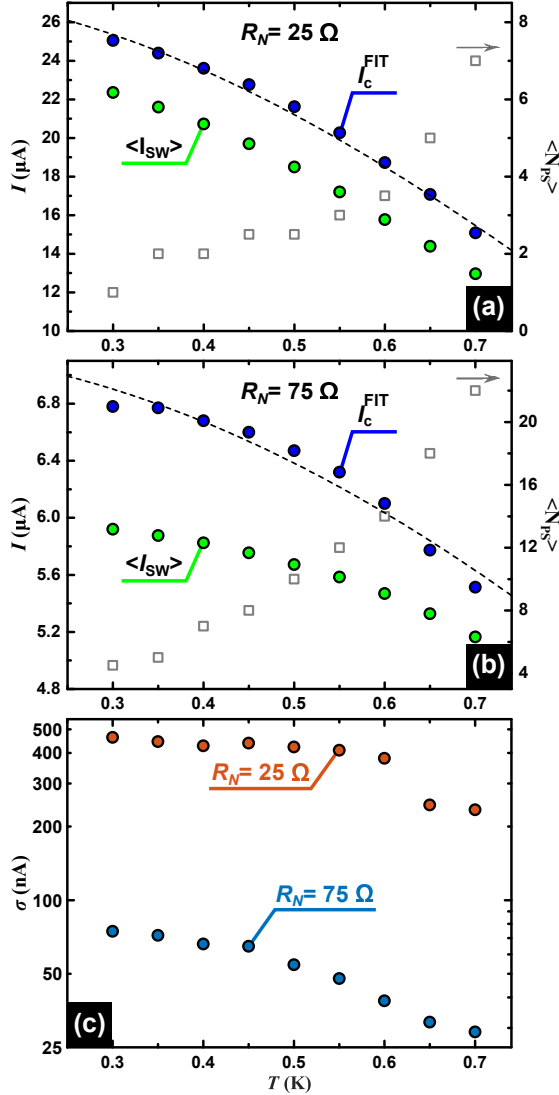


Figure 6.5: **Temperature dependence of the mean switching current and its standard deviation.** Green and blue circular symbols are respectively experimental data and values used in the fits presented in Figure 6.4 before (a) and after (b) electromigration. Light grey squared symbols are the mean number of PS involved in the switching. Black dotted lines correspond to Bardeen's expression for critical current. Panel (c) shows a monotonous decrease of the standard deviation of the switching current distribution.

The reduction of σ when decreasing the effective width of the constriction is consistent with previous reports on long nanowires^[159]. A decreasing σ with increasing T at high temperatures has been associated to the need of a train of PS events before switching to the normal state, whereas the observed flattening down of σ at low temperature has been interpreted as a signature of macroscopic quantum tunneling^[159]. In order to understand the change of σ with temperature for the particular case of a nanoconstriction, it is necessary to take into account the interplay of several competing effects. On the one hand, as T diminishes, the rate of TAPS decreases, fluctuations weaken and consequently σ should also decrease. On the other hand, lowering T leads also to an increase of the mean value of switching current ($\langle I_{\text{sw}} \rangle$) and a decrease of thermal conductivity (χ) and heat capacity (c) of the superconductor, all three factors combining to make the PSs more effective at heating the wire which would broaden the distribution. Our experimental data confirms that the influence of the last three factors overruns the influence of the decrease of TAPS when temperature is lowered, hence the broadening observed for the distribution^[17,149].

Let us now determine experimentally the switching rate $\Gamma(I, T)$. Since dI/dt is constant and $P(I)$ is obtained experimentally, $\Gamma(I, T)$ can be deduced by discretization (see Methods), from the experimental data shown in Figure 6.4. If we denote $K = 1$ the channel corresponding to the highest value of I_{sw} in the distribution, then $\Gamma(K)$ can be computed according to the formula^[160]:

$$\Gamma(K) = \frac{dI}{dt} \frac{1}{\Delta I} \ln \left(\frac{\sum_{j=1}^K P(j)}{\sum_{i=1}^{K-1} P(i)} \right) \quad (6.1)$$

where ΔI is the chosen binning size. The results of this analysis have been summarized in Figure 6.6 where the experimental data is indicated with symbols and continuous lines correspond to the theoretical fittings obtained from the Monte Carlo simulations including self-heating effects. The noisiness of the theoretical curves arises from the finite number of runs (4000) used to determine the distribution. At this point, we should stress that macroscopic quantum tunnelling does not need to be invoked to explain the observed effect at low temperatures in this particular sample. As recently reported in Ref. 130, it is possible to access the QPS regime by further electromigrating the sample. In this case, however, the critical current approaches zero, therefore making difficult to find a suitable range of samples' widths where it is possible to evidence the QPS influence on the switching statistics.

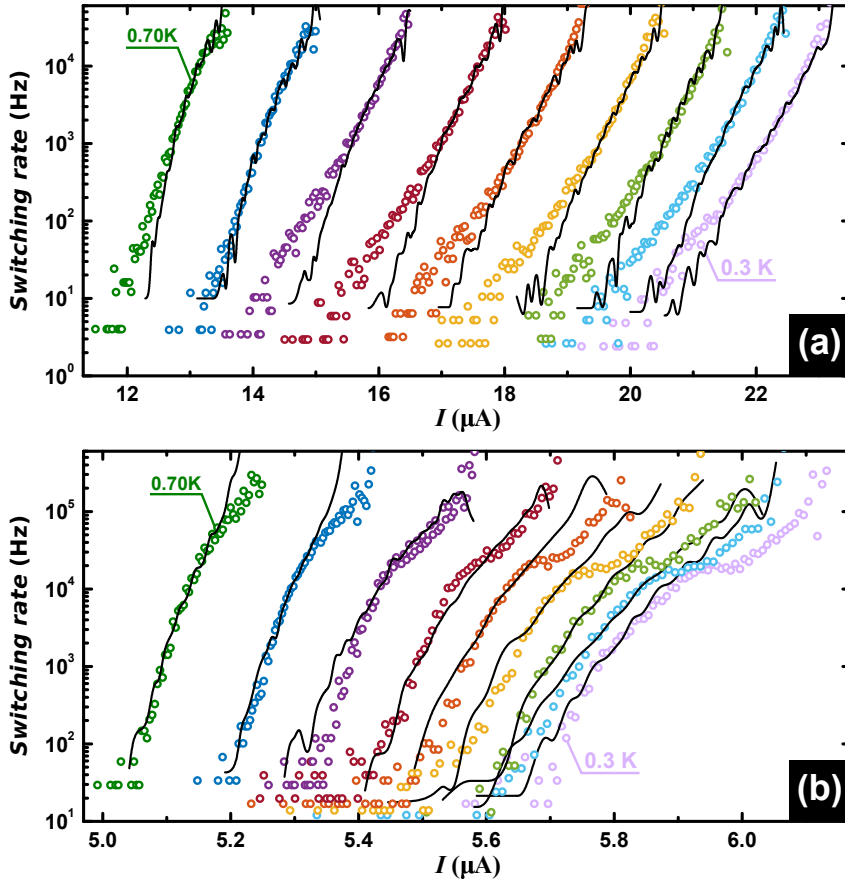


Figure 6.6: **Switching rates from the non-dissipative to the dissipative states.** Before (a) and after (b) narrowing down the constriction via electromigration. Experimental data corresponds to bath temperatures between 0.7 K (left most) and 0.3 K (right most). The black lines correspond to Monte-Carlo simulations for multiple PS events, including self-heating effects.

6.4 Methods

Sample granularity The Al grain size distribution is represented in Figure 6.1(d), where the probability density is plotted as a function of \sqrt{A} , the characteristic grain radius. This distribution was obtained by using the particle analysis tool provided by the ImageJ software, after filtering and binarization of the original image. A threshold was set at 200 nm^2 on the minimum value of the grain area, in order to avoid artefacts coming from noise in the image. The grains were counted in 50 nm^2 wide classes according to their area and the distribution was normalized by the total number of grains detected. The line in Figure 6.1(d) shows the fitting with a log-normal distribution and gives a mean characteristic grain radius of 18 nm.

Switching current distributions

The switching current distributions were taken using a digital phosphor oscilloscope (TDS5032B from Tektronix). A triangular wave signal was applied with desired amplitude and frequency using a function generator (K6221 from Keithley). The response of the sample was acquired via a low noise pre-amplifier (SR560 from Stanford Research Systems) giving an amplified signal to the oscilloscope. Triggering was ensured by a trigger link between function generator and oscilloscope. A home-made software was then in charge of acquiring the data from the oscilloscope: a voltage criterion was set for the switching, then time position of the switching event was located and transformed into the corresponding value of current via the knowledge of the applied wave. Ten thousands values for the switching current were registered for each temperature using this procedure.

Analytical and numerical fittings

The probability distribution of individual PS events when the current is swept with a rate dI/dt is given by^[160–162],

$$P(I) = \Gamma(I, T) (dI/dt)^{-1} \left[1 - \int_0^I P(u) du \right], \quad (6.2)$$

where $\Gamma(I, T)$ is the rate of events. This equation is a particular case of a Volterra equation of the second kind^[163] with general form of the solutions that can be derived analytically^[164]:

$$P(I) = (dI/dt)^{-1} \Gamma(I, T) e^{-(dI/dt)^{-1} (G(I, T) - G(0, T))}, \quad (6.3)$$

where $G(u, T) = \int \Gamma(u, T) du$. For a vast diversity of functional forms of $\Gamma(I, T)$ (see^[17,148,162]), Eq.(6.3) can be approximated by the Gumbel distribution^[148,159]:

$$P(I) = B^{-1} \exp \left[\frac{I - A}{B} - \exp \left(\frac{I - A}{B} \right) \right], \quad (6.4)$$

which has a mean $\langle I_{sw} \rangle = A - \gamma B$, where $\gamma \approx 0.577$ is the Euler-Mascheroni constant, and a standard deviation $\sigma = \pi B / \sqrt{6}$. Indeed, linearizing $\delta f(t, i) = \delta f(t) (1 - \frac{I}{I_c})^{5/4} \simeq \delta f(t) (1 - \frac{5I}{4I_c})$, the probability of switching is given by:

$$p(i) = \exp(c_1) \exp(c_2 i) \exp \left[\frac{-1}{c_2} (\exp(c_2 i) - 1) \right], \quad (6.5)$$

where $c_1 = \ln \left[\left(\frac{dI}{dt} \right)^{-1} \frac{\Omega}{2\pi} \right] - \frac{\Delta f}{k_B T}$ and $c_2 = \frac{5\Delta F}{4k_B T I_c}$. The goodness of fit using this expression is comparable to the one obtained using the Gumbel distribution.

The degree of asymmetry (skewness) and peakedness (kurtosis) of the Gumbel distribution are given by the third and fourth moments of the function, respectively,

and acquire constant (universal^[154]) values. Strictly speaking, Eq.6.2 is valid if the temperature T is well defined, i.e. if self-heating effects play no role. Since in our case the system is not in equilibrium with the cryogenic environment, it is necessary to take into account the heating driving process as described in Ref. 17,147. In the proposed model, a sample of length L in contact with a thermal bath at the temperature T_B is considered. A PS event induces heating in a segment $\ell \sim \xi(T)$. The equation for heat diffusion after the occurrence of a PS is:

$$\frac{d\delta T}{dt} + \alpha_r(T, T_B)\delta T = \eta(T, I) \sum_i \delta(t - t_i), \quad (6.6)$$

where $\delta T = T - T_B$ is the local increase of temperature and $\alpha_r(T, T_B)^{-1}$ is the relaxation time scale for the temperature T to return to its equilibrium value T_B after a sudden temperature rise η due to the PS at time t_i , has occurred. The distributions are obtained by running the simulation with 4000 determinations of the switching current. The numerical fitting procedure is obtained by adjusting two parameters: the critical current $I_c^{FIT}(T)$ and the threshold temperature T_{th} , i.e. the temperature above which we declare that the system has switched to a finite voltage state, which implies how many heating events are needed to induce the switching. We have found that for all fittings $0.11 \text{ K} < T_{th} - T < 0.17 \text{ K}$. For the simulations, we have used the following parameters $T_c = 1.3 \text{ K}$, diffusion constant $D = 49 \times 10^{14} \text{ nm}^2 \text{ s}^{-1}$, density of states at the Fermi level $\rho(\varepsilon_F) = 34.4 \text{ eV}^{-1} \text{ nm}^{-3}$. The length of the nanowire was 1500 nm, the length of its central part (along which PSs may occur) was 400 nm and its resistance in the normal state was 25 Ω . The superconducting coherence length at zero temperature was taken to be equal to 125 nm and the value of the superconducting gap to $2 \times 10^{-4} \text{ eV}$.

6.5 Conclusions

We have identified the presence of two distinct thermal regimes in planar superconducting nanoconstrictions. On the one hand, a weak self-heating regime where the heat removal is rather efficient and the superconducting constriction switches to the normal state in two steps when increasing current. On the other hand, a strong self-heating regime where the transition to the normal state corresponds to a single abrupt jump. In the former regime, a PS can exist as an oscillating order parameter with periodic phase jumps, whereas in the latter a hot spot develops. We have demonstrated the thermal origin of this transition by shifting it when reducing the size of the constriction. Irrespective of the thermal regime developed at currents larger than the switching current, the distribution of switching currents can be well accounted within a purely thermally activated PSs scenario. In addition, this chapter points out to the

importance of extending the current theoretical model to include mutual interaction of PS events occurring at short distances.

Although this chapter provides the first step towards an in-depth understanding of the effects of thermal fluctuations, further studies at lower temperatures are needed to clarify the role of QPS. The possibility to tune in a controlled way the thermal properties of the nanobridge and the fundamental energy scale, by reducing the critical current of the nanobridge through successive electromigration processes, will be the key knob to definitively address the transition to the quantum regime.

Chapter 7

Current-induced atomic
diffusion limits the dissipative
state of high T_c superconducting
bridges

7.1 Introduction

Electromigration has been and continues to be a real problem in electronics but may also become a factor limiting the applicability of spintronic devices requiring high current densities such as in domain-wall memories^[83,165].

In principle, superconducting nanocircuits are not concerned by atom migration problems chiefly because within the non-dissipative superconducting state there is no net momentum transfer between the carriers (Cooper pairs) and the atomic lattice. Furthermore, in low critical temperature superconductors, the critical current density J_c lies well below the current density J_{EM} needed to start displacing atoms.

This scenario may no longer hold for cuprate superconductors. The reason is twofold, on the one hand, the atomic diffusion barrier can be relatively weak for certain atoms like oxygen in $\text{YBa}_2\text{Cu}_3\text{O}_{7-\delta}$ (YBCO)^[97,99,166,167], consequently reducing J_{EM} . On the other hand, these compounds exhibit high superconducting critical current densities which may exceed J_{EM} at low temperatures. Under these circumstances, when the dissipative state is accessed by applying a current density $J > J_c$, the component of the current carried by the quasiparticles can surpass J_{EM} and produce irreversible damages to the material even at local temperatures substantially smaller than the melting point of the compound. This phenomenon seems to have been largely overlooked so far.

Motivated by these thoughts, we explored the temperature dependence of the electromigration current density in several conventional and cuprate superconductors and compared it with their corresponding superconducting critical current density. We observe that for YBCO there is a temperature range where the critical current density can exceed the current needed to trigger electromigration. As a consequence, within this region, surpassing the critical current density and reaching the dissipative state might lead to severe detrimental consequences on the circuits, such as local change of doping^[168], sample deformation^[169], or simply total destruction. This phenomenon could become visible in the abrupt penetration of flux due to thermomagnetic instabilities as recently reported in Ref. 170 and limit the lifetime of devices based on the superconducting dissipative state such as single photon detectors^[171].

7.2 Electromigration current density vs critical current density

All investigated superconductors are thin films patterned in a Dayem bridge or narrow constriction shape. A representative image of a YBCO constriction is shown in Figure 7.1(a). The transport properties were measured using a four-points Kelvin probe

configuration. Fabrication process and layout details for each specific material are described below.

A YBCO film with a thickness of 100 nm was grown by chemical solution deposition^[69] on LaAlO_3 single crystal substrate. Square $300\text{ }\mu\text{m} \times 300\text{ }\mu\text{m}$ Ag electrodes with 200 nm of thickness were sputtered and annealed by heating in an oxygen environment in order to reduce the contact resistance. Transport bridges of 1-2 μm width and 2-3 μm length were patterned with a 4-point geometry by photolithography followed by ion-beam etching. The fabrication details concerning Al and Nb constrictions can be found in Ref. 50 and Ref. 169, respectively.

In order to determine the electromigration current density J_{EM} we fed the sample with a train of pulses of 1 ms width, constant low value (bias) $I_{min} = 10\text{ mA}$ and linearly increasing high value I_{max} as schematically shown in Figure 7.1(b). The sample resistance reading takes place near the end of the flat top of the pulse, before the falling edge (R_{max}) and in between two consecutive pulses (R_{min}). Figure 7.1(c) shows the resulting R_{min} and R_{max} as a function of I_{max} for a typical measurement in a YBCO microbridge. Three different regimes can be identified. For low I_{max} (region I) the sample resistance does not depend on the intensity of the applied current, i.e. $R_{max} = R_{min}$. At intermediate I_{max} (region II), $R_{max} > R_{min}$ as consequence of joule heating effects and a non-zero resistance temperature coefficient α . By further increasing the applied current above a well defined threshold value I_{EM} , R_{min} starts to increase due to the current-induced modifications in the material properties (region III). In the particular case of YBCO, it has been suggested that at $I = I_{EM}$, oxygen atoms start to diffuse and therefore a local change of stoichiometry (and doping) is produced^[97,99,166,167]. For even higher current values, other atoms can be displaced and produce a visible damage on the structure^[168].

It is worth noting that the width of the pulse is much larger than the time needed for achieving a thermal stationary state ($\sim\text{ns}$) but substantially shorter than the time evolution of the material-dependent electromigration process ($\sim 1\text{ s}$)^[169]. The train of pulses is stopped once the resistance has increased by 1 %. For determining the superconducting critical current density J_c , either voltage-current characteristics are recorded at several temperatures and the critical current is estimated using a 1 μV criterion or pulsed measurements and $R_{max} \neq 0$ is used as criterion.

Figure 7.2 summarizes the obtained J_{EM} and J_c as a function of the bath temperature T_B . The inset shows the case of Al microbridges where $J_{EM} \gg J_c$ for all temperatures and therefore for which electromigration does not represent a major concern. Similar behavior is observed in $\text{La}_{2-x}\text{Ce}_x\text{CuO}_4$ (not shown) where the electromigration current at 50 K (13 MA/cm^2)^[168] already lies well above the maximum critical current density at zero Kelvin^[172] $J_c \approx 0.02\text{ MA/cm}^2$. The main panel of Figure 7.2 shows that a different trend is observed in YBCO. Indeed, it can be seen

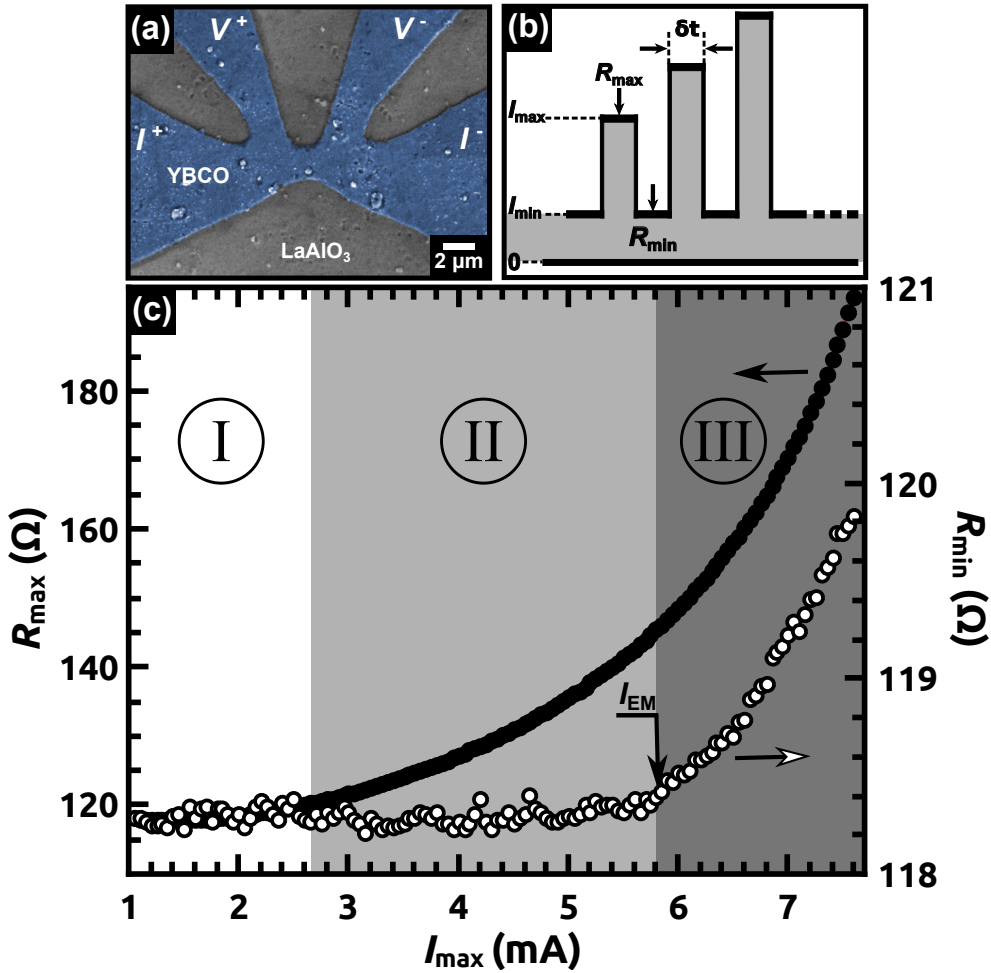


Figure 7.1: (a) Scanning electron image of a YBCO constriction. Electromigration takes place in between voltage constants where the current density reaches its maximum value. (b) Schematic representation of current pulses of dwell time $\delta t = 1$ ms, used to measure R_{min} and R_{max} . (c) Representative R_{min} (open points) and R_{max} (solid points) as a function of I_{max} for YBCO at 300 K. The criterion used to determine I_{EM} is indicated. Region I corresponds to negligible heating effects. In region II heating effects are important although without inducing any damage in the bridge. Deterioration of the sample develops in region III.

that the two lines $J_{\text{EM}}(T_B)$ and $J_c(T_B)$ intersects at $T^* \approx 75$ K. For temperatures $T^* < T_B < T_{c0}$, it is possible to access the normal state by applying sufficiently high currents and without producing any damage to the sample. However, for $T_B < T^*$, reaching the normal state can be done at expenses of irreversibly modifying the properties of the sample. In our case, reaching the normal state for $T_B < T^*$ leads to total destruction of the sample if no controlled feedback loop is used.

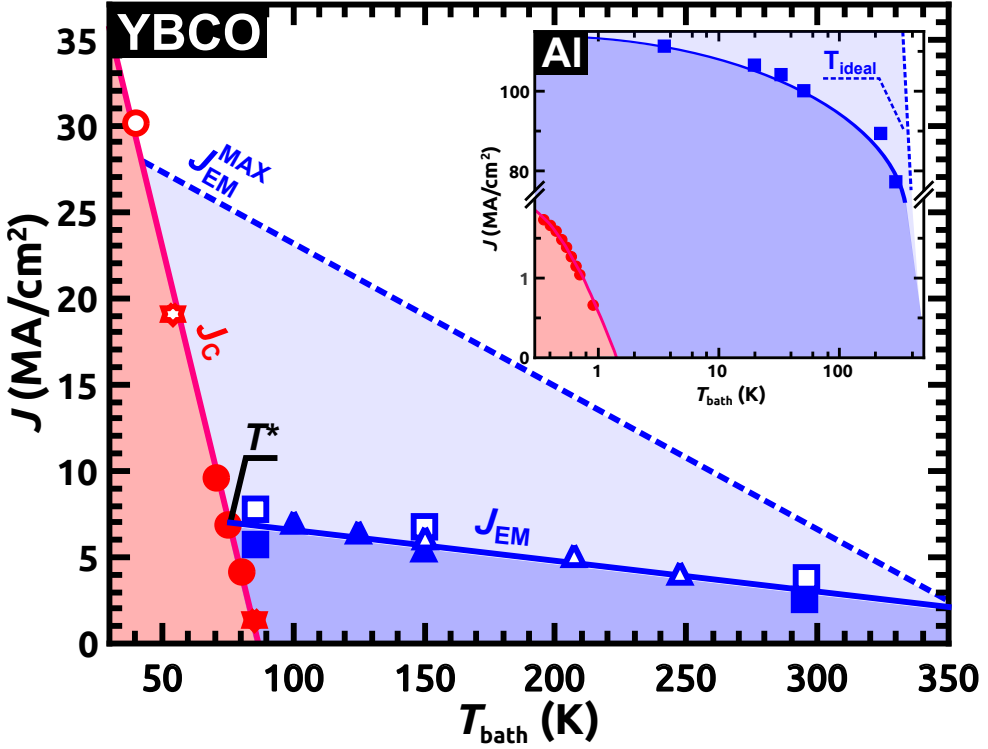


Figure 7.2: Superconducting critical current density J_c and electromigration current density J_{EM} for Al (inset) and YBCO (main panel), as a function of the bath temperature. The $J_{EM}(T)$ dependence obtained in a closed-cycle cryostation is indicated with symbols. Different symbols corresponding to different samples. This curve can shift substantially upwards upto J_{EM}^{max} when the heating effects are negligible (dotted line). Error bars are smaller than the size of the symbols.

It should be emphasized that for current densities exceeding J_c , the local temperature at the constriction (T_{local}) can rise substantially above the bath temperature, depending on the heat removal efficiency of the cryostat. In other words, $J_{EM}(T_B)$ will fall systematically below $J_{EM}(T_{\text{local}})$. As a consequence, the intersection temperature T^* can be shifted to lower values by improving the cooling power of the cryostat. In the present work, the investigation has been performed in a Montana closed-cycle cryostat, with the sample mounted on a cold finger with a relatively poor cooling power (~ 0.1 -1 W). By immersing the sample in liquid nitrogen, T^* should be further reduced and thus extending the temperature range where the normal state can be accessed without any harm. It is possible to estimate the minimum achievable T^* (or similarly the maximum possible J_{EM}) considering that for an infinitely efficient heat sink, $T_B = T_{\text{local}}$. In turn, T_{local} can be determined through the measured R_{max} at

I_{EM} and using the sample resistance as a thermometer. This approach provides an underestimation of T_{local} with an error diminishing as the ratio δ/d , between thermal healing length (δ) and the distance between voltage contacts (d), increases^[37]. Here $\delta = \sqrt{\chi t / \Upsilon}$, with χ the thermal conductivity of the material, Υ the heat transfer coefficient to the substrate, and t the sample thickness. The resulting $J_{EM}(T_{local})$ curves are indicated in Figure 7.2 as J_{EM}^{max} . The fact that the temperature difference $T_{local} - T_B$ becomes more pronounced at low temperatures reflects the fact that heating effects increase as T decreases. This is expected since χ , Υ , and the specific heat C decrease as T decreases. In addition, since J_{EM} increases at low temperatures, so does the associated joule heating.

7.3 Conclusions

To summarize, we have presented a comparative analysis of the temperature dependence of the electromigration current density for Al and YBCO microbridges. We show that for YBCO, there is a temperature range where the superconducting critical current can exceed the extrapolated electromigration current. Within this regime, accessing the dissipative (or normal) state can have detrimental consequences to the devices. We propose to shrink the temperature range where this harmful regime takes place by improving the heat evacuation and we estimate the maximum possible gain that one can expect by implementing this strategy. It would be interesting to extend this study to Fe-based superconductors and other technologically relevant superconductors such as NbN, Nb₃Sn, or MgB₂. A question that deserves more experimental and theoretical work is the possibility to achieve electromigration in the dissipative superconducting state. In this regime, the total current density $J_{tot} = J_s + J_n$ splits in a non-dissipative component J_s carried by the Cooper pairs, and another dissipative component J_n taken by the quasiparticles. Assuming isothermal conditions, electromigration can take place once $J_n > J_{EM}$. In another vein, it is not clear what would be the influence of an external magnetic field on J_{EM} and whether it will tend to reduce or increase T^* . Clearly, further experimental investigation are needed to address these questions.

Conclusion and perspectives

In this thesis, we make use of electromigration, a phenomenon long known as a detrimental process in electronic circuits, to outperform the limits of nanofabrication and study superconductivity in point contacts, constrictions and short nanowires. Several other techniques had already been considered to achieve this goal, such as Ar^+ sputtering^[117,173] or tape peel-off^[127], but all of them were limited to, at best, a few nanometers. While it has a response which depends strongly on the used material and imposes limitations to the geometrical shape of the structure, EM possesses strong extra benefits in comparison to these other methods lying in its low cost of implementation, its accuracy and the possibility to use it in situ.

In practice, EM is accomplished by implementing a reacting electronic feedback loop, in order to reliably reduce the size of a single nanowire. Starting from nanojunctions with a bow-tie geometry, so that EM would be expected in the close vicinity of the constriction, it is possible to reduce their width down to a few atoms. The resistance of the junction, directly linked to its cross-section, was selectable as the control software was capable of controlling the EM speed and final conductance threshold quite accurately.

Electromigration had been widely used to form nanogaps and point contacts with materials such as Al and Au, but little was known of its effects in other conductors. In the same way, the reversibility of the process was reported for some specific materials^[64] but the universality of the process was never questioned. We investigated superconducting nanoconstrictions thanks to EM in a variety of superconductors, going from conventional conductors to cuprates. We showed that EM is a reversible process in Al, partially reversible in $\text{La}_{2-x}\text{Ce}_x\text{CuO}_4$ and mainly irreversible in Nb. We showed that more complex phenomena than atom migration inducing cross-section reduction were at work in the last two mentioned compounds. We finally demonstrated the enormous potential of the proposed method to fine-tune the size/resistance of superconducting constrictions by combining runs of EM and anti-EM or alternatively by using current pulses.

Once the process of current assisted atomic migration was mastered, the develop-

ment of phase slips in superconducting nanowires was investigated and we were able to establish the threshold cross-section where fluctuations in the system switch from a thermal to a quantum dominated regime. We provided clear evidences for the explanation of the closely linked phenomenon of negative magneto-resistance, namely the destruction of superconductivity in the leads of the bridge, and we reported on a superconducting-to-insulator transition at high resistances. The latter was obtained at the level of the quantum of conductance, corresponding to roughly a single atom wide constriction.

Concerning the dynamics of phase slips, we have identified two distinct thermal regimes in superconducting nanojunctions. The first one corresponds to the existence of a single phase slip with efficient heat removal and is thus called weak self-heating regime. In this regime, the $V(I)$ characteristics are reversible and show a plateau corresponding to the oscillating phase slip. The second one corresponds to an avalanche of phase slips leading to a hot spot and is thus called strong self-heating regime. In this regime, the current-voltage characteristics are irreversible as evidenced by a clear hysteresis. The thermal origin of the transition between this two regimes was corroborated by a gradual reduction of the size achieved by EM. Moreover, by analysing the statistical distribution of phase slips, we could demonstrate that the switching current probability function could be well explained by a model including only the effect of thermally activated phase slips.

Following the interesting work on cuprates, we looked into narrow bridges of $\text{YBa}_2\text{Cu}_3\text{O}_{7-\delta}$ and compared the values of their critical current and their EM current. We highlighted the fact that, with decreasing temperature and at a certain $T^* < T_c$, J_c became higher than the extrapolated value of J_{EM} . This was in complete contrast with the case of Al, where J_c is clearly one or two orders of magnitude lower than J_{EM} for the whole range of temperature. Previous studies showed EM being triggered from the normal and the superconducting state in Pb^[174]. Of course, that was supposing that the sample first became normal before undergoing EM because Cooper pairs cause no momentum transfer in the superconducting state. Nevertheless, with our findings, it is possible to envision a way to electromigrate in the dissipative state, between the superconducting and normal states.

Although we furnished compelling evidences of a transition between phase slips regimes in nanoscale superconductors, further experimental efforts are needed to perfectly understand the role of quantum phase slips, as it was particularly highlighted in Chapter 6. This will surely necessitate studies at ultra-low temperatures.

Combining EM with local increase of temperature or with magnetic field and enhancing density of current stream lines could maybe help to trigger it at precise spots and help to create exotic structures such as connected islands of metallic materials. Considering the effect of polarization on a ferroelectric substrate^[175], we could also

imagine being able to trigger EM with some spatial control by taking advantage of local modifications of T_c . EM of superconductors like NbN or MgB₂ could also be interesting, as they are of relative technological relevance.

Further advances could be imagined on EM itself, assisted by the powerful technique of in situ visualization. With the acquired control of the process, progress in graphene related topics could be realized, as large current densities have already proven themselves as positive contributors to this field^[176,177].

It would be interesting also to investigate the EM in flexible substrates such as kapton, as the new technology trend is towards flexible electronics. In this case, mechanical stress might severely reduce the current needed to trigger EM, and thus set a limit for lifetime and miniaturization of such devices.

Bibliography

- [1] H. K. Onnes, *The superconductivity of mercury*, Comm. Phys. Lab. Univ. Leiden **122**, 124 (1911). 30
- [2] L. N. Cooper, *Bound electron pairs in a degenerate Fermi gas*, Phys. Rev. **104**, 1189 (1956). 30
- [3] J. Bardeen, L. N. Cooper, and J. R. Schrieffer, *Theory of superconductivity*, Phys. Rev. **108**, 1175 (1957). 31
- [4] F. London and H. London, *The electromagnetic equations of the supraconductor*, Proc. Roy. Soc. **A149**, 71 (1935). 31
- [5] W. Meissner and R. Ochsenfeld, *Ein neuer Effekt bei Eintritt der Supraleitfähigkeit*, Naturwissenschaften **21**, 787 (1933). 31
- [6] W. J. Elion, M. Matters, U. Geigenmüller, and J. E. Mooij, *Direct demonstration of Heisenberg's uncertainty principle in a superconductor*, Nature **371**, 594 (1994). 32
- [7] B. D. Josephson, *Possible new effects in superconductive tunnelling*, Phys. Lett. **1**, 251 (1962). 32, 36
- [8] M. Tinkham, *Introduction to Superconductivity*, 2 ed. (Dover Publications, Inc., 1996). 33, 35, 39, 40, 43, 44, 45, 46, 47
- [9] V. L. Ginzburg and L. D. Landau, *On the theory of superconductivity*, Zh. Eksp. Teor. Fiz. **20**, 1064 (1950). 34, 35, 38
- [10] L. Gor'kov, *Microscopic derivation of the Ginzburg-Landau equations in the theory of superconductivity*, J. Exptl. Theoret. Phys. **36**, 1918 (1959). 34, 35
- [11] A. A. Abrikosov, *On the magnetic properties of superconductors of the second group*, J. Exptl. Theoret. Phys. **32**, 1174 (1957). 38

- [12] D. Saint-James and P. G. de Gennes, *Onset of superconductivity in decreasing fields*, Phys. Lett. **7**, 306 (1963). 39
- [13] V. A. Schweigert and F. M. Peeters, *Influence of the confinement geometry on surface superconductivity*, Phys. Rev. B **60**, 3084 (1999). 39
- [14] J. S. Langer and V. Ambegaokar, *Intrinsic Resistive Transition in Narrow Superconducting Channels*, Phys. Rev. **164**, 498 (1967). 41, 44, 47
- [15] W. A. Little, *Decay of persistent currents in small superconductors*, Phys. Rev. **156**, 396 (1967). 41, 45
- [16] N. Giordano, *Dissipation in a one-dimensional superconductor: Evidence for macroscopic quantum tunneling*, Phys. Rev. B **41**, 6350 (1990). 46
- [17] D. Pekker, N. Shah, M. Sahu, A. Bezryadin, and P. M. Goldbart, *Stochastic dynamics of phase-slip trains and superconductive-resistive switching in current-biased nanowires*, Phys. Rev. B **80**, 214525 (2009). 46, 121, 126, 132, 134, 135
- [18] D. E. McCumber and B. I. Halperin, *Time Scale of Intrinsic Resistive Fluctuations in Thin Superconducting Wires*, Phys. Rev. B **1**, 1054 (1970). 47
- [19] A. D. Zaikin, D. S. Golubev, A. van Otterlo, and G. T. Zimanyi, *Quantum fluctuations and dissipation in thin superconducting wires*, Physics-Uspekhi **41**, 226 (1998). 47
- [20] P. B. Ghate, *Some observations on the electromigration in aluminum films*, Appl. Phys. Lett. **11**, 14 (1967). 50
- [21] I. A. Blech and E. S. Meieran, *Direct transmission electron microscope observation of electrotransport in aluminum thin films*, Appl. Phys. Lett. **11**, 263 (1967).
- [22] R. Rosenberg and L. Berenbaum, *Resistance monitoring and effects of nonadhesion during electromigration in aluminum films*, Appl. Phys. Lett. **12**, 201 (1968).
- [23] J. R. Black, *Electromigration failure modes in aluminum metallization for semiconductor devices*, Proceedings of the IEEE **57**, 1587 (1969). 50, 58, 93
- [24] F. d'Heurle and I. Ames, *Electromigration in single-crystal aluminum films*, Appl. Phys. Lett. **16**, 80 (1970). 50, 60, 93
- [25] I. A. Blech, *Electromigration in thin aluminum films on titanium nitride*, J. Appl. Phys. **47**, 1203 (1976). 130

- [26] P. S. Ho and T. Kwok, *Electromigration in metals*, Rep. Prog. Phys. **52**, 301 (1989). 50, 130
- [27] J. R. Lloyd, *Electromigration for designers: an introduction for the non-specialist*, https://www.eetimes.com/document.asp?doc_id=1275855, 2002. 50, 51, 60, 94
- [28] P. S. Ho and T. Kwok, *Electromigration in metals*, Rep. Prog. Phys. **52**, 301 (1989). 51, 60
- [29] S. Elliott, *The Physics and Chemistry of Solids*, 2 ed. (John Wiley and Sons, Inc., 2000). 51, 52
- [30] H. Ibach and H. Lüth, *Solid State Physics*, 4 ed. (Springer, 2009). 53
- [31] V. Levitin, *Atom Vibrations in Solids: Amplitude and Frequencies*, 1 ed. (Cambridge Scientific Publishers Ltd, 2004). 53
- [32] J. R. Lloyd, *Electromigration in thin film conductors*, Semicond. Sci. Technol. **12**, 1177 (1997). 54, 55, 56, 58
- [33] H. B. Huntington and A. R. Grone, *Current-induced marker motion in gold wires*, J. Phys. Chem. Solids **20**, 76 (1961). 55, 96
- [34] C. Bosvieux and J. Friedel, *Sur l'électrolyse des alliages métalliques*, J. Phys. Chem. Solids **23**, 123 (1962). 55, 96
- [35] H. Brophy, R. M. Rose, and J. Wulff, *The Structure and Properties of Materials* (John Wiley and Sons, Inc., 1964). 57, 58
- [36] H. Fangohr, D. S. Chernyshenko, M. Franchin, T. Fischbacher, and G. Meier, *Joule heating in nanowires*, Phys. Rev. B **84**, 054437 (2011). 57, 95
- [37] A. V. Gurevich and R. G. Mints, *Self-heating in normal metals and superconductors*, Rev. Mod. Phys. **59**, 941 (1987). 59, 120, 125, 126, 142
- [38] I. A. Blech, *Electromigration in thin aluminum films on titanium nitride*, J. Appl. Phys. **47**, 1203 (1976). 59, 60
- [39] M. F. Lambert, M. F. Goffman, J. P. Bourgoin, and P. Hesto, *Fabrication and characterization of sub-3 nm gaps for single-cluster and single-molecule experiments*, Nanotechnology **14**, 772 (2003). 60
- [40] G. Esen and M. S. Fuhrer, *Temperature control of electromigration to form gold nanogap junctions*, Appl. Phys. Lett. **87**, 263101 (2005). 61, 63, 64, 68, 110

- [41] D. R. Strachan *et al.*, *Controlled fabrication of nanogaps in ambient environment for molecular electronics*, Appl. Phys. Lett. **86**, 043109 (2005). 61, 63, 64, 111
- [42] D. R. Strachan *et al.*, *Clean Electromigrated Nanogaps Imaged by Transmission Electron Microscopy*, Nano Lett. **6**, 441 (2006). 129
- [43] M. L. Trouwborst, S. J. v. d. Molen, and B. J. v. Wees, *The role of Joule heating in the formation of nanogaps by electromigration*, J. Appl. Phys. **99**, 114316 (2006). 61, 68, 110
- [44] H. Park, A. Lim, A. Alivisatos, J. Park, and P. McEuen, *Fabrication of metallic electrodes with nanometer separation by electromigration*, Appl. Phys. Lett. **75**, 301 (1999). 60
- [45] H. Park *et al.*, *Nanomechanical oscillations in a single-C60 transistor*, Nature **407**, 57 (2000). 61
- [46] J. Park *et al.*, *Coulomb blockade and the Kondo effect in single-atom transistors*, Nature **417**, 722 (2002).
- [47] L. H. Yu and D. Natelson, *The Kondo Effect in C60 Single-Molecule Transistors*, Nano Lett. **4**, 79 (2004). 61
- [48] N. Ittah, I. Yutsis, and Y. Selzer, *Fabrication of Highly Stable Configurable Metal Quantum Point Contacts*, Nano Lett. **8**, 3922 (2008). 61, 90, 103
- [49] J. M. Campbell and R. G. Knobel, *Feedback-controlled electromigration for the fabrication of point contacts*, Appl. Phys. Lett. **102**, 023105 (2013). 61, 63, 64, 68
- [50] X. D. A. Baumanns *et al.*, *Thermal and quantum depletion of superconductivity in narrow junctions created by controlled electromigration*, Nat. Commun. **7**, 10560 (2016). 61, 94, 95, 122, 129, 130, 139
- [51] W. Seith and S. Wever, *On a new effect in the electrolytic transfer in solid alloys*, Z. Elektrochem. **57**, 891 (1953). 61
- [52] T. Aref and A. Bezryadin, *Precise in situ tuning of the critical current of a superconducting nanowire using high bias voltage pulses*, Nanotechnology **22**, 395302 (2011). 61, 93
- [53] J. Moser, A. Barreiro, and A. Bachtold, *Current-induced cleaning of graphene*, Appl. Phys. Lett. **91**, 163513 (2007). 61

- [54] T. Taychatanapat, K. I. Bolotin, F. Kuemmeth, and D. C. Ralph, *Imaging Electromigration during the Formation of Break Junctions*, Nano Lett. **7**, 652 (2007). 61, 71
- [55] C. Xiang, J. Y. Kim, and R. M. Penner, *Reconnectable Sub-5 nm Nanogaps in Ultralong Gold Nanowires*, Nano Lett. **9**, 2133 (2009). 61, 90, 103
- [56] H. B. Heersche, G. Lientschnig, K. O'Neill, H. S. J. van der Zant, and H. W. Zandbergen, *In situ imaging of electromigration-induced nanogap formation by transmission electron microscopy*, Appl. Phys. Lett. **91**, 072107 (2007). 63
- [57] A. A. Houck, J. Labaziewicz, E. K. Chan, J. A. Folk, and I. L. Chuang, *Kondo Effect in Electromigrated Gold Break Junctions*, Nano Lett. **5**, 1685 (2005). 63
- [58] O. Elíasson *et al.*, *Power regulation and electromigration in platinum microwires*, Review of Scientific Instruments **85**, 114709 (2014). 63
- [59] Y. Kanamaru, M. Ando, and J.-i. Shirakashi, *Ultrafast feedback-controlled electromigration using a field-programmable gate array*, J. Vac. Sci. Technol. B **33**, 02B106 (2014). 63
- [60] V. Zharinov, X. D. A. Baumans, A. V. Silhanek, E. Janssens, and J. Van de Vondel, *Controlled electromigration protocol revised*, Rev. Sci. Instrum. **89**, 043904 (2018). 64, 65, 66, 95
- [61] K. J. Astrom and R. M. Murray, *Feedback Systems: An Introduction for Scientists and Engineers* (Princeton University Press, 2008). 65
- [62] E. Ruska, *Nobel prize in physics "for his fundamental work in electron optics, and for the design of the first electron microscope"*, https://www.nobelprize.org/nobel_prizes/physics/laureates/1986/ruska-facts.html, 1986. 68
- [63] J. I. Goldstein *et al.*, *Scanning Electron Microscopy and X-Ray Microanalysis*, 4 ed. (Springer, 2018). 68, 69
- [64] T. Kozlova, M. Rudneva, and H. W. Zandbergen, *In situ TEM and STEM studies of reversible electromigration in thin palladium-platinum bridges*, Nanotechnology **24**, 505708 (2013). 71, 90, 95, 143
- [65] A. J. V. Griffiths and T. Walther, *Quantification of carbon contamination under electron beam irradiation in a scanning transmission electron microscope and its suppression by plasma cleaning*, J. Phys. Conf. Ser. **241**, 012017 (2010). 71

- [66] A. E. Ennos, *The origin of specimen contamination in the electron microscope*, B. J. Appl. Phys. **4**, 101 (1953). 71
- [67] A. E. Ennos, *The sources of electron-induced contamination in kinetic vacuum systems*, B. J. Appl. Phys. **5**, 27 (1954). 71
- [68] H. Saadaoui *et al.*, *The phase diagram of electron-doped $\text{La}_{2-x}\text{Ce}_x\text{CuO}_4 - \delta$* , Nat. Commun. **6**, 6041 (2015). 74
- [69] X. Obradors *et al.*, *Growth, nanostructure and vortex pinning in superconducting $\text{YBa}_2\text{Cu}_3\text{O}_7$ thin films based on trifluoroacetate solutions*, Supercond. Sci. Technol. **25**, 123001 (2012). 74, 139
- [70] D. Massarotti *et al.*, *Macroscopic quantum tunnelling in spin filter ferromagnetic Josephson junctions*, Nat. Commun. **6**, 7376 (2015). 79
- [71] W. Gifford, *The gifford-mcmahon cycle*, Adv. Cryog. Eng. **11**, 152 (1966). 80
- [72] M. Instruments, *Montana instruments knowledge base*, available online at <http://ressources.montanainstruments.com/help>, 2017. 80
- [73] C. D. Motchenbacher and J. A. Connelly, *Low-Noise electronic system design*, 1 ed. (John Wiley and Sons, Inc., 1993). 80
- [74] W. Buckel and R. Kleiner, *Superconductivity: Fundamentals and Applications*, 2 ed. (Wiley, 2004). 80
- [75] J. R. Barry, E. A. Lee, and D. G. Messerschmitt, *Digital communication*, 3 ed. (Springer, 2003). 80
- [76] Y. Blanter and M. Büttiker, *Shot noise in mesoscopic conductors*, Physics Reports **336**, 1 (2000). 81
- [77] R. F. Voss, *Linearity of $1/f$ noise mechanisms*, Phys. Rev. Lett. **40**, 913 (1978). 81
- [78] Z. Li, C. L. Bauer, S. Mahajan, and A. G. Milnes, *Degradation and subsequent healing by electromigration in Al-1 wt % Si thin films*, J. Appl. Phys. **72**, 1821 (1992). 90, 93
- [79] C.-F. Hong, M. Togo, and K. Hoh, *Repair of Electromigration-Induced Voids in Aluminum Interconnection by Current Reversal*, Jpn. J. Appl. Phys. **32**, L624 (1993). 90, 93
- [80] J. Brisbois *et al.*, *Magnetic flux penetration in Nb superconducting films with lithographically defined microindentations*, Phys. Rev. B **93**, 054521 (2016). 92

- [81] J. J. Spokas and C. P. Slichter, *Nuclear Relaxation in Aluminum*, Phys. Rev. **113**, 1462 (1959). 93
- [82] J. Bass, *The formation and motion energies of vacancies in aluminium*, Philo. Mag. **15**, 717 (1967). 93
- [83] C.-Y. You, I. M. Sung, and B.-K. Joe, *Analytic expression for the temperature of the current-heated nanowire for the current-induced domain wall motion*, Appl. Phys. Lett. **89**, 222513 (2006). 94, 138
- [84] W. J. Skocpol, M. R. Beasley, and M. Tinkham, *Self-heating hotspots in superconducting thin-film microbridges*, J. Appl. Phys. **45**, 4054 (1974). 95
- [85] K. Mizuno and T. Aomine, *Temperature Dependence of Critical Current in Granular Al Bridges with Different Thicknesses and Widths*, J. Phys. Soc. Jpn. **48**, 1908 (1980). 95
- [86] W. Jeong, K. Kim, Y. Kim, W. Lee, and P. Reddy, *Characterization of nanoscale temperature fields during electromigration of nanowires*, Sci. Rep. **4**, 4975 (2014). 95
- [87] M. Zgirski and K. Y. Arutyunov, *Experimental limits of the observation of thermally activated phase-slip mechanism in superconducting nanowires*, Phys. Rev. B **75**, 172509 (2007). 95, 113
- [88] Y. Serruys, *Electromigration du niobium-95 et du tantale-182 dans le niobium*, Scr. Metall. **16**, 365 (1982). 96
- [89] Y. Serruys and G. Brébec, *Electromigration dans le niobium*, Philo. Mag. A **45**, 563 (1982). 96
- [90] R. P. Gupta, Y. Serruys, G. Brébec, and Y. Adda, *Calculation of the effective valence for electromigration in niobium*, Phys. Rev. B **27**, 672 (1983). 96
- [91] W. DeSorbo, *Effect of Dissolved Gases on Some Superconducting Properties of Niobium*, Phys. Rev. **132**, 107 (1963). 98
- [92] J. Halbritter, *On the oxidation and on the superconductivity of niobium*, Appl. Phys. A **43**, 1 (1987). 98
- [93] H. Shiraishi, K. Furuya, and R. Watanabe, *Change in solute oxygen level and loss of ductility of niobium during oxidation in imperfect vacuum conditions*, J. Less Common Met. **63**, 147 (1979). 98
- [94] M. Murakami and T. Yogi, *Strain in evaporated Nb thin films*, J. Appl. Phys. **57**, 211 (1985). 98

- [95] A. K. Vijh, *Influence of Bond Energies of Oxides on the Kinetics of Anodic Oxide Growth on Valve Metals*, J. Electrochem. Soc. **116**, 972 (1969). 99
- [96] A. K. Vijh, *On some aspects of low-temperature and anodic oxidation of metals and semiconductors*, Oxid. Met. **4**, 63 (1972). 99
- [97] K. G. Rajan, P. Parameswaran, J. Janaki, and T. S. Radhakrishnan, *Electromigration of oxygen in $YBa_2Cu_3O_{7-\delta}$* , J. Phys. D: Appl. Phys. **23**, 694 (1990). 99, 138, 139
- [98] B. H. Moeckly and R. A. Buhrman, *Electromigration studies of the role of oxygen defects in $YBa_2Cu_3O_{7-\delta}$ grain boundary weak links*, IEEE Trans. Appl. Supercond. **3**, 2038 (1993). 99
- [99] B. H. Moeckly, D. K. Lathrop, and R. A. Buhrman, *Electromigration study of oxygen disorder and grain-boundary effects in $YBa_2Cu_3O_{7-\delta}$ thin films*, Phys. Rev. B **47**, 400 (1993). 138, 139
- [100] B. H. Moeckly, R. A. Buhrman, and P. E. Sulewski, *Micro-Raman spectroscopy of electromigration-induced oxygen vacancy aggregation in $YBa_2Cu_3O_{7-\delta}$* , Appl. Phys. Lett. **64**, 1427 (1994). 99
- [101] R. F. Klie *et al.*, *Enhanced current transport at grain boundaries in high- T_c superconductors*, Nature **435**, 475 (2005). 99
- [102] X. Zhang *et al.*, *Transport anomalies and quantum criticality in electron-doped cuprate superconductors*, Phys. C **525-526**, 18 (2016). 101
- [103] C. R. Rotundu *et al.*, *High-pressure effects on single crystals of electron-doped $Pr_{2-x}Ce_xCuO_4$* , Phys. Rev. B **87**, 024506 (2013). 101
- [104] P. Gao *et al.*, *Electrically Driven Redox Process in Cerium Oxides*, J. Am. Chem. Soc. **132**, 4197 (2010). 101
- [105] E. Roduner, *Size matters: why nanomaterials are different*, Chem. Soc. Rev. **35**, 583 (2006). 106
- [106] L.-F. Zhang, L. Covaci, M. V. Milošević, G. R. Berdiyrov, and F. M. Peeters, *Unconventional Vortex States in Nanoscale Superconductors Due to Shape-Induced Resonances in the Inhomogeneous Cooper-pair Condensate*, Phys. Rev. Lett. **109**, 107001 (2012). 106
- [107] V. Moshchalkov *et al.*, *Effect of sample topology on the critical fields of mesoscopic superconductors*, Nature **373**, 319 (1995). 106, 111

- [108] A. A. Shanenko, M. D. Croitoru, M. Zgirski, F. M. Peeters, and K. Arutyunov, *Size-dependent enhancement of superconductivity in Al and Sn nanowires: Shape-resonance effect*, Phys. Rev. B **74**, 052502 (2006). 106, 107
- [109] A. Halder, A. Liang, and V. V. Kresin, *A Novel Feature in Aluminum Cluster Photoionization Spectra and Possibility of Electron Pairing at T greater than or similar to 100 K*, Nano Lett. **15**, 1410 (2015). 106
- [110] D. B. Haviland, Y. Liu, and A. M. Goldman, *Onset of superconductivity in the two-dimensional limit*, Phys. Rev. Lett. **62**, 2180 (1989). 106
- [111] A. Bezryadin, C. N. Lau, and M. Tinkham, *Quantum suppression of superconductivity in ultrathin nanowires*, Nature **404**, 971 (2000). 106, 114, 117, 121
- [112] D. S. Golubev and A. D. Zaikin, *Quantum tunneling of the order parameter in superconducting nanowires*, Phys. Rev. B **64**, 014504 (2001). 114, 117
- [113] C. Lau, N. Markovic, M. Bockrath, A. Bezryadin, and M. Tinkham, *Quantum phase slips in superconducting nanowires*, Phys. Rev. Lett. **87** (2001). 106, 114
- [114] Y. Chen, Y.-H. Lin, S. D. Snyder, A. M. Goldman, and A. Kamenev, *Dissipative superconducting state of non-equilibrium nanowires*, Nat. Phys. **10**, 567 (2014). 106
- [115] J. S. Langer and V. Ambegaokar, *Intrinsic Resistive Transition in Narrow Superconducting Channels*, Phys. Rev. **164**, 498 (1967). 106, 113
- [116] D. E. McCumber and B. I. Halperin, *Time Scale of Intrinsic Resistive Fluctuations in Thin Superconducting Wires*, Phys. Rev. B **1**, 1054 (1970). 106, 113
- [117] M. Zgirski, K.-P. Riikonen, V. Touboltsev, and K. Arutyunov, *Size Dependent Breakdown of Superconductivity in Ultranarrow Nanowires*, Nano Lett. **5**, 1029 (2005). 106, 121, 143
- [118] A. Bezryadin and P. M. Goldbart, *Superconducting Nanowires Fabricated Using Molecular Templates*, Adv. Mater. **22**, 1111 (2010). 121, 127
- [119] T. Morgan-Wall, H. J. Hughes, N. Hartman, T. M. McQueen, and N. Markovic, *Fabrication of sub-15 nm aluminum wires by controlled etching*, Appl. Phys. Lett. **104** (2014). 106
- [120] D. Y. Vodolazov and F. M. Peeters, *Enhancement of the retrapping current of superconducting microbridges of finite length*, Phys. Rev. B **85**, 024508 (2012). 107, 116

-
- [121] J. Romijn, T. M. Klapwijk, M. J. Renne, and J. E. Mooij, *Critical pair-breaking current in superconducting aluminum strips far below T_c* , Phys. Rev. B **26**, 3648 (1982). 109
- [122] F. R. Fickett, *Aluminum-1. A review of resistive mechanisms in aluminum*, Cryogenics **11**, 349 (1971). 109
- [123] COMSOL Multiphysics, *Joule heating module* (COMSOL Inc.). 110
- [124] V. V. Moshchalkov *et al.*, *Superconductivity in Networks and Mesoscopic Systems* (AIP, 1998). 111
- [125] C. Strunk *et al.*, *Nonlocal effects in mesoscopic superconducting aluminum structures*, Phys. Rev. B **54**, R12701 (1996). 111
- [126] M. Zgirski, K.-P. Riikonen, V. Touboltsev, and K. Y. Arutyunov, *Quantum fluctuations in ultranarrow superconducting aluminum nanowires*, Phys. Rev. B **77**, 054508 (2008). 112, 114
- [127] M.-H. Bae, R. C. Dinsmore, T. Aref, M. Brenner, and A. Bezryadin, *Current-Phase Relationship, Thermal and Quantum Phase Slips in Superconducting Nanowires Made on a Scaffold Created Using Adhesive Tape*, Nano Lett. **9**, 1889 (2009). 113, 114, 143
- [128] R. S. Newbower, M. R. Beasley, and M. Tinkham, *Fluctuation Effects on the Superconducting Transition of Tin Whisker Crystals*, Phys. Rev. B **5**, 864 (1972). 113
- [129] N. Giordano, *Evidence for Macroscopic Quantum Tunneling in One-Dimensional Superconductors*, Phys. Rev. Lett. **61**, 2137 (1988). 114
- [130] F. Altomare, A. M. Chang, M. R. Melloch, Y. Hong, and C. W. Tu, *Evidence for Macroscopic Quantum Tunneling of Phase Slips in Long One-Dimensional Superconducting Al Wires*, Phys. Rev. Lett. **97**, 017001 (2006). 114, 121, 132
- [131] D. Y. Vodolazov, *Negative magnetoresistance and phase slip process in superconducting nanowires*, Phys. Rev. B **75**, 184517 (2007). 114, 115
- [132] A. Schmid and G. Schön, *Linearized kinetic equations and relaxation processes of a superconductor near T_c* , J. Low Temp. Phys. **20**, 207 (1975).
- [133] K. Y. Arutyunov, *Negative magnetoresistance of ultra-narrow superconducting nanowires in the resistive state*, Physica C **468**, 272 (2008).

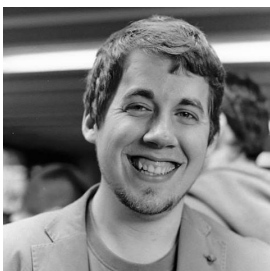
- [134] Y. Chen, S. D. Snyder, and A. M. Goldman, *Magnetic-Field-Induced Superconducting State in Zn Nanowires Driven in the Normal State by an Electric Current*, Phys. Rev. Lett. **103**, 127002 (2009).
- [135] Y. Chen, Y.-H. Lin, S. D. Snyder, and A. M. Goldman, *Stabilization of superconductivity by magnetic field in out-of-equilibrium nanowires*, Phys. Rev. B **83**, 054505 (2011). 114
- [136] T. E. Golikova *et al.*, *Nonlocal supercurrent in mesoscopic multiterminal SNS Josephson junction in the low-temperature limit*, Phys. Rev. B **89**, 104507 (2014). 116
- [137] F. Hübler, J. C. Lemyre, D. Beckmann, and H. v. Löhneysen, *Charge imbalance in superconductors in the low-temperature limit*, Phys. Rev. B **81**, 184524 (2010). 125
- [138] G. J. Dolan and L. D. Jackel, *Voltage Measurements within the Nonequilibrium Region near Phase-Slip Centers*, Phys. Rev. Lett. **39**, 1628 (1977). 116
- [139] A. D. Zaikin, D. S. Golubev, A. van Otterlo, and G. T. Zimanyi, *Quantum fluctuations and dissipation in thin superconducting wires*, Physics-Uspekhi **41**, 226 (1998). 117
- [140] H. P. Büchler, V. B. Geshkenbein, and G. Blatter, *Quantum Fluctuations in Thin Superconducting Wires of Finite Length*, Phys. Rev. Lett. **92**, 067007 (2004). 117
- [141] G. Schön and A. D. Zaikin, *Quantum coherent effects, phase transitions, and the dissipative dynamics of ultra small tunnel junctions*, Phys. Rep. **198**, 237 (1990). 117
- [142] J. S. Penttilä, U. Parts, P. J. Hakonen, M. A. Paalanen, and E. B. Sonin, *“Superconductor-Insulator Transition” in a Single Josephson Junction*, Phys. Rev. Lett. **82**, 1004 (1999). 117
- [143] S. Blundell, *Magnetism in Condensed Matter* (Oxford University Press, Inc., 2001). 120
- [144] J. A. Cuesta and A. Sánchez, *General Non-Existence Theorem for Phase Transitions in One-Dimensional Systems with Short Range Interactions, and Physical Examples of Such Transitions*, J. Stat. Phys. **115**, 869 (2004). 120
- [145] J. Meyer and G. v. Minnigerode, *Instabilities in the transition curve of current-carrying one-dimensional superconductors*, Phys. Lett. A **38**, 529 (1972). 120, 125

-
- [146] N. Shah, D. Pekker, and P. M. Goldbart, *Inherent Stochasticity of Superconductor-Resistor Switching Behavior in Nanowires*, Phys. Rev. Lett. **101**, 207001 (2008). 121, 127
- [147] D. Massarotti *et al.*, *Breakdown of the escape dynamics in Josephson junctions*, Phys. Rev. B **92**, 054501 (2015). 121, 130, 135
- [148] T. Aref, A. Levchenko, V. Vakaryuk, and A. Bezryadin, *Quantitative analysis of quantum phase slips in superconducting $\text{Mo}_{76}\text{Ge}_{24}$ nanowires revealed by switching-current statistics*, Phys. Rev. B **86**, 024507 (2012). 121, 128, 134
- [149] M. Sahu *et al.*, *Individual topological tunnelling events of a quantum field probed through their macroscopic consequences*, Nat. Phys. **5**, 503 (2009). 121, 132
- [150] W. J. Skocpol, M. R. Beasley, and M. Tinkham, *Phase-slip centers and nonequilibrium processes in superconducting tin microbridges*, J. Low Temp. Phys. **16**, 145 (1974). 125
- [151] A. M. Kadin, W. J. Skocpol, and M. Tinkham, *Magnetic field dependence of relaxation times in nonequilibrium superconductors*, J. Low Temp. Phys. **33**, 481 (1978). 126
- [152] M. Tinkham, J. U. Free, C. N. Lau, and N. Markovic, *Hysteretic I-V curves of superconducting nanowires*, Phys. Rev. B **68**, 134515 (2003). 126
- [153] R. G. Mints and A. L. Rakhmanov, *Critical state stability in type-II superconductors and superconducting-normal-metal composites*, Rev. Mod. Phys. **53**, 551 (1981). 126
- [154] A. Murphy *et al.*, *Universal Features of Counting Statistics of Thermal and Quantum Phase Slips in Nanosize Superconducting Circuits*, Phys. Rev. Lett. **110**, 247001 (2013). 127, 135
- [155] P. Dubos, *Josephson critical current in a long mesoscopic S-N-S junction*, Phys. Rev. B **63**, 064502 (2001). 127, 128
- [156] I. O. Kulik and A. N. Omel'yanchuk, *Contribution to the microscopic theory of the josephson effect in superconducting bridges*, JETP Lett. **21**, 96 (1975). 127
- [157] I. O. Kulik and A. N. Omel'yanchuk, *Current flow in long superconducting junctions*, JETP Lett. **41**, 1071 (1975). 127
- [158] J. Bardeen, *Critical Fields and Currents in Superconductors*, Rev. Mod. Phys. **34**, 667 (1962). 130

- [159] P. Li *et al.*, *Switching Currents Limited by Single Phase Slips in One-Dimensional Superconducting Al Nanowires*, Phys. Rev. Lett. **107**, 137004 (2011). 132, 134
- [160] T. A. Fulton and L. N. Dunkleberger, *Lifetime of the zero-voltage state in Josephson tunnel junctions*, Phys. Rev. B **9**, 4760 (1974). 132, 134
- [161] J. Kurkijärvi, *Intrinsic Fluctuations in a Superconducting Ring Closed with a Josephson Junction*, Phys. Rev. B **6**, 832 (1972).
- [162] A. Garg, *Escape-field distribution for escape from a metastable potential well subject to a steadily increasing bias field*, Phys. Rev. B **51**, 15592 (1995). 134
- [163] G. B. Arfken and H. J. Weber, *Mathematical Methods for Physicists*, 4 ed. (Academic Press, Inc., 1995). 134
- [164] S.-Z. Lin and D. Roy, *Role of kinetic inductance in transport properties of shunted superconducting nanowires*, J. Phys.: Condens. Matter **25**, 325701 (2013). 134
- [165] S. S. P. Parkin, M. Hayashi, and L. Thomas, *Magnetic Domain-Wall Racetrack Memory*, Science **320**, 190 (2008). 138
- [166] S. Vitta, M. A. Stan, J. D. Warner, and S. A. Alterovitz, *Electromigration failure in $YBa_2Cu_3O_{7-\delta}$ thin films*, Appl. Phys. Lett. **58**, 759 (1991). 138, 139
- [167] G. N. Mikhailova, A. M. Prokhorov, A. V. Troitskii, and L. Y. Shchurova, *Ion migration in high- t_c superconductors and the nature of the conducting state in d -wave superconductors*, Inorg Mater **36**, 807 (2000). 138, 139
- [168] X. D. A. Baumans *et al.*, *Healing Effect of Controlled Anti-Electromigration on Conventional and High-Tc Superconducting Nanowires*, Small **13**, 1700384. 138, 139
- [169] J. Lombardo *et al.*, *In situ tailoring of superconducting junctions via electro-annealing*, Nanoscale **10**, 1987 (2018). 138, 139
- [170] M. Baziljevich, E. Baruch-El, T. H. Johansen, and Y. Yeshurun, *Dendritic instability in $YBa_2Cu_3O_{7-\delta}$ films triggered by transient magnetic fields*, Appl. Phys. Lett. **105**, 012602 (2014). 138
- [171] A. J. Kerman *et al.*, *Constriction-limited detection efficiency of superconducting nanowire single-photon detectors*, Appl. Phys. Lett. **90**, 101110 (2007). 138
- [172] K. Jin *et al.*, *Anomalous enhancement of the superconducting transition temperature of electron-doped $La_{2-x}Ce_xCuO_4$ and $Pr_{2-x}Ce_xCuO_4$ cuprate heterostructures*, Phys. Rev. B **83**, 060511 (2011). 139

-
- [173] N. Giordano, W. Gilson, and D. E. Prober, *Experimental Study of Anderson Localization in Thin Wires*, Phys. Rev. Lett. **43**, 725 (1979). 143
- [174] D. Staudt and R. Hoffmann-Vogel, *Controlled electromigration of thin Pb films started from the normal and from the superconducting state*, J. Phys. D: Appl. Phys. **50**, 185301 (2017). 144
- [175] V. V. Lemanov, A. L. Kholkin, and A. B. Sherman, *Ybco thin films on ferroelectric substrates: the polarization-induced changes of superconductive properties*, SuST **6**, 814 (1993). 144
- [176] S. G. Sarwat *et al.*, *Scaling Limits of Graphene Nanoelectrodes*, Nano Lett. **17**, 3688 (2017). 145
- [177] J. Moser and A. Bachtold, *Fabrication of large addition energy quantum dots in graphene*, Appl. Phys. Lett. **95**, 173506 (2009). 145

Curriculum Vitae



Name: Xavier D. A. Baumans

Birthdate: December 3, 1989

Nationality: Belgium (BE)

Current address: Rue Félix Vandersnoeck 94, 4000 Liège, Belgium

E-mail (permanent): xavierbaumans@gmail.com

Education

- **2013-2018**

PhD student with assistant tenure at physics department of University of Liège
Group of Experimental Physics of Nanostructured Materials

- **2011-2013**

Master degree in Physics, University of Liège, Belgium

Master thesis: Isotope shifts and hyperfine structure of the 372.8 nm resonance
line of neutral ruthenium

Grade: Magna Cum Laude

- **2008-2011**

Bachelor in Physics, University of Liège, Belgium

- **2001-2007**

Secondary school: Collège Royal Marie-Thérèse, Herve, Belgium

List of publications

1. **Nano-SQUIDs with controllable weak links created via current-induced atom migration**
W. Keijers, **X. D. A. Baumans**, R. Panghotra J. Lombardo, V. S. Zharinov, R. B. G. Kramer,, A. V. Silhanek, and J. Van de Vondel.
Submitted (2018).
2. **Controlled electromigration protocol revised**
V. Zharinov, **X. D. A. Baumans**, A. V. Silhanek, E. Janssens, and J. Van de Vondel.
Review of Scientific Instruments **89**, 043904 (2018).
3. **In situ tailoring of superconducting junctions via electro-annealing**
J. Lombardo, Ž. L. Jelić, **X. D. A. Baumans**, J. E. Scheerder, J. P. Nacenta, V. V. Moshchalkov, J. Van de Vondel, R. B. G. Kramer, M. V. Milosevic and A. V. Silhanek
Nanoscale **10**, 1987 (2018).
4. **Healing effect of controlled anti-electromigration on conventional and high- T_c superconducting nanowires**
X. D. A. Baumans, J. Lombardo, J. Brisbois, G. Shaw, V. S. Zharinov, G. He, H. Yu, J. Yuan, B. Zhu, K. Jin, R. B. G. Kramer, J. Van de Vondel, and A. V. Silhanek.
Small, 1700384 (2017).
5. **Statistics of localized phase slips in tunable width planar point contacts**
X. D. A. Baumans, V. S. Zharinov, E. Raymenants, S. Blanco Alvarez, J. E. Scheerder, J. Brisbois, D Massarotti, R. Caruso, F. Tafuri, E. Janssens, V. V. Moshchalkov, J. Van de Vondel, and A. V. Silhanek.
Scientific Reports **7**, 44569 (2017).
6. **Thermal and quantum depletion of superconductivity in narrow junctions created by controlled electromigration**
X. D. A. Baumans, D. Cerbu, O.-A. Adami, V. S. Zharinov, N. Verellen, G. Papari, J. E. Scheerder, G. Zhang, V. V. Moshchalkov, A. V. Silhanek and J. Van de Vondel.
Nature Communications **7**, 10560 (2016).

Conferences and scientific missions

- **26-29 March 2018:** Coherent Superconducting Hybrids and Related Materials ($S^i\varphi$ hybrids, Les Arcs 1800, France)
Talk: "Anti-Electromigration: Restoring Conventional and High- T_c Ultra-Narrow Superconducting Junctions"
- **24 September - 1 October 2016:** Short Term Scientific Mission (STSM NanoSC-COST, Naples, Italy) in order to obtain critical current distributions of electromigrated nanoconstrictions in a ultra-high quality of filtering cryostat (group of Prof. F. Tafuri)
- **4-9 September 2016:** Applied Superconductivity Conference (ASC, Denver, Colorado, USA)
Talk: "Ultra-narrow superconducting junctions: electromigration to shed light on quantum point contacts"
- **26 November 2015:** One-day conference "Superconductivity in the Greater Region" (UdS Saarbrücken, Germany)
Poster presentation: Electromigration to explore superconductivity at the nanoscale
- **12-17 September 2015:** 9th international conference in school format on Vortex Matter in nanostructured Superconductors (Vortex IX, Rhodos, Greece)
Poster presentation: Thermal and quantum depletion of superconductivity in narrow junctions created by controlled electromigration
- **13 May 2015:** Belgian Physical Society annual meeting (Liège, Belgium)
Poster presentation: Superconducting properties of electromigrated nanowires

